

CHEMISTRY AND MORPHOLOGY OF ROCKS: IMPLICATION  
FOR CO<sub>2</sub> STORAGE CAPACITY

by  
Manju Pharkavi Murugesu

Copyright by Manju Pharkavi Murugesu 2019

All Rights Reserved

A thesis submitted to the Faculty and the Board of Trustees of the Colorado School of Mines in partial fulfillment of the requirements for the degree of Master of Science (Petroleum Engineering).

Golden, Colorado

Date \_\_\_\_\_

Signed: \_\_\_\_\_

Manju Pharkavi Murugesu

Signed: \_\_\_\_\_

Dr. Manika Prasad  
Thesis Advisor

Signed: \_\_\_\_\_

Dr. Svitlana Pylypenko  
Thesis Advisor

Golden, Colorado

Date \_\_\_\_\_

Signed: \_\_\_\_\_

Dr. Erdal Ozkan  
Professor and Head  
Department of Petroleum Engineering

## ABSTRACT

Carbon Capture, Storage and Utilization (CCUS) on a large scale is one of the possible solutions to mitigate CO<sub>2</sub> emission into the atmosphere. Potential escape of CO<sub>2</sub> due to leaking faults and seals in subsurface formations poses a safety risk. Therefore, it is important to investigate CO<sub>2</sub> trapping mechanisms in the formation: structural and stratigraphic trapping, residual trapping, solubility trapping and mineral trapping (Benson et al. 2012). Trapping occurs at the interface of rock-CO<sub>2</sub>, and rock-CO<sub>2</sub> dissolved in water. This dissertation studies wettability of rock surfaces at a micro scale to understand rock-fluid interaction along CO<sub>2</sub> pathways in the formation. The methods utilized are gas adsorption, surface free energy, and X-ray Photoelectron Spectroscopy (XPS).

In the first part of the thesis, shales rich in calcite, clay and organic matter are investigated. The analysis of CO<sub>2</sub> with calcite-rich shale suggests presence of chemisorbed water in calcite that permanently traps CO<sub>2</sub> in the ultra-micropore region (0.2-0.4 nm) at reservoir conditions. Such trapping is not observed in clay- and organic-rich shales; removal of soluble organic matter leads to a gradual but reversible increase in CO<sub>2</sub> adsorption in the micropore region (<2 nm).

In the second part of the thesis, rock surface forces are studied by determining their surface free energy. The prominent component governing the interactions on shale surfaces is van der Waals forces. The surface free energy of individual pure minerals does not contribute to the effective surface free energy of the shale in an additive manner. However, a validation of surface free energy is not possible because the existing theoretical inversion models are not comparable to each other.

I explored the usability of X-ray Photoelectron Spectroscopy (XPS) to characterize chemical compositions and reactions on the surface. Literature review of XPS shows that XPS has

been successfully used to evaluate oil wettability through identification and quantification of organic carbon content, sulfur and nitrogen elements on the rock surface. In this work, I present a workflow to use near-ambient pressure capability of XPS to study mineral carbonation while dosing with gases such as CO<sub>2</sub>, H<sub>2</sub>O and CH<sub>4</sub>. Preliminary sample characterizations are conducted in this study using XRD, ESEM/EDS and TGA.

Finally, the results from this thesis are used to estimate CO<sub>2</sub> storage capacity in calcite-rich and organic-rich shale formations. Permanent storage of CO<sub>2</sub> is observed in pore structures of calcite-rich shales. An increase in CO<sub>2</sub> storage capacity is observed in the pores of insoluble kerogen as soluble organic matter is removed, due to increasing micro-porosity and affinity of kerogen to CO<sub>2</sub>.

## TABLE OF CONTENTS

ABSTRACT.....	iii
LIST OF FIGURES .....	viii
LIST OF TABLES.....	xii
ACKNOWLEDGEMENT .....	xv
CHAPTER 1 INTRODUCTION.....	1
1.1 Storage Capacity and Pore Size Distribution .....	2
1.2 Wettability.....	3
1.3 Organization of the Thesis .....	5
1.4 Publications and Presentations .....	6
CHAPTER 2 NANO-SCALE SHALE-FLUID INTERACTIONS USING SUBCRITICAL GAS ADSORPTION.....	7
2.1 Terminology .....	7
2.1.1 Adsorption, Adsorbent, and Adsorptive .....	7
2.1.2 Ultra-micro, Micro-, Meso-, and Macro-pores .....	8
2.1.3 Organic Matter, Kerogen, and Bitumen.....	8
2.2 Background and Motivation.....	8
2.3 Adsorbent and Adsorptive.....	11
2.3.1 Adsorbent.....	11
2.3.2 Adsorptive.....	12
2.4 Methodology .....	13
2.4.1 Experimental method.....	13
2.4.2 Inversion Models .....	15
2.4.3 CO <sub>2</sub> adsorption.....	17

2.5	CO <sub>2</sub> -shale reactions .....	20
2.5.1	CO <sub>2</sub> -calcite rich shale .....	20
2.5.2	CO <sub>2</sub> -organic rich shale .....	22
2.5.3	CO <sub>2</sub> -clay rich shale .....	23
2.5.4	Calcite-CO <sub>2</sub> Reaction.....	23
2.5.5	Implication for CO <sub>2</sub> Storage .....	25
2.6	CO <sub>2</sub> Adsorption on Organic Matter.....	27
CHAPTER 3	SURFACE FREE ENERGY.....	37
3.1	Terminology .....	37
3.1.1	Wettability.....	37
3.1.2	Surface Free Energy.....	38
3.1.3	Contact Angle .....	40
3.2	Background and Motivation .....	40
3.3	Contact Angle Measurement Method.....	42
3.3.1	Droplet Size .....	44
3.3.2	Equilibrium Time.....	44
3.3.3	Fluid Choice.....	45
3.3.4	Sample Preparation .....	46
3.3.5	Summary of Methods.....	48
3.4	Results and Discussion .....	48
3.5	Inversion Models .....	56
3.5.1	van Oss-Chaudhury-Good Method.....	57
3.5.2	Owens and Wendt's Method.....	59
3.5.3	Results and Discussion .....	61
CHAPTER 4	CHEMICAL CHARACTERIZATION OF RESERVOIR AND CAP-ROCKS.....	65

4.1	Introduction .....	65
4.2	X-ray Diffraction (XRD) Mineral Analysis .....	67
4.3	Thermogravimetric analysis (TGA) .....	68
4.4	Electron Microscopy and Energy Dispersive X-ray Spectroscopy (EDS).....	72
4.5	X-ray Photoelectron Spectroscopy (XPS).....	83
4.6	Ambient Pressure X-ray Photoelectron Spectroscopy (AP-XPS).....	93
4.6.1	Capabilities of AP-XPS .....	93
4.6.2	Potential of XPS and AP-XPS for investigation of Mineral Carbonation.....	94
4.6.3	Proposed Workflow for Investigation of Gas-solid Interactions using XPS and AP-XPS, along with Complementary Techniques..	96
CHAPTER 5	CONCLUSION.....	100
5.1	Calcite – CO <sub>2</sub> Interaction .....	100
5.2	Organic Matter – CO <sub>2</sub> .....	101
5.3	Surface Free Energy .....	102
5.4	X-ray Photoelectron Spectroscopy .....	102
5.5	Conclusion.....	103
	LIST OF ABBREVIATIONS AND NOMENCLATURE .....	104
	REFERENCES CITED.....	106
	APPENDIX A SUPPLEMENTAL ELECTRONIC FILES.....	113

## LIST OF FIGURES

Figure 1.1	CO <sub>2</sub> storage mechanism based on physical and geochemical trapping. The four main categories are structural and stratigraphic trapping, residual CO <sub>2</sub> trapping, solubility trapping and mineral trapping (Benson et al. 2012).....	2
Figure 2.1	N <sub>2</sub> -adsorption isotherm of pure Na-rich Montmorillonite from Clay Minerals Society: (I) micropore filling occurs at the lowest relative pressure; (II) monolayer of adsorptive forms until the inflection point at P/P <sub>0</sub> = 0.4; (III) capillary condensation leads to hysteresis at the mesopores; (IV) presence of macropores is indicated by a steep curve at near-unity relative pressure (Sing et al. 1985; Kuila 2013; Thommes et al. 2015; Murugesu 2017).....	9
Figure 2.2	Workflow of experimental procedure breaking down the three main steps: sample preparation, outgassing the sample and analysis.....	14
Figure 2.3	a) Adsorption capacity, and b) pore size distribution of G1 (Green River Shale) of different masses. Although the higher mass sample causes the total volume adsorbed to be nearly double in the isotherm, the different masses do not cause significant variance in the pore size distribution.....	19
Figure 2.4	The isotherms obtained from CO <sub>2</sub> adsorption on Niobrara N1 (88.9% calcite content): First CO <sub>2</sub> run (Test 1) shows an open hysteresis, indicating possibly trapped CO <sub>2</sub> during the test. As subsequent tests are conducted, the total adsorption capacity gradually decreased due to the CO <sub>2</sub> molecules already occupying the existing pores. After degassing the sample again to remove all trapped gas, test 4 shows similar open hysteresis as test 1, but its total adsorption capacity did not return to original capacity. This suggests that some CO <sub>2</sub> is permanently trapped in the pores after test 1.....	21
Figure 2.5	CO <sub>2</sub> adsorption on organic-rich G1 (Green River Shale): First CO <sub>2</sub> run (Test 1) shows an open hysteresis, indicating possibly trapped CO <sub>2</sub> during the test. As subsequent tests are conducted, the total adsorption capacity gradually decreased. After degassing the sample again to remove all trapped gas, its total adsorption capacity returned to original capacity. CO <sub>2</sub> is not permanently trapped in the pores. ....	22
Figure 2.6	CO <sub>2</sub> run on clay-rich A1 (Agardhfjellet): A1 contains 61.1% of clay, 6% of carbonate and 12% of organic content. No successive decreasing adsorptive capacity is observed for A1 with consecutive runs. Hence, CO <sub>2</sub> is not trapped in the pores at any point of the runs. ....	23
Figure 2.7	Water content on calcite as a function of temperature (modified from Morimoto et al. 1980).....	24

Figure 2.8	Isotherm of pure calcite minerals at degassing temperatures of 200°C (grey dots) and 400°C (blue dots). The initial negative volume adsorbed for pure calcite at 200°C indicates possible dissolution of CO <sub>2</sub> into the chemisorbed water. When temperature was increased to 400°C, the initial volume drop was lesser than at 200°C and did not fall on negative scale. At 400°C, chemisorbed water has mostly evaporated, lowering CO <sub>2</sub> dissolution. The adsorption capacity after degassing at 400°C is higher as the CO <sub>2</sub> adsorbs to pore surfaces instead of dissolving in chemisorbed water. ....	25
Figure 2.9	Pore size distribution of calcite-rich N1 with different runs. Pore size distribution of N1 shows that decreasing presence of pores from 2Å to 4Å causes the decreasing trend of CO <sub>2</sub> adsorption capacity in N1 isotherm. Thus, CO <sub>2</sub> is possibly trapped in the pore range of 2Å to 4Å (ultra-micropores) between test 1 and test 4. ....	26
Figure 2.10	The adsorption capacity of organic-rich G1 is the highest, followed by clay-rich A1 and calcite-rich N1. ....	28
Figure 2.11	Solvent Extraction set-up for powder sample. The powder is placed in a cellulose and cotton balls are placed at the mouth of the cellulose, preventing the sample from overflowing. ....	30
Figure 2.12	(a) CO <sub>2</sub> adsorption isotherms of sample A1 showing increased adsorption capacity at the micropore level after extraction of soluble organic matter. (b) N <sub>2</sub> adsorption isotherms showing increased adsorption capacity at micropore (low relative pressure range) after toluene and chloroform extraction. It continued to increase at macropores (high relative pressure range) with chloroform extraction. ....	31
Figure 2.13	CO <sub>2</sub> adsorption isotherms of sample B1 showing increased adsorption capacity at the micropore level after extraction of soluble organic matter. (b) N <sub>2</sub> adsorption isotherms showing increased adsorption capacity at micropores (low relative pressure range) after toluene extraction and increased adsorption at macropores (high relative pressure range) after chloroform extraction. ....	32
Figure 2.14	(a) The pore size distribution obtained at the ultra-micropore level for sample A1. (b) The pore size distribution from micro- to mesopore range using N <sub>2</sub> adsorption. ....	32
Figure 2.15	(a) The pore size distribution obtained at the ultra-micropore level for sample B1. (b) The pore size distribution from micro- to mesopore range using N <sub>2</sub> adsorption. ....	32
Figure 3.1	Contact angle of a liquid drop on solid surface (Kwok and Neumann 1999). ...	39
Figure 3.2	The balance of forces between rock, oil and water (Zerpa et al. 2010). Water droplet with large contact angle (>120°) is denoted as oil-wet (Diagram on	

	the left). Water droplet with small contact angle ( $<90^\circ$ ) is denoted as water-wet (Diagram on the right). .....	40
Figure 3.3	Drop Shape Analyzer (DSA100) used to measure the contact angle. ....	41
Figure 3.4	Sessile Drop Method: (a) Droplet suspension on a fused silica; (b) The schematic of sessile drop method. ....	42
Figure 3.5	The variance in contact angles measured as captured by the high-resolution camera for calcite crystals. ....	50
Figure 3.6	The variance in contact angles measured as captured by the high-resolution camera for quartz microscope slides. ....	51
Figure 3.7	Whisker plot of calcite with each probe liquid: The plot compares the means of different groups shown in Table 3.7. The plot shows how groups B2 and D1 are different from the rest of the measurements for respective fluids. Group A1 is also removed due to its large variance within the group. Such variance is captured better by the JMP analysis method than discerning from whisker plot. ....	52
Figure 3.8	Whisker plot of quartz with each probe liquid: The plot compares the means of different groups shown in Table 3.8. As indicated by the JMP analysis method, the groups are not statistically different from each other for each probe liquid, largely due to homogeneity and flatness of quartz microscope slides. Some measurements from each group are removed to reduce the variance within the group. ....	53
Figure 3.9	The Owens and Wendt's plot with four probe liquids. The polar and dispersive components of the solids are derived from the linear plot. ....	59
Figure 4.1	TGA and derivative on Niobrara (N1) shale: Major mass loss occurs at $700^\circ\text{C}$ which corresponds to calcite minerals. ....	68
Figure 4.2	TGA and derivative on Agardhfjellet (A1) shale: Thermal analysis shows degradation of illite and smectite minerals at $500^\circ\text{C}$ and $600^\circ\text{C}$ respectively. Due to clay content, the sample loses free water and clay-bound water below $100^\circ\text{C}$ . Due to high organic content of the sample (12%), organic matter matures in increasing temperature after $400^\circ\text{C}$ goes through pyrolysis. ....	68
Figure 4.3	Features showing on the Agardhfjellet shale. The bright features are silt-rich due to high oxygen and silicon content. The dark features are possibly clay and organic matter due to its higher carbon, oxygen, aluminium, silicon, potassium and iron elements. ....	74
Figure 4.4	Mapping of elements on Agardhfjellet sample surface. ....	75

Figure 4.5	The features on unpolished Niobrara sample. Note the poor quality of image is due to obtaining the image from ESEM and low accelerating voltage.....	78
Figure 4.6	Photoemission Effect: As X-ray photons hit the core electron (closest to nucleus and characteristic of the atom), part of the energy is transferred to overcome the binding energy between the electron and nucleus, and the remaining energy becomes kinetic energy with which the photoelectron escapes to energy analyzer. The detector measures the kinetic energy of the photoelectron (Ratner and Castner 1994).....	81
Figure 4.7	Example of low-resolution spectrum obtained from XPS for reservoir rock (Mitchell et al. 1990). s and p refer to the orbitals the electron belongs to. KLL refers to Auger emission, where additional energy is released from an atom as a result of a higher energy state electron from outer shell transferring to a lower energy state core shell after the previous core electron has vacated upon photoemission.....	82
Figure 4.8	Plot of carbon content versus wettability index with data from Mitchell et al. (1990), Quet et al. (1991) and Toledo et al. (1996). Blue dots refer to water wetting indices and orange dots indicate oil wetting indices. The lines are drawn to illustrate potential trends. The stronger the water wetting tendency of rocks, the lower the carbon atomic percent. The stronger the oil wetting tendency of rocks, the higher the carbon atomic percent. ....	84
Figure 4.9	Difference in binding energy of carbon from calcium carbonate and air-borne organic carbon (Quet et al. 1991). ....	85
Figure 4.10	O1s XPS spectra acquired from perovskite film with H <sub>2</sub> O at different temperatures (Stoerzinger et al. 2015) demonstrating shifts due to interactions between perovskite and water: At 300°C, the deconvoluted O1 spectrum shows bulk oxygen from film, surface oxygen and OH <sup>-</sup> from initial H <sub>2</sub> O reaction. At 150°C, CO <sub>2</sub> traces in the chamber reacts with the sample, forming CO <sub>3</sub> <sup>2-</sup> . As temperature is cooled, adsorption of water occurs.....	91
Figure 4.11	The Experimental Plan for ambient-pressure XPS. The colored boxes are preliminary steps. ....	94

## LIST OF TABLES

Table 2.1	Origin of samples .....	11
Table 2.2	Mineralogy (XRD) of samples investigated with increasing TOC. Samples are Utica (U1), Green River Shale (G1), Niobrara (N1), Bakken (B1) and Agardhfjellet (A1). .....	12
Table 2.3	Inversion methods used to invert pore size distribution in micropores and mesopores, micro-porosity and specific surface area: Tick marks show the function of each inversion method and the shaded boxes show preferred methods for geological samples. ....	15
Table 2.4	Equilibrium Criteria Tested.....	18
Table 2.5	Cumulative pore volume of U1 for equilibrium criteria: timeout=800 s and equilibrium=400 s, timeout=1000 s and equilibrium=600 s, timeout=1400 s and equilibrium=1000 s.....	19
Table 2.6	Volume of CO <sub>2</sub> trapped in the ultra-micropore region for the given volume. ...	27
Table 2.7	RockEval for organic-rich A1 and B1.....	28
Table 2.8	Physical Properties of Organic Solvents (Zargari et al. 2015). ....	29
Table 2.9	Specific surface area exposed to adsorption for A1 and B1 determined using N <sub>2</sub> adsorption. ....	31
Table 2.10	The cumulative pore volume obtained from (CO <sub>2</sub> adsorption+N <sub>2</sub> adsorption), and CO <sub>2</sub> adsorption of A1 and B1 after sequential removal of soluble organic matter. ....	33
Table 2.11	CO <sub>2</sub> storage capacity estimated for cumulative pore volumes shown in Table 2.10: CO <sub>2</sub> -derived pore volume + N <sub>2</sub> -derived pore volume, compared with CO <sub>2</sub> -derived pore volume. Pore volume refers to cumulative pore volume obtained during adsorption at ultra-micropore (CO <sub>2</sub> ) and ultra-micropore to mesopore (CO <sub>2</sub> +N <sub>2</sub> ).....	34
Table 2.12	The additional storage capacity of CO <sub>2</sub> after bitumen removal. ....	35
Table 3.1	The surface tension components of probe liquids (van Oss 1993). The probe liquids are arranged in terms of decreasing polarity. Glycerol and ethylene glycol are highly basic liquids. Water has neutral basic and acid components. Diiodomethane and 1-Bromonaphthalene are non-polar liquids.....	44

Table 3.2	Contact angles measured on cleaned and uncleaned quartz and calcite crystals.....	46
Table 3.3	Contact angle measurements on fused silica optical flat (20λ). .....	46
Table 3.4	Summary of preparation method and fluid choice for each sample. ....	47
Table 3.5	Mineralogy of Niobrara shale obtained from XRD.....	48
Table 3.6	Contact angles measured on heterogenous Niobrara shales.....	48
Table 3.7	The contact angles on calcite crystals. The shaded cells contain values omitted. Different groups of samples are indicated by sample ID. The lines within each column shows groups of multiple measurements in the same locality. ....	52
Table 3.8	The contact angles on quartz microscope slides. The shaded cells contain values omitted. Different groups of samples are indicated by sample ID. ND refers to No Data. ....	53
Table 3.9	The means and standard deviation before and after the statistical analysis. ....	54
Table 3.10	The surface energy components as determined from the van Oss-Chaudhury-Good equation. ....	60
Table 3.11	The polar and dispersive component of calcite and quartz minerals determined using the Owens and Wendt's linear plot. ....	61
Table 3.12	Surface free energy of Niobrara compared with literature from Zelenev (2011). ....	62
Table 4.1	Mineralogy of Niobrara and Agardhfjellet shales determined by XRD.....	66
Table 4.2	Chemical composition of common rock minerals.....	70
Table 4.3	Comparison of different accelerating voltages for Agardhfjellet shale. The boxed values indicate consistently higher silicon content at 20kV compared to 10kV. ....	72
Table 4.4	The atomic percent of elements at different magnifications for Agardhfjellet shale.....	72
Table 4.5	Atomic percent of elements at three different spots on the same Agardhfjellet sample.....	73
Table 4.6	The average atomic percent of elements at prominent features shown on Figure 4.3.....	74

Table 4.7	The atomic percent of elements at different accelerating voltages for unpolished Niobrara shale: Carbon, oxygen and calcium element at 20kV and X100 are boxed as outliers because it does not match the predicted proportion for CaCO <sub>3</sub> in the calcite-rich Niobrara, where every atom of calcium should have equal amount of carbon and three times the amount of oxygen. ....	76
Table 4.8	Atomic percent of elements at different magnifications for unpolished Niobrara. The boxes indicate outliers.....	77
Table 4.9	Atomic percent of elements at different magnifications for polished Niobrara. ....	77
Table 4.10	The atomic percent of elements for different features on unpolished Niobrara. ....	78
Table 4.11	Comparison of atomic percent of elements between polished and unpolished Niobrara shale. The boxes show outliers because the ratio of the elements does not show expected composition for CaCO <sub>3</sub> .....	79
Table 4.12	Literature Review of wettability investigations using X-ray Photoelectron Spectroscopy.....	87

## ACKNOWLEDGEMENT

I would like to sincerely thank Dr. Manika Prasad for her guidance throughout my research while allowing me to have the freedom to explore science with my own curious mind. I owe her sincere gratitude for her extensive help in my greatest academic, research and personal achievements. Thank you for providing me the first opportunity to join your team and supporting my growth in the past four years. I would like to thank Dr. Svitlana Pylypenko for willingly taking me as her advisee and guiding me in a field that was completely new to me. Your guidance and constant encouragement have pushed me to go above and beyond. I would like to thank my committee members, Dr. Xiaolong Yin and Dr. Carolyn Koh for being on my committee, providing me with valuable insights and willingly allowing me to use experimental facility.

I would like to thank Dr. Hossein Kazemi for inspiring me through his reservoir simulation courses. Your lessons are invaluable, and I am inspired to look at challenging problems with a curious mind. I sincerely thank all my research group members (OCLAASH and SAM) especially Kurt, Mathias, Nerine and Mike for your valuable discussions, collaborations and help. Thank you to Dr. Miller for your valuable inputs on the content and formatting of the thesis. I thank for the support of Denise, Rachel, Terri and Kayla in the Petroleum Engineering department for keeping me on track with the logistics of undergraduate and graduate work. Thank you to Joe Chen and Weiping Wang for helping me with setting up experiments. I sincerely thank the U.S. Department of Energy and Chevron for providing the funding for my research.

Most importantly, I would like to thank my parents (Murugesu and Jaya Mala) and my siblings (Kharthik, Thamayanthy, Preveena and Narmatha) for constantly supporting me to take a step higher and believing in me.

## CHAPTER 1

### INTRODUCTION

Increasing greenhouse gases in the atmosphere raise concerns of climate change. Subsurface CO<sub>2</sub> storage or sequestration on a massive scale is one of the possible solutions to counteract increasing levels of atmospheric CO<sub>2</sub>. In Earth Science, Carbon Capture, Utilization, and Storage (CCUS) describes the process of capturing CO<sub>2</sub> produced by coal plants or from natural sources to use for enhanced oil recovery and simultaneous storage of CO<sub>2</sub> in subsurface formations. Potential storage sites for CO<sub>2</sub> can be deep saline aquifers, basalts, depleted shale and sandstone reservoirs, and coal seams. The risks associated with subsurface CO<sub>2</sub> storage, such as long-term leakage of CO<sub>2</sub> through damaged seals, faults, fractures, and groundwater contamination need to be carefully assessed via comprehensive theoretical and laboratory studies.

Storage occurs through four identified trapping mechanisms as shown in Figure 1.1 (Benson et al. 2012). The permanence of CO<sub>2</sub> trapping depends on reactivity of CO<sub>2</sub> with the mineral. The trapping mechanisms occur at the interface of rock and CO<sub>2</sub> or rock and CO<sub>2</sub> dissolved in water, along pathways of faults, fractures and seals. CO<sub>2</sub> is soluble in water and forms carbonic acid that reacts with the host rock causing mineral dissolution, precipitation, and ultimately altering the rock matrix. Mineral precipitation and dissolution could alter both rock and fluid chemistry. Therefore, a special report by the Intergovernmental Panel on Climate Change (Metz et al. 2005) recommends laboratory studies of reservoir and cap-rocks with native pore fluids and CO<sub>2</sub> to understand the effects of interfacial reactions in complex mineralogy. These reactions at the interfaces are governed by preferential wettability of mineral constituents of the rock.

Past CO<sub>2</sub> pilot projects are predominantly performed in depleted sandstone reservoirs and saline aquifers. This thesis shows the potential for shale reservoir and cap-rocks while addressing two concepts, storage capacity and wettability. By studying CO<sub>2</sub> reaction with calcite, clay and organic matter, I studied potential for CO<sub>2</sub> storage by adsorption in the pore structures of shale reservoirs. The effect of pore structure (e.g. pore size distribution) on storage capacity is given emphasis. Wettability is visited throughout this work as the parameter that determines rock-fluid interaction and subsequently storage capacity.

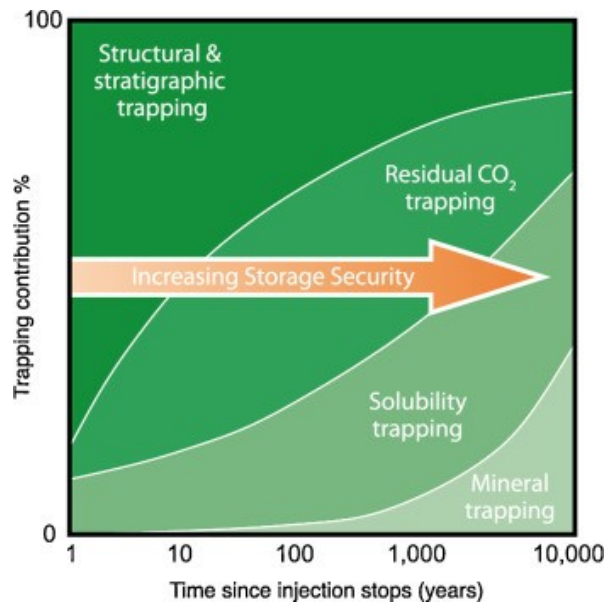


Figure 1.1: CO<sub>2</sub> storage mechanism based on physical and geochemical trapping. The four main categories are structural and stratigraphic trapping, residual CO<sub>2</sub> trapping, solubility trapping and mineral trapping (Benson et al. 2012).

## 1.1 Storage Capacity and Pore Size Distribution

Sorption capacity of CO<sub>2</sub> onto the surface of porous media largely depends on the reservoir conditions and mineralogy. Mineral composition is the controlling factor of nano-scale microstructures (pore width < 200 nm) in shales and its complex wetting properties. It is important

to understand the adsorption phenomenon as 80% storage capacity in shales occurs by sorption (Ambrose et al. 2012).

Adsorption is the enrichment of fluids in an interfacial layer (Thommes et al. 2015). I discuss the effect of mineralogy and moisture in CO<sub>2</sub> using a low-pressure system, also known as subcritical adsorption. Conventionally, nitrogen gas has been used prevalently as the adsorptive due to its wide availability and affordability. Nitrogen adsorption gives useful information such as specific surface area and pore size distribution in the micro- to mesopores (Pore diameter = 0.7 nm – 50 nm). However, the kinetic diameter of nitrogen (0.36nm) prevents it from accessing ultramicropores (Pore width < 0.7 nm). The kinetic diameter of CO<sub>2</sub> (0.33 nm) allows the access to the micropore region of shales. CO<sub>2</sub>-derived microporosity combined with N<sub>2</sub>-derived mesoporosity gives a larger range of pore size distribution (pore width = 0.25-50 nm). The pore size distribution influences interactions of wettability and fluid flow. In terms of pore size distribution, this paper presents: (i) comparison between the pore size distribution obtained from N<sub>2</sub> and CO<sub>2</sub> sorption; (ii) study of CO<sub>2</sub> sorption with existing moisture condition in minerals such as calcite; and (iii) excess sorption of CO<sub>2</sub> after removal of soluble organic matter.

## **1.2 Wettability**

Wettability of rocks can be defined as the preference of one fluid to wet the rock surface compared to another fluid. The pore surfaces of rocks consist of multiple minerals with varying preferential affinities for pore fluids such as brine, hydrocarbon, and CO<sub>2</sub>. The interfacial chemistry of composite minerals determines the effective wetting behavior of rocks. Wettability governs rock-fluid interactions which affects electrical properties, capillary pressure, relative permeability, dispersion, oil recovery, irreducible water saturation, residual oil saturation and stimulation operations (Anderson 1986).

Techniques commonly used to determine pore surface wettability are Amott-Harvey core flooding, centrifuge capillary flooding, relative permeability tests, and contact angle. Amott-Harvey test is laborious and takes several months for samples with tight permeability (Quet et al. 1991; Toledo et al. 1996). For centrifuge flooding, the reliability can be limited if it does not correspond to equilibrium conditions (Huang and Holm 1988). Relative permeability tests allow inferring wettability from the end-point data, but the end-points tend to have skewed data for strongly oil wet samples (Mitchell et al. 1990). The three-phase, flat-surface contact angle may not be applicable for matrix pores of tight reservoirs (Kumar 2016). The common limitation of these techniques is lack of fine-scale wettability evaluation.

Rocks are polymineralic and therefore, I emphasized studying mineral-CO<sub>2</sub> reactions before studying the composite rock. Gas adsorption, surface free energy, Environmental Scanning Electron Microscope (ESEM), Energy Dispersive Spectroscopy (EDS) and X-ray Photoelectron Spectroscopy (XPS) are utilized to study the physicochemical properties of rocks.

Wettability is controlled by surface forces. The attraction and repulsion at rock-fluid interface is governed by the intermolecular forces (Donaldson and Alam 2008). This dissertation defines surface free energy of solids in terms of the various intermolecular forces (van der Waals, Lewis acid-base and polarity) to fundamentally predict the wettability behavior of various minerals with fluids. Due to the limitation of the theoretical models used to invert surface free energy, I explored the potential for X-ray Photoelectron Spectroscopy (XPS) to quantify chemical interactions and to predict the major elements that cause reactions at the rock-fluid interface. XPS analysis is quick and inexpensive compared to the above-mentioned methods used to derive wettability and shows fine-scale (elemental-scale) wettability.

### 1.3 Organization of the Thesis

This thesis consists of five chapters. The core results of my research are presented in Chapters 2 through 4. The work conducted in each chapter is independent of each other, but the concepts are related. The main contents of each chapter are as shown:

**Chapter 1** provides the motivation for studying wettability and the structure of this thesis.

**Chapter 2** presents results for CO<sub>2</sub> and N<sub>2</sub> adsorption. I study various shales rich in minerals such as calcite, clay and organic matter. The pore size distribution ranging from ultra-micropore to mesopore region is provided to study the physicochemical properties of shales and how it affects the fluid distribution and flow. This chapter is in preparation for publication.

**Chapter 3** shows the potential for deriving surface free energy for rock surfaces from contact angle measurements. The findings shed light on the challenges and limitations of both experimental contact angle and theoretical inversion models.

**Chapter 4** explores the potential for using X-ray Photoelectron Spectroscopy to characterize the chemical reactions and wettability at rock-fluid interface. I present various methods to characterize the bulk mineralogy of shales, followed by elemental characterization. A review of past literature and workflow of XPS to rigorously study rock-fluid interaction is presented. This chapter is in preparation for literature review publication.

**Chapter 5** summarizes the main findings of the thesis.

## 1.4 Publications and Presentations

### *Peer-reviewed Publications*

1. Revil, A., Murugesu, M., Prasad, M., and Le Breton, M. (2017). Alteration of volcanic rocks: A New Non-Intrusive Indicator Based on Induced Polarization Measurements. *Journal of Volcanology and Geothermal Research*, 341, 351-362.

### *Conference Proceedings*

2. Murugesu, M., and Prasad, M. (April 2019). CO<sub>2</sub> Reaction with Organic- and Carbonate-Rich Shales. Abstract accepted at 5th International Workshop of Rock Physics, Hong Kong
3. Murugesu, M., Joewondo, N., and Prasad, M. (October 2018). CO<sub>2</sub> Sorption Capacity in Clay-rich Shales with Moisture Content. Submitted to Greenhouse Gas Control Technologies (GHGT-14), Australia.
4. Murugesu, M., and Prasad, M. (May 2018). Surface Characterization to Determine Wettability. Oral presentation at 13th International Symposium on Reservoir Wettability and its Effects on Oil Recovery, Austin, TX.
5. Murugesu, M. P. (2017, October). Pore Structure Analysis Using Subcritical Gas Adsorption Method. In SPE Annual Technical Conference and Exhibition. Society of Petroleum Engineers.
6. Joewondo, N., Murugesu, M., and Prasad, M. (June 2017). A Systematic Workflow in Quantifying Surface Area and Pore-Size Distribution Using The Nitrogen Adsorption Experiment. Poster presented at 4th International Workshop of Rock Physics, Trondheim, Norway.
7. Murugesu, M., and Prasad, M. (Sept 2016). Rock Characterization through Gas Adsorption. Poster presented at Geological Society of America (GSA), Denver, CO.

CHAPTER 2  
NANO-SCALE SHALE-FLUID INTERACTIONS USING SUBCRITICAL GAS  
ADSORPTION

This chapter is in preparation for submission to journal.

This chapter shows interactions of shales with CO<sub>2</sub> using subcritical gas adsorption, where the interactions govern storage of CO<sub>2</sub> by physical or chemical means. Shales rich in specific minerals are chosen to compare the affinity of CO<sub>2</sub> to each mineral. N<sub>2</sub> adsorption is conducted along with CO<sub>2</sub> adsorption to characterize porosity (storage capacity) of shales from ultra-micropore to mesopore. The chapter is separated into six sections: (1) Terminology and specific concepts discussed in the chapter are defined; (2) Background and motivation of conducting subcritical gas adsorption is introduced; (3) The mineralogy of samples and properties of fluids used for subcritical adsorption is shown; (4) Methodology outlines the experimental method and inversion models for N<sub>2</sub> and CO<sub>2</sub> adsorption; (5) CO<sub>2</sub>-shale mineral reactions are studied by comparing CO<sub>2</sub> adsorption trend on shales dominant in certain minerals (calcite, clay and organic matter); and (6) CO<sub>2</sub> adsorption on organic matter is further investigated due to affinity of CO<sub>2</sub> to organic matter.

## **2.1 Terminology**

### **2.1.1 Adsorption, Adsorbent, and Adsorptive**

Adsorption is defined as enrichment of molecules at an interface (Thommes et al. 2015). In this work, the interface of interest is the interface between fluid molecules and mineral atoms. The fluid in bulk phase is referred to as the “adsorptive” and the sample is referred to as the

“adsorbent”. The adsorptive used in this study are nitrogen and carbon dioxide gases and adsorbents are pure crystal and solid shale.

### **2.1.2 Ultra-micro, Micro-, Meso-, and Macro-pores**

The pore sizes defined in this thesis are in accordance to the International Union of Pure and Applied Chemistry (IUPAC) (Sing et al. 1985; Thommes et al. 2015):

Ultra-micropores:  $< 0.7\text{nm}$

Micropores:  $< 2\text{nm}$

Mesopores:  $2\text{nm} - 50\text{nm}$

Macropores:  $> 50\text{nm}$

### **2.1.3 Organic Matter, Kerogen, and Bitumen**

Organic matter is dead organic material that is classified by its depositional environment such as lacustrine, marine, or terrestrial. Over time, pressure and heat convert organic matter into kerogen. As organic matter further matures under pressure and temperature, kerogen converts into bitumen, and finally into petroleum oil or gas. While kerogen is insoluble, bitumen is soluble and extractable by organic solvents. Immature kerogen tends to contain aliphatic carbon, aliphatic sulfur and oxygen containing functionalities (Pomerantz 2014). With maturation, carbon and sulfur grow into aromatic ring systems and oxygen containing functionalities cease to exist (Pomerantz 2014).

## **2.2 Background and Motivation**

Almost 80% of gas in place is stored through adsorption in shale reservoirs (Ambrose et al. 2012). The contribution of nanopores is of interest because shales have heterogenous mineral compositions and nano-scale microstructures (pore width  $< 200\text{ nm}$ ). Therefore, subcritical gas adsorption is conducted to investigate gas adsorption phenomena in nanopores (ultra-micro to

mesopores) of shales. Subcritical adsorption is a low-pressure adsorption occurring below the critical point of the fluid at a given cryogenic temperature. A cryogenic temperature (E.g. 77K for nitrogen and 273K for carbon dioxide) is maintained constant throughout the experiment as such low temperature creates exothermic reaction that causes maximum adsorption (Lowell et al. 2012).

The experimental method is based on static manometric adsorption, where a known volume of adsorptive is dosed into an already calibrated volume of sample cell containing the adsorbent at equilibrium pressure points. The gas adsorption phenomenon can be illustrated through an isotherm as shown in Figure 2.1. An isotherm describes the volume of adsorptive adsorbed as a function of increasing relative pressure (ratio of equilibrium pressure to fluid saturation pressure) at a constant cryogenic temperature. The hysteresis between the adsorption and desorption curves depends on the pore geometry of the adsorbent (Sing et al. 1985; Thommes et al. 2015).

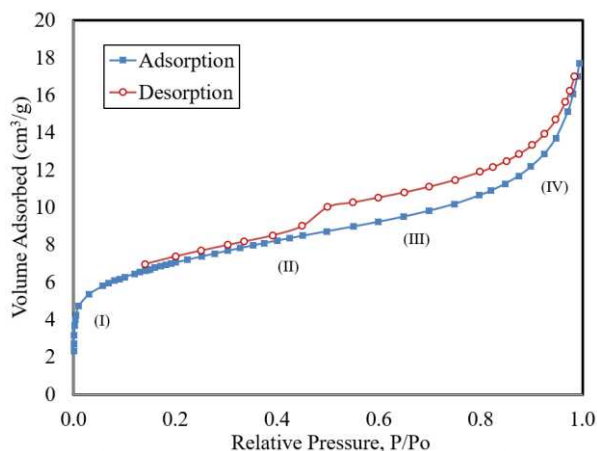


Figure 2.1: N<sub>2</sub>-adsorption isotherm of pure Na-rich Montmorillonite from Clay Minerals Society: (I) micropore filling occurs at the lowest relative pressure; (II) monolayer of adsorptive forms until the inflection point at  $P/P_o = 0.4$ ; (III) capillary condensation leads to hysteresis at the mesopores; (IV) presence of macropores is indicated by a steep curve at near-unity relative pressure (Sing et al. 1985; Kuila 2013; Thommes et al. 2015; Murugesu 2017).

Figure 2.1 shows the adsorption and desorption curves in a typical isotherm for N<sub>2</sub> adsorption.

Interpretation of an isotherm is essential to understand how useful physical properties such as pore

size distribution, porosity and specific surface area are inverted. The adsorption curve is separated into four sections numbered I, II, III and IV to individualize and illustrate the different phenomenon occurring at each region (Sing et al. 1985; Kuila 2013; Thommes et al. 2015; Murugesu 2017).

(I) **Micropore filling:** Due to stronger attraction and overlapping surface energy at narrow pores, adsorption of gas tends to begin in pore width  $< 2\text{nm}$  and in most cases completely fills the micropores (Sing et al. 1985; Storck et al. 1998; Thommes and Cychosz 2014). Micropore filling allows determination of micro-porosity and hence, the presence of micropores.

(II) **Monolayer coverage:** Due to adhesion to adsorbent, the adsorptive tends to adsorb and form monolayer on pore surfaces, ending at the sharp inflection point at relative pressure  $P/P_0=0.4$  (Kuila 2013). Monolayer coverage is used to determine the specific surface area of surfaces (Brunauer et al. 1938).

(III) **Capillary condensation:** As successive layers are formed with increasing relative pressure, the mesopores (2-50 nm) are filled, leading to capillary condensation. Due to the narrow structure of mesopores, gas molecules condense in the capillary at a pressure lower than saturation pressure of the bulk fluid (Lowell et al. 2012). Hysteresis between the adsorption and desorption curves is a result of pore condensation (Lowell et al. 2012).

(IV) **Presence of macropores:** Macropores (pore width  $> 50\text{nm}$ ) do not exhibit pore filling or condensation phenomenon. However, the presence of macropores is indicated by a steep increase in adsorbed volume at  $P/P_0 \approx 1$ , whereas a plateau at near saturation pressure indicates negligible macropores in the adsorbent (Sing et al. 1985).

The phenomena occurring during gas adsorption as described by the isotherm are result of physical interactions due to pore size distribution, and chemical interactions due to intermolecular

forces at adsorptive-adsorbent interface. In this study, pore size distribution ranges from ultra-micropore to mesopore, and can be directly inverted from the isotherm using inversion models (refer to Section 2.4.2). The intermolecular forces involved are attractive dispersive forces, short-range repulsive forces and specific molecular interactions resulting from polarization between the adsorbent and adsorptive molecules (Thommes et al. 2015). Similar physical and chemical interactions govern the transport, adsorption and storage of CO<sub>2</sub> along gas injection pathways, gas leakage pathways, and at the interface of CO<sub>2</sub> with caprock and reservoir rock with implications on CO<sub>2</sub> sequestration and enhanced oil recovery (EOR) (Gaus 2010). Therefore, information gained from subcritical adsorption can be used as first step towards understanding the chemical and physical interactions at shale - CO<sub>2</sub> interface.

## 2.3 Adsorbent and Adsorptive

### 2.3.1 Adsorbent

Characterizing reactions at the interface is demanding due to complex mineralogy of shales and therefore requires studying the reaction of the fluid with each mineral constituent to understand the bulk reaction. Therefore, the adsorbents chosen for this study are pure calcite and shales rich in certain minerals with varying organic content (0.3-12%) from Utica (U1), Green River (G1), Niobrara (N1), Bakken (B1) and Agardhfjellet (A1) formations (Table 2.1 and Table 2.2).

Table 2.1: Origin of samples

Formation	Location	Description
Utica	North America	Hydrocarbon-producing shale
Bakken	North America	Hydrocarbon-producing shale
Green River	North America	Oil Shale
Niobrara	North America	Hydrocarbon-producing chalk
Agardhfjellet	Central Spitsbergen, Norway	Potential CO <sub>2</sub> storage caprock

The samples represent a range of mineralogy: U1 contains a mixture of minerals that are commonly present in shales, making it a representative shale sample. N1 is calcite-rich, G1 is organic rich and A1 is clay-rich and organic-rich with negligible calcite content. The calcite-rich, organic-rich and clay-rich samples are compared to study the difference in CO<sub>2</sub> adsorption on each mineral. A1 and B1 are organic-rich samples with varying thermal maturity used to study CO<sub>2</sub> adsorption on organic matter.

Table 2.2: Mineralogy (XRD) of samples investigated with increasing TOC. Samples are Utica (U1), Green River Shale (G1), Niobrara (N1), Bakken (B1) and Agardhfjellet (A1).

ID	TOC	Mixed Illite/Smectite	Illite+Mica	Chlorite	Kaolinite	Total Clay	Calcite	Dolomite	Siderite	Total Carbonate
N1	0.3	2.1	1.0	0.0	0.0	3.1	88.9	1.5	0.0	90.4
U1	2.6	6.1	40.4	6.6	0.0	53.1	8.6	3.9	0.0	12.5
B1	11.9	2.6	20.3	2.6	0.0	25.5	No data			19.4
A1	12	31.7	24.6	4.8	0.0	61.1	0.0	3.4	2.6	6.0
G1	23.36	5.5	12.0	1.6	0.6	19.7	8.6	26.9	0	35.5
	Quartz	Feldspar	Plagioclase	Pyrite	Analcime	Total Other Minerals				
N1	4.7	0.0	1.2	0.6	0.0	6.5				
U1	23.3	0.6	4.9	1.9	0.0	30.7				
B1			No data			43.2				
A1	25.2	0.8	3.2	3.7	0.0	32.9				
G1	16.1	4.4	10.6	2.0	11.7	44.8				

### 2.3.2 Adsorptive

The adsorptives used are N<sub>2</sub> and CO<sub>2</sub>. N<sub>2</sub>, an inert gas, is used as a reference fluid for general pore characterization. Kinetic diameter of N<sub>2</sub> (0.36 nm) prevents it from accessing narrow micropores smaller than 0.7nm of width (Thommes et al. 2015; Joewondo 2018). On the other hand, CO<sub>2</sub> has a smaller kinetic diameter allowing its access to the ultra-micropores. The combined pore size distribution derived from CO<sub>2</sub> and N<sub>2</sub> adsorption gives the entire range from ultra-micro to mesopores. CO<sub>2</sub> adsorption is of interest to advance our understanding in CO<sub>2</sub>-shale interactions.

## 2.4 Methodology

### 2.4.1 Experimental method

The experimental steps for both N<sub>2</sub> and CO<sub>2</sub> adsorption can be separated into three steps: sample preparation, degassing and adsorption analysis (refer to Figure 2.2 for the workflow).

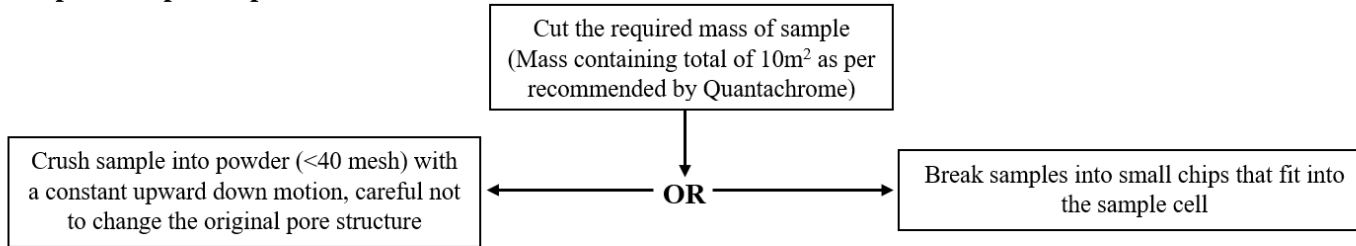
Sample preparation - The samples can either be crushed into powder and sieved with 40µm mesh or broken into pellets (Kuila and Prasad 2013). Kuila and Prasad (2013) suggests that crushing the samples reduces the length of travel for the adsorptive into the pores and allows equilibrium to be reached within a reasonable time. Equilibrium time is the time needed for adsorptive molecules to diffuse into adsorbent pores.

Degassing – Degassing ensures removal of physically adsorbed unwanted vapors and gases from the internal and external surfaces of the sample, allowing direct contact between pore walls and the adsorptive (Sing et al. 1985). During degassing, the sample chamber is connected to a vacuum source and nitrogen backfill. In this study, samples are degassed at 200°C for a minimum of 12 hours under vacuum condition (at least 10 millitorr). Care should be taken to prevent irreversible damage to the sample components with heat treatment.

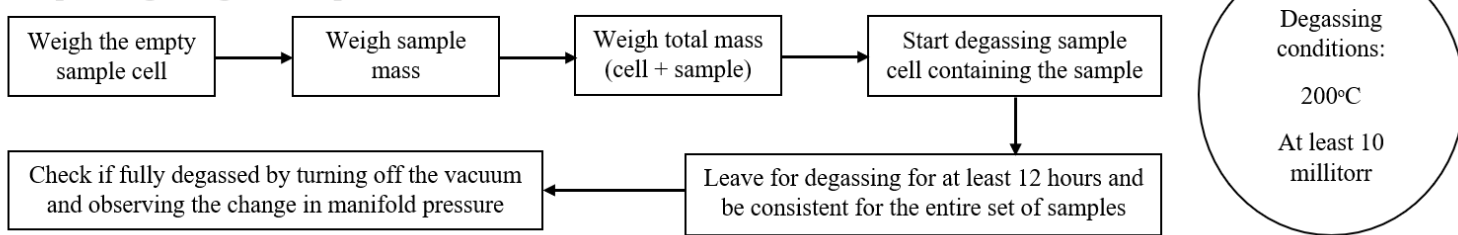
Adsorption analysis – The degassed sample is transferred to the adsorption ports. The sample cell is degassed again before dosing helium, a non-reactive gas used to measure the dead volume of the cell containing the adsorbent. Once helium is completely removed from the sample cell, the adsorptive gas is introduced, and pressure is slowly increased until saturation pressure of adsorptive is reached. As relative pressure ( $P/P_0$ ) increases, the adsorptive is adsorbed onto the sample and the reverse occurs during desorption. The volume of gas adsorbed at each relative pressure is calculated by determining the difference between the volume of gas dosed and the dead volume of sample cell.

## Workflow for Subcritical Adsorption

### Step 1: Sample Preparation



### Step 2: Degassing the sample



### Step 3: Analysis

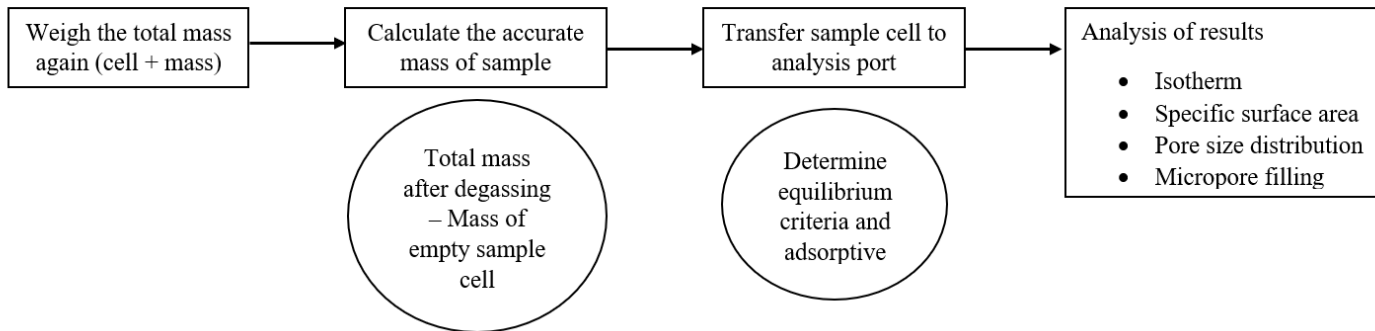


Figure 2.2: Workflow of experimental procedure breaking down the three main steps: sample preparation, outgassing the sample and analysis.

## 2.4.2 Inversion Models

Useful physical parameters of rocks such as pore size distribution, micro-porosity and specific surface area can be derived from an isotherm by applying inversion models shown in Table 2.3. The current inversion models exist for carbon, zeolite and silica, but its application to geological samples is more challenging. The various inversion methods are compared in Table 2.3 with highlights of the methods most commonly used for deriving physical information of geological samples.

Table 2.3: Inversion methods used to invert pore size distribution in micropores and mesopores, micro-porosity and specific surface area: Tick marks show the function of each inversion method and the shaded boxes show preferred methods for geological samples.

Inversion Methods	Pore Size Distribution Micropores	Pore Size Distribution Mesopores	Micro-porosity	Specific Surface Area
Brunauer-Emmett-Teller (BET)				✓
t-plot			✓	✓
Langmuir				✓
DR Method			✓	✓
Alpha-S method			✓	✓
MP Method			✓	✓
Barrett, Joyner, Halenda (BJH)		✓		✓
DH Method		✓		✓
HK Method	✓			
SF Method	✓			
DA Method	✓			
Density functional theory (DFT)	✓	✓	✓	✓
Monte Carlo	✓	✓	✓	✓

## Pore Size Distribution

Density Functional Theory (DFT)-based pore size distribution constructs the configuration of adsorbed layer at a molecular level (Thommes 2010). DFT is based on statistical mechanic method. At a molecular level, DFT models allow calculation of specific density of the adsorbed fluid in the pore space at a given temperature and equilibrium pressure (Thommes 2010; Landers et al. 2013). The major advantage of DFT compared to the commonly used BJH lies in its ability to quantify relative volumes of micro- and mesopores. Several kernels are available for DFT analysis. The kernel used for this specific analysis is the QSDFT kernel on carbon with slit cylindrical pores on adsorption branch, and the pore size distribution is displayed as differential pore volume (cc/g/nm) to better represent the micropores (Joewondo 2018). DFT kernels for general pore characterization are explained by IUPAC technical report in 2015 (Thommes and Cychosz 2014; Thommes et al. 2015). The use of DFT for geological samples has been discussed by Clarkson et al. (2012), Wei et al. (2016), Lingling et al. (2017) and Joewondo (2018).

## Specific Surface Area

The Brunauer-Emmett-Teller (BET) method allows us to estimate monolayer specific surface area from the isotherm based on several assumptions. First, monolayer coverage is expected to occur at relative pressure ranging from 0.05 to 0.35. At this range, the BET plot ( $P/n(P_0-P)$  vs.  $P/P_0$ ) is typically linear with a positive intercept,  $C$ , as shown by (Rouquerol et al. 2013). The molecules cover the surface of the adsorbent uniformly, but the BET specific surface area ( $a_s$ ) varies depending on the molecular cross-sectional area ( $\sigma_m$ ) (Rouquerol et al. 2013). The equation governing BET specific surface area is expressed as Equation 2.1 (Thommes et al. 2015):

$$a_s(\text{BET}) = n_m * L * \sigma_m / m \quad (2.1)$$

## Micropore Filling

The statistical t-plot method determines the volume of micropores based on the conversion of relative pressure ( $p_0/p$ ) to thickness of the adsorbate ( $t$ ) (de Boer et al. 1966; Voogd et al. 1991). The conversion is automatically calculated by programs installed for the adsorption analysis with the statistical thickness equation expressed as Equation 2.2:

$$t = \left[ \frac{13.99}{\log\left(\frac{P_0}{P}\right)} + 0.034 \right]^{0.5} \quad (2.2)$$

Volume of the adsorptive adsorbed is plotted against statistical thickness to obtain a linear range. The slope of the linear line corresponds to external surface area, and the intercept corresponds to micropore volume (Remy and Poncelet 1995). The micropore volume can also be validated by the isotherm shape at the low end of relative pressure. The volume of adsorbate at the low relative pressure reflects micropore volume since micropore filling mostly governs adsorption at this pressure range. MP (micropore analysis) method is an extension of the de Boer statistical t-plot (refer to Lowell et al. (2012) for a comprehensive discussion of micropore analysis).

### 2.4.3 CO<sub>2</sub> adsorption

Various studies have addressed the application of N<sub>2</sub> or Ar adsorption to geological samples. I performed CO<sub>2</sub> adsorption for two reasons: (i) to study the ultra-micropores on geological samples due to the increasing interest in quantifying the contribution of this range of pores to storage capacity (also addressed by Joewondo (2018)), and (ii) to gain insights on CO<sub>2</sub>-shale interactions. Through repeated runs, I identified that subcritical adsorption at micropore scale is sensitive to equilibrium criteria and sample mass. Discussion below shows the discrepancies resulting from using inconsistent equilibrium criteria and sample mass, hence I recommend consistency.

Equilibrium criteria: Prior to each CO<sub>2</sub> test, relative pressure steps from 0 to  $\approx 0.03$  are manually input into the program. At each relative pressure, the instrument doses gas until the pre-determined relative pressure is nearly achieved. Then, the cell pressure is closely monitored for set equilibrium time for variation of current pressure from set tolerance (0.05% was used for all cases in this work). If current pressure varies more than the tolerance, the final volume of gas adsorbed for the specific relative pressure step will only be recorded after a timeout period. Table 2.4 shows three sets of equilibrium criteria in the order of tighter conditions, as tested on U1 sample. U1 is chosen as a representative shale sample due to its encompassing composition of minerals.

Table 2.4: Equilibrium Criteria Tested

Number	Timeout (seconds)	Equilibrium (seconds)
1	800	400
2	1000	600
3	1400	1000

Table 2.5 shows the total adsorbed volume derived from isotherms and the cumulative pore volume derived from DFT pore size distribution. The total volume from isotherm and pore size distribution do not match. Unlike the isotherm-determined volume, the DFT-determined pore volume is specific to pore geometry and disregards the adsorption on external pore surfaces. The standard deviations confirm the discrepancies caused by using different equilibrium criteria. Tighter equilibrium condition renders better accuracy but leads to an unnecessarily long analysis time. For the purpose of the thesis, I consistently used shortest equilibrium criteria (timeout = 800 s, equilibrium = 400 s) to reduce the duration of analysis.

Table 2.5: Cumulative pore volume of U1 for equilibrium criteria: timeout =800 s and equilibrium =400 s, timeout =1000 s and equilibrium =600 s, timeout =1400 s and equilibrium =1000 s.

Equilibrium Criteria	Total volume Adsorbed (cm <sup>3</sup> /g)	Cumulative Pore Volume (cm <sup>3</sup> /g)
Timeout=800s and Equilibrium=400s	2.72	0.00023
Timeout=1000s and Equilibrium=600s	2.76	0.00025
Timeout=1400s and Equilibrium=1000s.	2.94	0.00029
<b>Standard Deviation</b>	<b>0.11</b>	<b>0.00003</b>

Adsorbent Mass: Figure 2.3(a) shows the adsorption capacity due to different mass ( $M_1 = 2.310$  g &  $M_2 = 3.724$  g) for G1 (Green River Shale). G1 was chosen for this purpose based on availability. The instrument provider recommends filling the sample tube with mass that has minimum of  $10 \text{ m}^2$ . Thus, G1 with a specific surface area of  $0.582 \text{ m}^2/\text{g}$  requires a total mass of  $\approx 20$  g for the analysis. Such a large mass will not fit in the sample tube and will prolong the analysis time. Therefore, for samples with low specific surface area such as shales, I recommend using minimum of 3.5 g which will sufficiently fill the sample cell without exceeding the cell limit. The measurements with different masses of G1 do not show significant variance in the pore size distribution according to Figure 2.3(b), ruling out the effect of sample mass on pore volume determination. The total volume adsorbed varies in the isotherms because more adsorptive is likely adsorbed to the external surface area of the larger sample. I used a constant mass of  $(2.5 \pm 0.3 \text{ g})$  for this study to prevent bias towards sample mass.

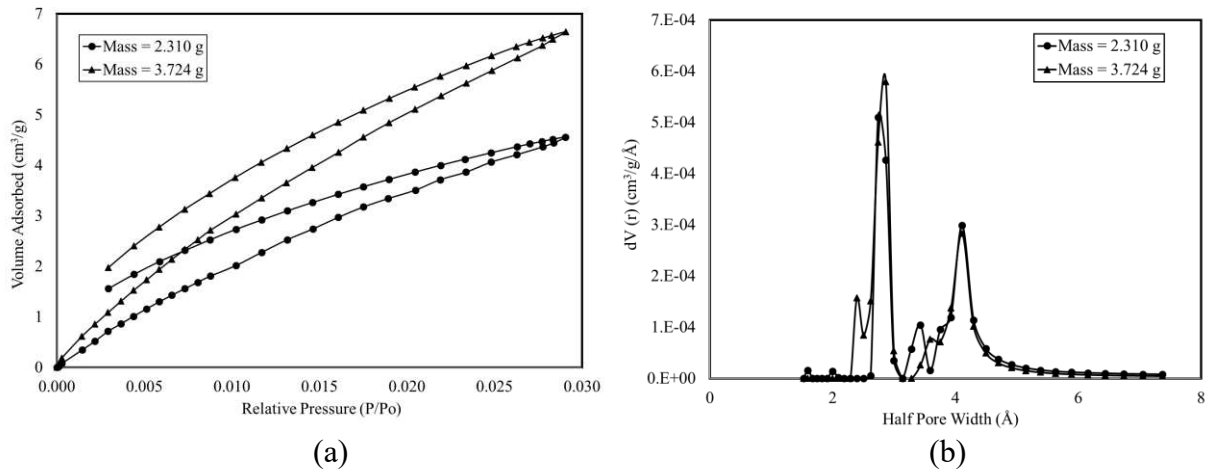


Figure 2.3: a) Adsorption capacity, and b) pore size distribution of G1 (Green River Shale) of different masses. Although the higher mass sample causes the total volume adsorbed to be nearly double in the isotherm, the different masses do not cause significant variance in the pore size distribution.

## Results and Discussions

### 2.5 CO<sub>2</sub>-shale reactions

The motivation of this chapter is to derive useful chemical and physical interactions of CO<sub>2</sub> with shale. Due to complexity of shale composition, I investigated the contribution of shale minerals by studying samples rich in specific mineral such as (i) calcite, (ii) clay, and (iii) organic matter.

#### 2.5.1 CO<sub>2</sub>-calcite rich shale

Calcite is a common reactive carbonate mineral in shales. While permanent storage of CO<sub>2</sub> is possible through mineral carbonation of calcium silicate into calcium carbonate (calcite), this study shows additional storage is attainable through calcite-CO<sub>2</sub> interaction. The sample studied for this purpose is N1 (88.9% calcite by weight).

Figure 2.4 shows the isotherms of N1. The initial analysis (Test 1) shows hysteresis between adsorption and desorption curves, suggesting possible entrapment of CO<sub>2</sub>. To confirm the

occurrence, the analysis was repeated without intermediate degassing step. The total adsorption capacity of CO<sub>2</sub> decreased for each consecutive step, suggesting some CO<sub>2</sub> dosed in previous steps may be residing in the existing pores and blocking additional CO<sub>2</sub> from accessing the pores. After three repeated runs, N1 shale was degassed again at 200°C under vacuum to remove any trapped CO<sub>2</sub>. However, the total adsorption capacity of N1 did not return to its original value. The low TOC content of N1 makes it improbable that CO<sub>2</sub> was trapped by organic matter. The isotherms of calcite-rich N1 is neither reversible nor recoverable, indicating permanent storage of CO<sub>2</sub> in the micropores.

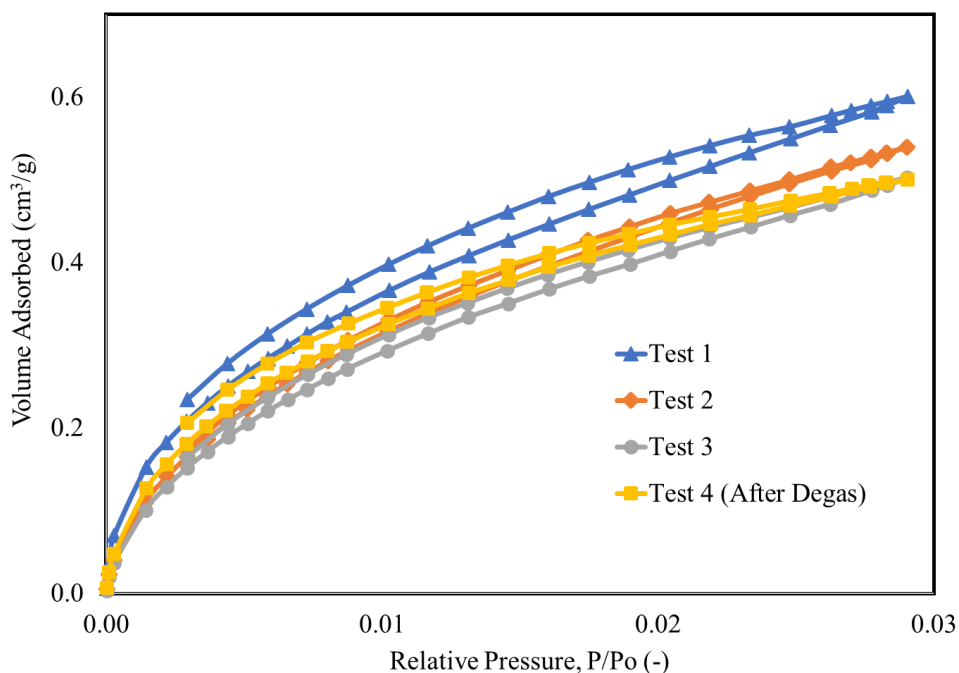


Figure 2.4: The isotherms obtained from CO<sub>2</sub> adsorption on Niobrara N1 (88.9% calcite content): First CO<sub>2</sub> run (Test 1) shows an open hysteresis, indicating possibly trapped CO<sub>2</sub> during the test. As subsequent tests are conducted, the total adsorption capacity gradually decreased due to the CO<sub>2</sub> molecules already occupying the existing pores. After degassing the sample again to remove all trapped gas, test 4 shows similar open hysteresis as test 1, but its total adsorption capacity did not return to the original capacity. This suggests that some CO<sub>2</sub> is permanently trapped in the pores after test 1.

## 2.5.2 CO<sub>2</sub>-organic rich shale

CO<sub>2</sub> preferentially adsorbs to organic matter compared to inorganic minerals of shales, and the fine pores of organic matter have large capacity for CO<sub>2</sub> storage (Edwards et al. 2015; Zargari et al. 2015). The nature of organic matter presents motivation for careful study of CO<sub>2</sub>-organic rich shale reactions.

The test sequence as shown for N1 is repeated for sample G1 from Green River shale (23.3% organic matter by weight). Figure 2.5 shows the isotherms for G1, where the hysteresis in the initial run shows possible entrapment of CO<sub>2</sub>. G1 also follows similar trend of decreasing adsorption capacity with repeated runs. As opposed to N1, the adsorption capacity of G1 returned to its original value after degassing the sample again. While the isotherms of G1 are not reversible, they are recoverable.

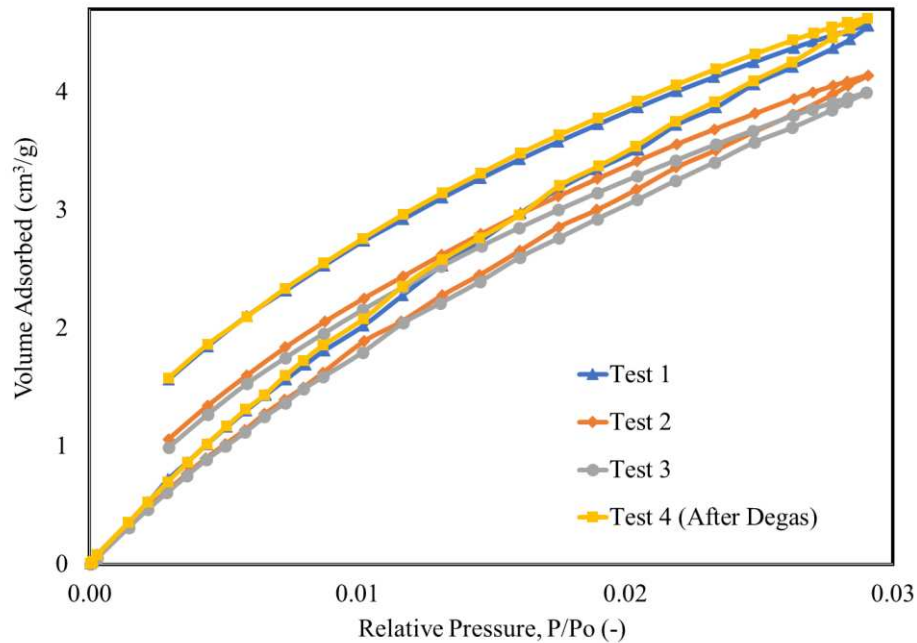


Figure 2.5: CO<sub>2</sub> adsorption on organic-rich G1 (Green River Shale): First CO<sub>2</sub> run (Test 1) shows an open hysteresis, indicating possibly trapped CO<sub>2</sub> during the test. As subsequent tests are conducted, the total adsorption capacity gradually decreased. After degassing the sample again to remove all trapped gas, its total adsorption capacity returned to original capacity. CO<sub>2</sub> is not permanently trapped in the pores.

### 2.5.3 CO<sub>2</sub>-clay rich shale

Clay minerals have fine pores and large specific surface area for adsorption. Studies have also indicated potential clay mineral swelling with CO<sub>2</sub> sorption (Busch et al. 2010). A clay rich sample A1 (61.1% clay and 12% TOC) from Agardhfjellet formation was chosen for this purpose and the isotherms are shown in Figure 2.6. The isotherms do not show a successive decrease in adsorption capacity with consecutive runs. The isotherms of A1 are both reversible and recoverable.

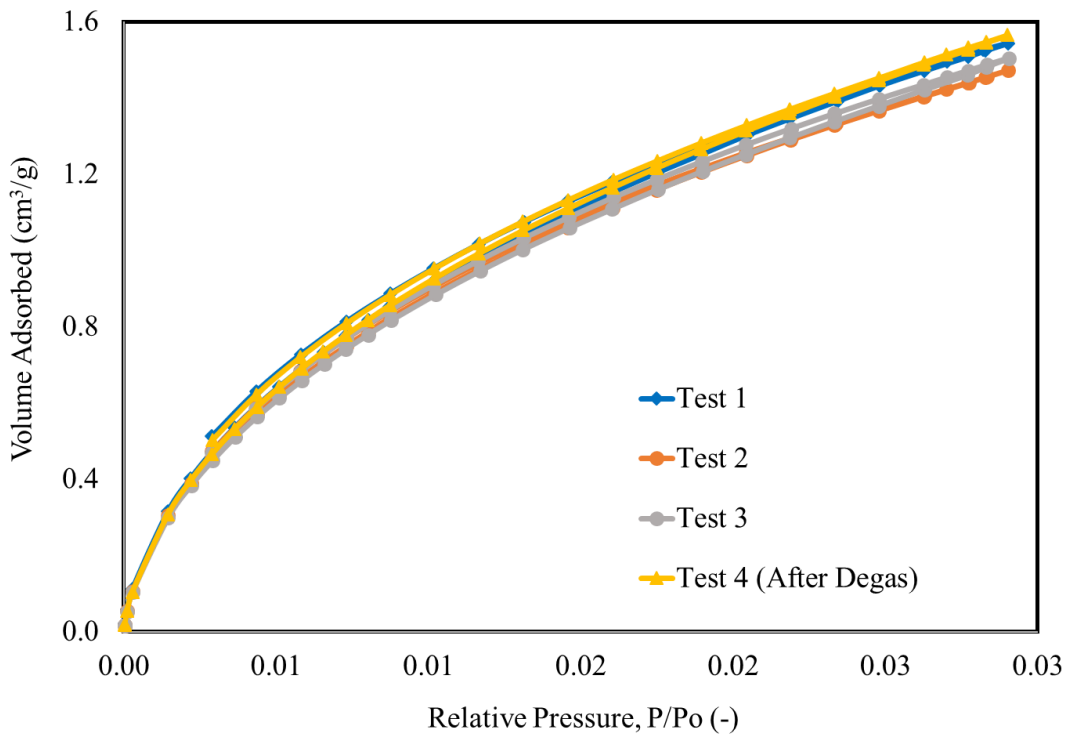


Figure 2.6: CO<sub>2</sub> run on clay-rich A1 (Agardhfjellet): A1 contains 61.1% of clay, 6% of carbonate and 12% of organic content. No successive decreasing adsorption capacity is observed for A1 with consecutive runs. Hence, CO<sub>2</sub> is not trapped in the pores at any point of the runs.

### 2.5.4 Calcite-CO<sub>2</sub> Reaction

Note that the y-axis scale of each shale is different to magnify the characteristic isotherm of each sample. From comparing calcite-rich N1, organic-rich G1 and clay-rich A1, N1 is

interesting because the isotherms are not recoverable, leading to permanent storage of CO<sub>2</sub> in the pores of calcite-rich shale. One theory that explains permanent storage of CO<sub>2</sub> in the calcite-rich N1 is possible dissolution of CO<sub>2</sub> in the chemisorbed water in calcite minerals.

The surface of calcite has chemisorbed water that leaves the sample only when heated to 600°C under vacuum as shown in Figure 2.7 (Morimoto et al. 1980). I tested the effect of chemisorbed water in calcite at different temperatures (200°C and 400°C). At a degassing temperature of 200°C, I observed hysteresis in the isotherm with a negative initial adsorption, indicating possible dissolution of CO<sub>2</sub> (Figure 2.8). To confirm this observation and hypothesis, I increased the degassing temperature from 200°C to 400°C. At the higher degassing temperature, pure calcite mineral shows a positive uptake and adsorbs more CO<sub>2</sub>. As the degassing temperature is increased, more chemisorbed water detaches from calcite, lowering CO<sub>2</sub> dissolution. Consequently, CO<sub>2</sub> adsorbs to the newly exposed mineral surfaces as indicated by the increased amount of adsorption in Figure 2.8.

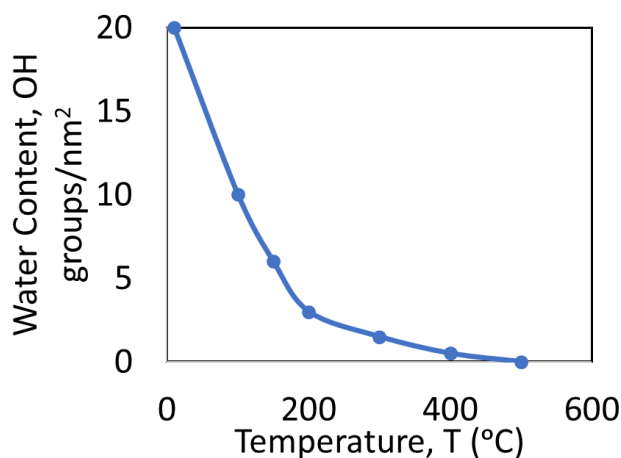


Figure 2.7: Water content on calcite as a function of temperature (modified from Morimoto et al. 1980).

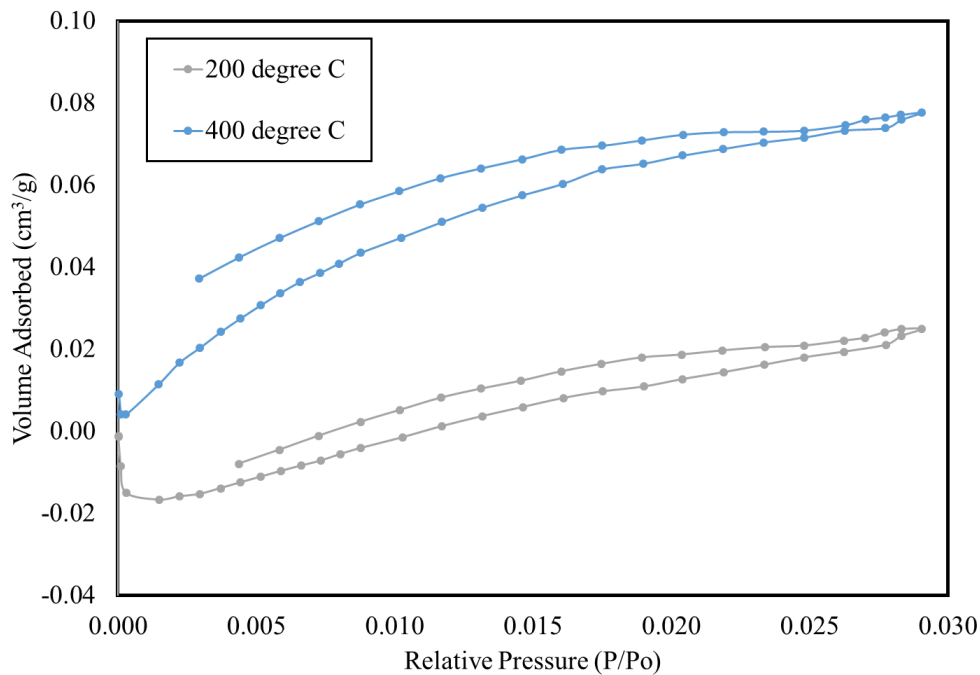


Figure 2.8: Isotherm of pure calcite minerals at degassing temperatures of 200°C (grey dots) and 400°C (blue dots). The initial negative volume adsorbed for pure calcite at 200°C indicates possible dissolution of CO<sub>2</sub> into the chemisorbed water. When temperature was increased to 400°C, the initial volume drop was lesser than at 200°C and did not fall on negative scale. At 400°C, chemisorbed water has mostly evaporated, lowering CO<sub>2</sub> dissolution. The adsorption capacity after degassing at 400°C is higher as the CO<sub>2</sub> adsorbs to pore surfaces instead of dissolving in chemisorbed water.

### 2.5.5 Implication for CO<sub>2</sub> Storage

CO<sub>2</sub> trapped in calcite-chemisorbed water has implication for total CO<sub>2</sub> storage capacity of calcite-rich reservoir and cap-rocks. Figure 2.9 shows that CO<sub>2</sub> trapped in calcite minerals is most likely located in the ultra-micropores, due to the decreasing number of ultra-micropores with repeat measurements at pore width ranging from 2Å to 4Å (0.4nm to 0.8nm). Chemisorbed water is expelled from the larger pores before the smaller pores in minerals. Due to stronger attraction forces in the smaller pores, higher temperatures are required to overcome the attraction between the water and pore wall at this pore region. CO<sub>2</sub> possibly dissolves and remains in the ultra-micropore region, blocking gas from entering these pores in subsequent runs. Interestingly, the

trapped CO<sub>2</sub> in sample N1 (Figure 2.4 & Figure 2.9) was not expelled completely from the sample upon second degassing (test 4), suggesting permanent trapping. It is important to understand the implication of CO<sub>2</sub> trapped in the ultra-micropore.

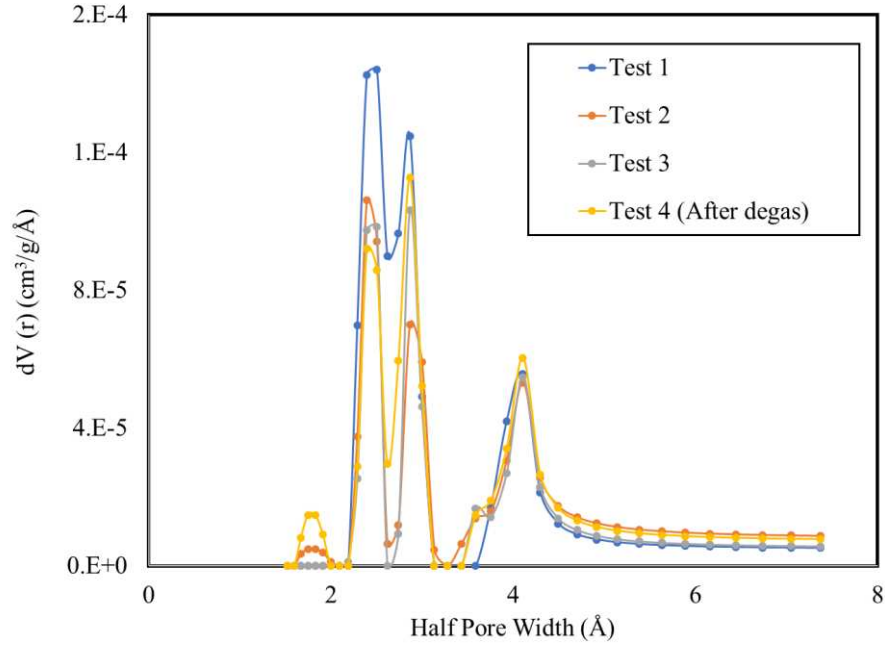


Figure 2.9: Pore size distribution of calcite-rich N1 with different runs. Pore size distribution of N1 shows that decreasing presence of pores from 2Å to 4Å causes the decreasing trend of CO<sub>2</sub> adsorption capacity in N1 isotherm. Thus, CO<sub>2</sub> is possibly trapped in the pore range of 2Å to 4Å (ultra-micropores) between test 1 and test 4.

With the difference in cumulative pore volume obtained from test 1 and test 4 in sample N1 (Figure 2.9), I have shown the volume of CO<sub>2</sub> trapped in the ultra-micropore region for a given volume of reservoir (refer to Table 2.6). For the purpose of determining the CO<sub>2</sub> storage capacity, I used Equation 2.3:

$$\text{storage capacity} \left[ \frac{\text{kgCO}_2}{\text{m}^3_{\text{rock}}} \right] = \rho_{\text{shale}} \left[ \frac{\text{g}}{\text{cm}^3} \right] \times \text{micropore volume} \left[ \frac{\text{cm}^3}{\text{g}} \right] \times \rho_{\text{CO}_2} \left[ \frac{\text{g}}{\text{cm}^3} \right] \times 1000 \frac{\text{kg/m}^3}{\text{g/cm}^3} \quad (2.3)$$

Assumptions for this equation are: (i) CO<sub>2</sub> fills the effective ultra-micropore volume completely, (ii) shale density estimate ( $\rho_{shale}$ )= 2.4 g/cm<sup>3</sup>, and (iii) density of CO<sub>2</sub> liquid = 0.7 g/cm<sup>3</sup> at 30 °C and 8 MPa (van der Meer et al. 2005).

Table 2.6: Volume of CO<sub>2</sub> trapped in the ultra-micropore region for the given volume.

Area	Thickness	Differential Pore volume (cm <sup>3</sup> /g)	Storage Capacity
1 Acre	1 ft	2.63E-05	0.10 Tonnes/acre ft
10 km <sup>2</sup>	100 m	2.63E-05	82.98 Kilotonnes/km <sup>3</sup>

The volume of CO<sub>2</sub> trapped in this pore structure also has implication in CO<sub>2</sub>-EOR processes, where the given volume of injected CO<sub>2</sub> may not be recoverable during production. Thus, pore structure of formations evaluated for potential CO<sub>2</sub>-EOR studies must be carefully characterized.

## 2.6 CO<sub>2</sub> Adsorption on Organic Matter

Comparing the three shales with distinct mineralogy, organic-rich G1 has the highest adsorption capacity, followed by clay-rich A1 and calcite-rich N1 (refer to Figure 2.10). Observation in Figure 2.10 garners interest in organic matter for CO<sub>2</sub> storage purposes. Both chemical and physical behavior of organic matter affects preferential adsorption of CO<sub>2</sub>. Chemically, CO<sub>2</sub> is known to have affinity towards organic matter than inorganic minerals in shales (Edwards et al. 2015). Physically, the large amount of ultra-micropores in kerogen allows for higher adsorption of CO<sub>2</sub> into the pores. This section characterizes the distribution of organic matter in shales, of particular interest is quantification of pore volume in organic matter to determine CO<sub>2</sub> storage capacity. Direct inversion of the chemistry of organic matter is limited using subcritical gas adsorption, but possible explanations are presented throughout the discussion.

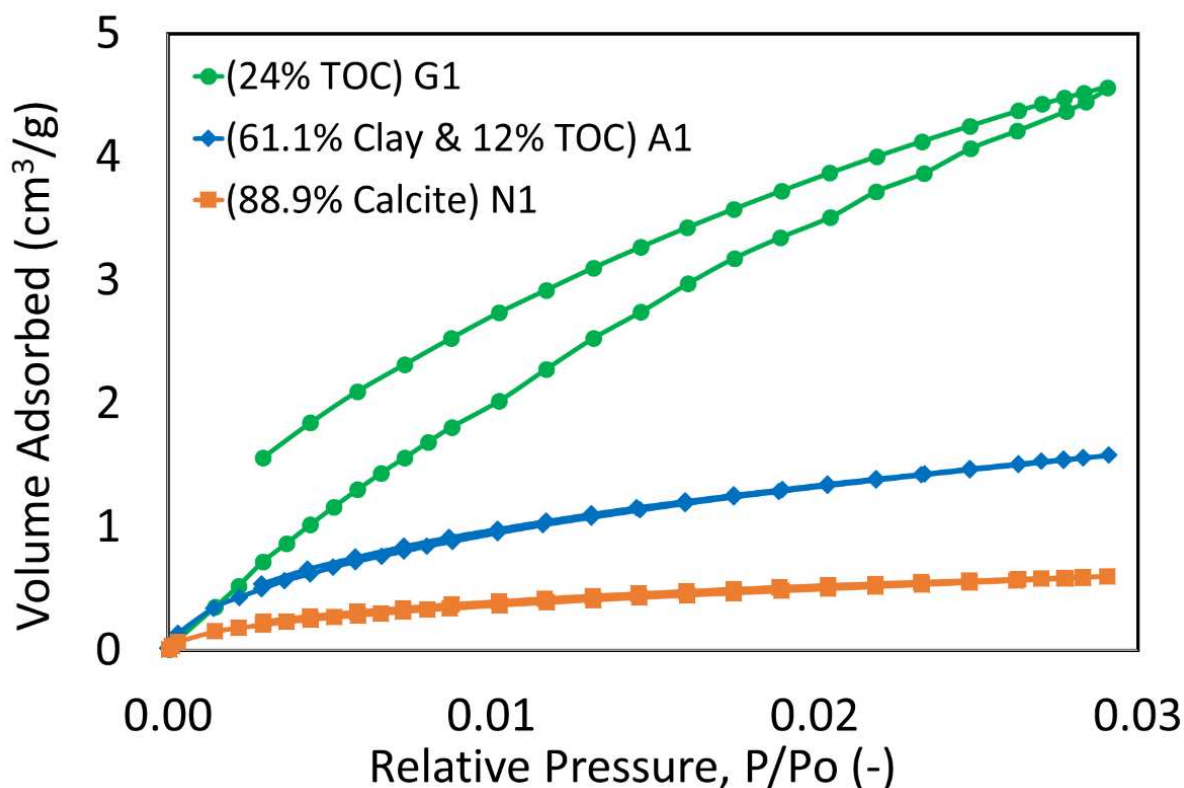


Figure 2.10: The adsorption capacity of organic-rich G1 is the highest, followed by clay-rich A1 and calcite-rich N1.

I conducted low pressure adsorption of CO<sub>2</sub> and N<sub>2</sub> onto organic-rich Agardhfjellet (A1) and Bakken (B1) samples. The Rock-Eval for the samples are shown in Table 2.7. CO<sub>2</sub> adsorption provides pore size distribution (PSD) at 0.25-0.7 nm of pore diameter, whereas nitrogen provides PSD at the mesopore range (0.7nm – 50nm). The combined PSD obtained from CO<sub>2</sub> and N<sub>2</sub> adsorption shows the complete pore size distribution from the ultra-micropore to mesopore, which is the primary pore size range in kerogen (Nuttall et al. 2005; Chalmers and Bustin 2007a; Chalmers and Bustin 2007b; Zhang et al. 2012; Kuila 2013; Joewondo 2018).

Table 2.7: RockEval for organic-rich A1 and B1.

Sample ID	Formation	TOC	HI	OI	T <sub>max</sub> (°C)	S1	S2	S3
A1	Agardhfjellet	11.97	94	0	472	2.61	11.30	0.05
B1	Bakken	11.90	345	2	443	0.15	38.71	0.26

In addition to studying the pore size distribution, I distinguished soluble (bitumen) from insoluble organic matter (kerogen) by extracting bitumen using solvents such as toluene and chloroform. By removing bitumen, we gain insights on the locations of soluble organic matter, which shows the dominant pore sizes of kerogen. As organic matter thermally matures, it enters oil window, generating bitumen that resides in the kerogen-hosted pores and blocks CO<sub>2</sub> from accessing the pores during adsorption study (Kuila 2013; Zargari et al. 2015). Once bitumen is removed, the pores that were previously blocked appear in the pore size distribution, indicating kerogen pore type.

Solvent extraction has been employed in the past by Zargari et al. (2015) to show effective porosity and the distribution of organic matter in shales by measuring N<sub>2</sub> adsorption. In this study, I measured both N<sub>2</sub> and CO<sub>2</sub>-adsorption to learn the effects of soluble organic matter removal on the ultra-micropore region and how that affects CO<sub>2</sub>-storage capacity in kerogen-hosted pores. Note that both samples have similar total organic carbon (TOC). The Agardhfjellet (A1) is slightly more matured at post oil-window (type III kerogen) compared to Bakken (B1) at early oil-window (%R<sub>o</sub> = 0.81) (Koevoets et al. 2016).

Solvent-extraction method: Shale samples are extracted using toluene for 48 hours, followed by chloroform for another 48 hours. Solubility of bitumen in toluene and chloroform is more than 90% (Huang and Holm 1998). The physical properties of the solvent are shown in Table 2.8.

Table 2.8: Physical Properties of Organic Solvents (Zargari et al. 2015).

Solvent	Polarity	Boiling Point (°C)	Solubility in Water (25°C %w/w)
Toluene	9.9	110.6	0.052
Chloroform	25.9	61.0	0.820

Almost 15 grams of sample was crushed into powder and sieved with a 40 $\mu$ m mesh. Aliquots (~3g) were collected from the total sample mass prior to extraction, after toluene extraction and after chloroform extraction. For each set of samples, both N<sub>2</sub> and CO<sub>2</sub> adsorptions were conducted. Figure 2.11 shows the solvent extraction set-up for powder samples, where the sample is kept in a cellulose and covered with cotton balls.

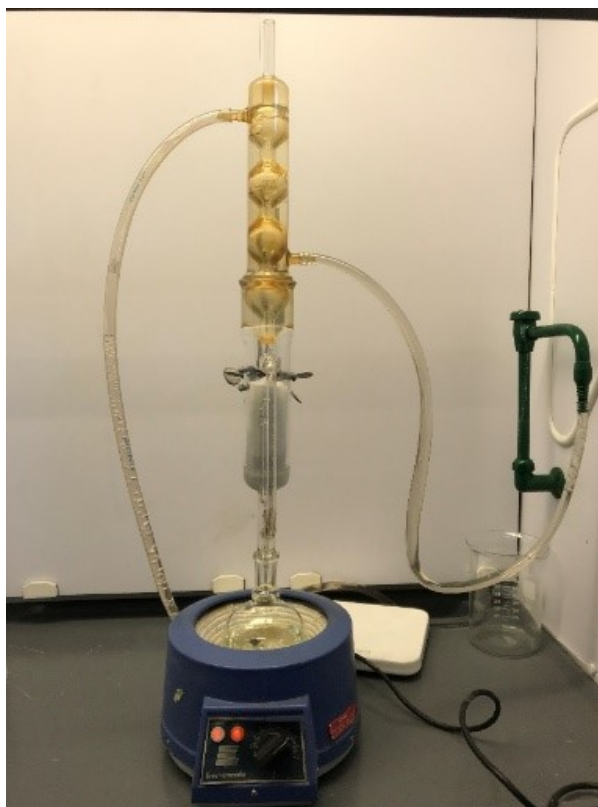


Figure 2.11: Solvent extraction set-up for powder sample. The powder is placed in a cellulose and cotton balls are placed at the mouth of the cellulose, preventing the sample from overflowing.

Findings: Table 2.9 shows the specific surface area (SSA) exposed for adsorption for A1 and B1 before and after extraction. Note that the general SSA for A1 is larger than B1 and the total volume of CO<sub>2</sub> and N<sub>2</sub> adsorbed as shown by isotherms of A1 (Figure 2.12) is larger than the volume adsorbed by B1 (Figure 2.13). The difference in volume adsorbed despite having similar total organic content can be attributed to the chemistry of the samples. Agardhfjellet (A1) is more mature than Bakken (B1). Higher thermal maturity and the aromatic hydrocarbon present on kerogen type III enhances adsorption capacity of A1 shale (Zhang et al. 2012; Koevoets et al. 2016).

We expect SSA to increase after extraction of soluble organic matter because pores that were previously blocked by bitumen is now exposed to gas molecules (Zargari et al. 2015). The pores are also determined to be micropores due to the increase in this pore sizes with subsequent solvent extraction (Figure 2.14 and Figure 2.15). Interestingly, the SSA declined for B1 after chloroform extraction. Similar observation is made on some samples investigated by Zargari et al. (2015). Without existing evidence to why that may occur, I assume that some minerals in the pores are dissolving in chloroform and get redeposited back into the pores due to inefficient extraction. Therefore, the chloroform extraction method needs to be further investigated.

Table 2.9: Specific surface area exposed to adsorption for A1 and B1 determined using N<sub>2</sub> adsorption.

Extraction Process	Specific Surface Area, SSA (m <sup>2</sup> /g)	
	A1 (gas window)	B1 (oil window)
Before Extraction	17.249	0.953
Toluene Extraction	25.498	1.501
Chloroform Extraction	25.711	1.163

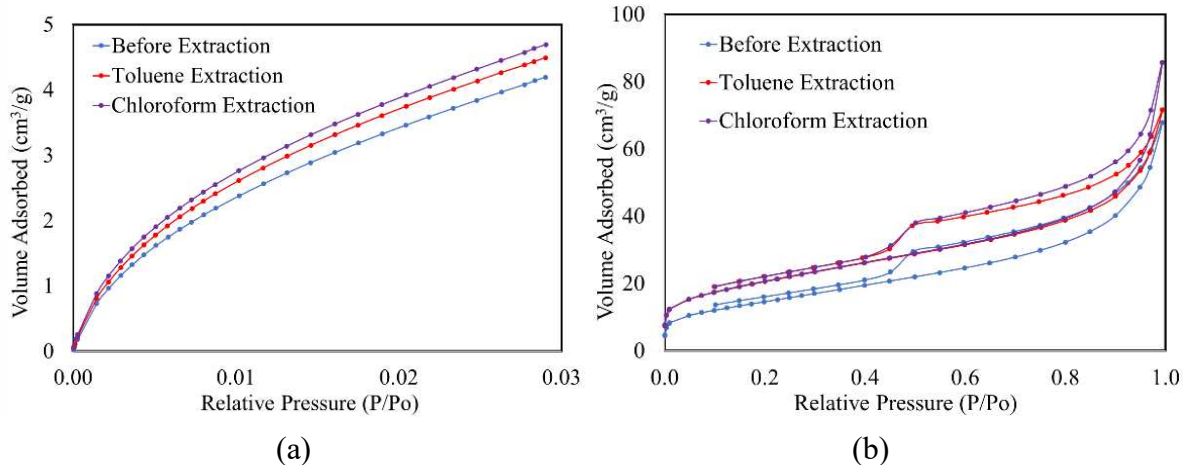


Figure 2.12: (a) CO<sub>2</sub> adsorption isotherms of sample A1 showing increased adsorption capacity at the micropore level after extraction of soluble organic matter. (b) N<sub>2</sub> adsorption isotherms showing increased adsorption capacity at micropore (low relative pressure range) after toluene and chloroform extraction. It continued to increase at macro-pores (high relative pressure range) with chloroform extraction.

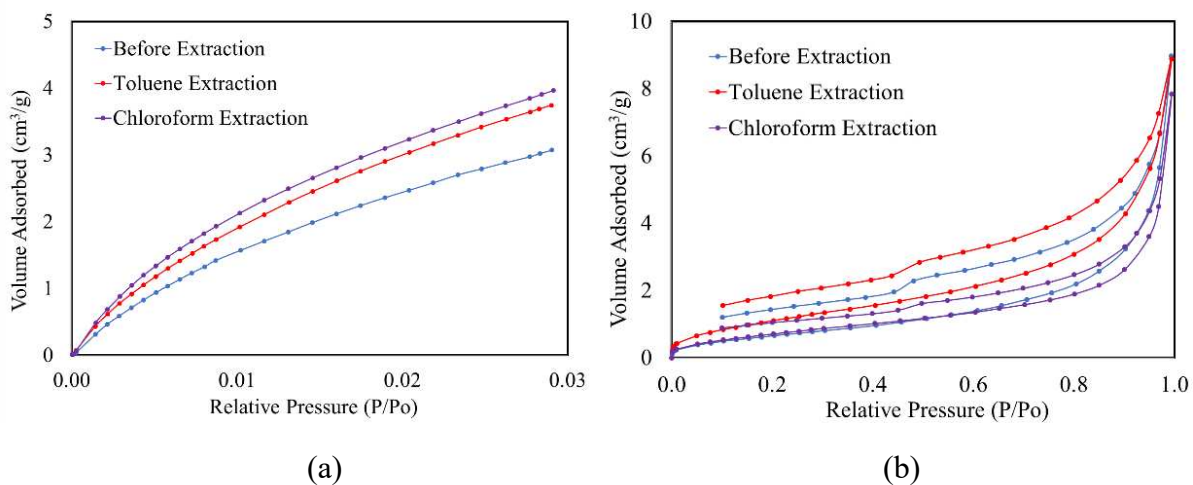


Figure 2.13: CO<sub>2</sub> adsorption isotherms of sample B1 showing increased adsorption capacity at the micropore level after extraction of soluble organic matter. (b) N<sub>2</sub> adsorption isotherms showing increased adsorption capacity at micropores (low relative pressure range) after toluene extraction and increased adsorption at macro-pores (high relative pressure range) after chloroform extraction.

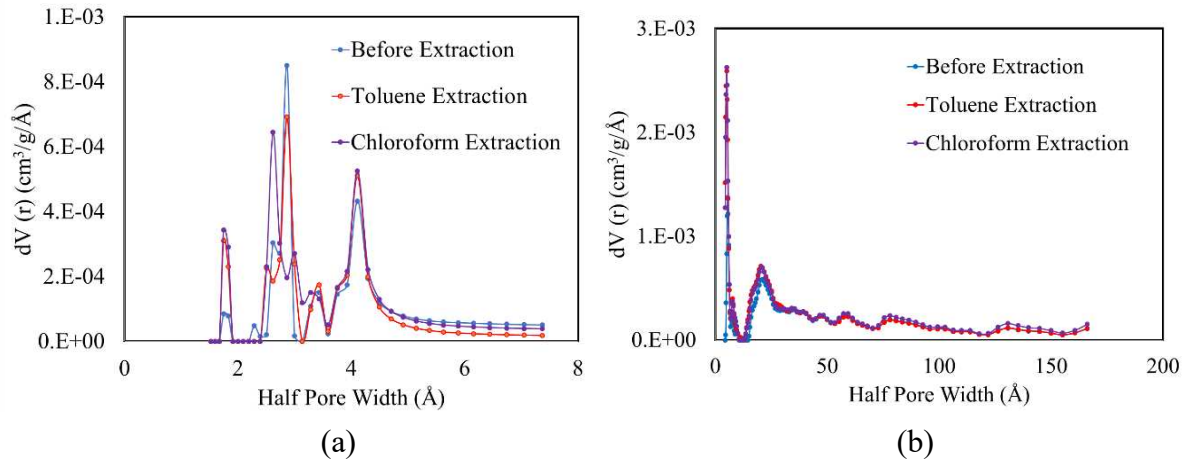


Figure 2.14: (a) The pore size distribution obtained at the ultra-micropore level for sample A1. (b) The pore size distribution from micro- to mesopore range using N<sub>2</sub> adsorption.

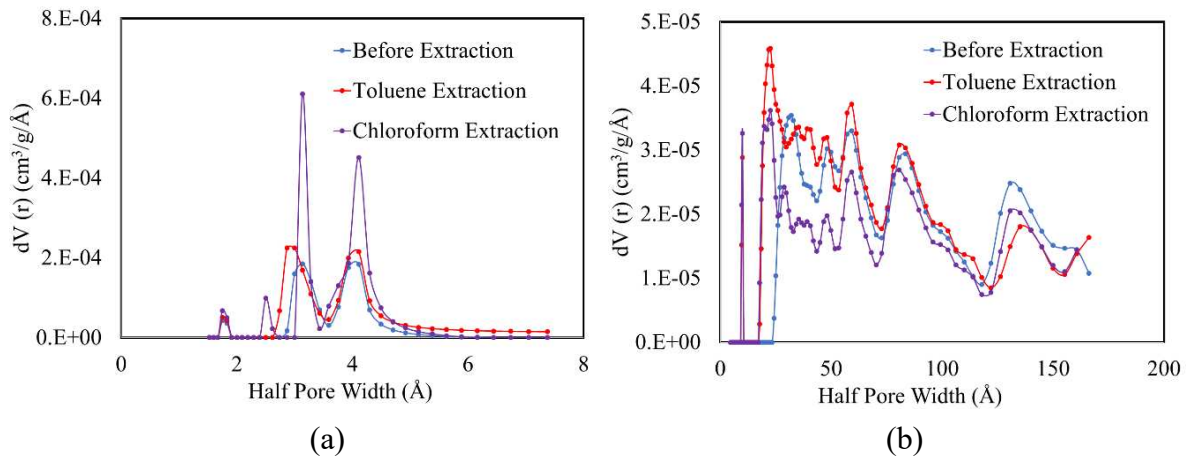


Figure 2.15: (a) The pore size distribution obtained at the ultra-micropore level for sample B1. (b) The pore size distribution from micro- to mesopore range using N<sub>2</sub> adsorption.

Cumulative pore volumes of the samples are obtained from (i) ultra-micropore to mesopore range by combining CO<sub>2</sub> adsorption and N<sub>2</sub> adsorption, and from (ii) ultra-micropore region alone using CO<sub>2</sub> adsorption (Table 2.10). The increase in cumulative pore volume shows the pores emptied after soluble organic matter is removed. In natural reservoir system, the soluble bitumen will eventually pass post-mature stage, entering gas window and possibly evacuating the kerogen

pores. The time it takes for the process to take place depends on the pressure and temperature of the formation. Quantifying the pore volume filled by bitumen provides knowledge on possible volume of CO<sub>2</sub> that can be trapped by organic matter when the formation has passed post-mature stage.

Table 2.10: The cumulative pore volume obtained from (CO<sub>2</sub> adsorption+N<sub>2</sub> adsorption), and CO<sub>2</sub> adsorption of A1 and B1 after sequential removal of soluble organic matter.

Extraction Process	(CO <sub>2</sub> +N <sub>2</sub> )-Derived Cumulative Pore Volume (cc/g)	
	A1 (gas window)	B1 (oil window)
Before Extraction	0.0260	0.0031
Toluene Extraction	0.0302	0.0035
Chloroform Extraction	0.0329	0.0030
Extraction Process	CO <sub>2</sub> -Derived Cumulative Pore Volume (cc/g)	
	A1 (gas window)	B1 (oil window)
Before Extraction	0.0006	0.0002
Toluene Extraction	0.0006	0.0003
Chloroform Extraction	0.0007	0.0003

For the purpose of determining CO<sub>2</sub> storage capacity, I used Equation 2.3 described in previous section. Similar assumptions of shale and CO<sub>2</sub> density are applied. The reference storage capacity for this calculation is obtained from Nuttall et al. (2005) for Devonian shales in Kentucky that shows potential storage of 28 Gigatonnes of CO<sub>2</sub>. Assuming similar volumetric properties used for the reference formation, the areal distribution and thickness for our calculation is set to be 37500 km<sup>2</sup> and 50 m respectively (Ettensohn et al. 1988). Table 2.11 shows the estimated storage capacity.

Table 2.11: CO<sub>2</sub> storage capacity estimated for cumulative pore volumes shown in Table 2.10: CO<sub>2</sub>-derived pore volume + N<sub>2</sub>-derived pore volume, compared with CO<sub>2</sub>-derived pore volume. Pore volume refers to cumulative pore volume obtained during adsorption at ultra-micropore (CO<sub>2</sub>) and ultra-micropore to mesopore (CO<sub>2</sub>+N<sub>2</sub>).

	Adsorption	Pore volume (cc/g)	Storage Capacity (Gigatonnes)	Pore volume (cc/g)	Storage Capacity (Gigatonnes)
Before Extraction	CO <sub>2</sub> +N <sub>2</sub>	0.0260	81.9	0.0031	9.8
	CO <sub>2</sub>	0.0006	1.9	0.0002	0.6
Toluene Extracted	CO <sub>2</sub> +N <sub>2</sub>	0.0302	95.1	0.0035	11.0
	CO <sub>2</sub>	0.0006	1.9	0.0003	0.9
Chloroform Extracted	CO <sub>2</sub> +N <sub>2</sub>	0.0329	103.6	0.0030	9.5
	CO <sub>2</sub>	0.0007	2.2	0.0003	0.9

The ultra-micropore volume (CO<sub>2</sub>-adsorption) contributes to an extent to the total storage capacity. The storage capacity of A1 from ultra-micropore to mesopore region (CO<sub>2</sub>-adsorption+ N<sub>2</sub>-adsorption) is at least three times more than literature-estimated value while B1 shows lesser storage capacity than the literature. The difference can stem from variations between samples and the formation described in the literature. Nevertheless, the importance of the nanopore region for CO<sub>2</sub> storage capacity is shown.

Table 2.12 shows the difference between cumulative pore volume before and after toluene extraction. The differential pore volume indicates the volume of pores exposed for CO<sub>2</sub> storage upon removal of bitumen. In natural system, the differential pore volume/storage capacity refers to the volume of CO<sub>2</sub> that can be trapped by organic matter after soluble organic matter reaches post mature state and evacuates the pores. The area (37500 km<sup>2</sup>) and thickness (100 m) is the literature reference volume estimated for formation in previous calculation shown in Table 2.11. For the volume representing a formation, the storage capacities determined (13.2 Gt for A1 and 1.2 Gt for B1) show potential for large scale storage in kerogen-hosted pores.

Table 2.12: The additional storage capacity of CO<sub>2</sub> after bitumen removal.

(CO <sub>2</sub> +N <sub>2</sub> )-Derived Cumulative Pore Volume (cm <sup>3</sup> /g)					
Area	Thickness	Differential Pore volume (cm <sup>3</sup> /g)		Differential Storage Capacity	
		A1	B1	A1	B1
1 Acre	1 ft	0.0042	0.0004	8.70 Tonnes/acre ft	0.83 Tonnes/acre ft
10 km <sup>2</sup>	100 m	0.0042	0.0004	7.06 Mt/km <sup>3</sup>	0.67 Mt/km <sup>3</sup>
37500 km <sup>2</sup>	100 m	0.0042	0.0004	13.2 Gt	1.2 Gt

## CHAPTER 3

### SURFACE FREE ENERGY

This chapter aims to use contact angle measurements to theoretically determine the surface free energy, which in turn informs about the potential wettability of geological samples. The chapter is separated into five sections. (1) Terminology defines the terms and concepts used; (2) Background and motivation for determining surface free energy of rocks are explained. (3) Contact angle measurement method, the experimental steps and factors needed to be accounted for accurate representation of contact angle are discussed. (4) Contact angle measurement values are presented and analyzed; (5) Various inversion models are discussed to invert surface free energy from contact angle values.

### **3.1 Terminology**

#### **3.1.1 Wettability**

Wettability is a result of physical and chemical interaction between pore fluids and the rock. Common fluids are brine solutions, hydrocarbon components in both oil and gas form and carbon dioxide in the case of Carbon Capture, Utilization and Storage (CCUS). Wettability of cores affects electrical properties, capillary pressure, relative permeability, dispersion, primary, secondary and tertiary recovery, irreducible water saturation, and residual oil saturation (Anderson 1986). The extent of importance of wettability necessitate continuous efforts in determining this parameter. In this chapter, wettability is explored as parameter to explain rock-fluid interaction. Commonly, wettability in Earth Science can be illustrated as water-wet, oil-wet or intermediate

wet. In this work, I attempt to determine intrinsic wettability by determining the surface forces at play, particularly the surface free energy of solid/rock surfaces.

### **3.1.2 Surface Free Energy**

Surface energy, surface free energy, surface tension and interfacial tension are interconnected, but serve different meanings. Interfacial tension (ITF) is the property between any two substances. In this chapter, I focus on property of solid surfaces. Surface tension is a tangential stress in a surface layer and is related to surface free energy. For pure fluids, surface tension equals surface free energy (Shuttleworth 1950). Thus, surface tension is typically used to describe liquids. Surface free energy is defined as energy required to create unit area of new surface. There is an inward cohesive force on the surface of solid to minimize the energy on the surface. This minimization of energy governs the equilibrium contact of a liquid spread on the solid surface and consequently, the energy that creates a unit area of surface (Johnson et al. 1971). Surface energy and surface free energy are numerically different terms (Ip and Toguri 1994). Therefore, in order to accurately denote the information presented in this chapter, I will consistently use surface free energy for solids and surface tension for liquids.

Surface free energy governs interactions on the solid surface. High surface free energy indicates strong interactions on the surface. In this work, surface free energy is further divided into several components, such as van der Waals, Lewis acid-base, polar and non-polar components. The purpose of separating surface free energy into different intermolecular forces is to understand the contribution of each types of forces to possible interaction at surface. Relevance of each intermolecular force in rock-fluid interaction is shown:

van der Waals: van der Waals consists of dipole-dipole interaction (Keesom), induced dipole-dipole interaction (Debye) and fluctuating dipole-induced dipole London dispersion (Erbil 2006). These are forces introduced by van der Waals to manifest physical attraction and repulsion mechanisms for non-ideal gases and liquids. The London dispersion force is considered universal due to its lack of permanent dipoles. It is the only force with significant effect in macroscopic bodies (van Oss et al. 1988).

Lewis acid-base: Lewis acid is denoted by the electron acceptor ( $\gamma^+$ ) and Lewis base is denoted by electron donor ( $\gamma^-$ ). The Lewis acid and Lewis base components on rock minerals and crude oil are attracted to each other at the rock-oil interface. For example, the siloxane oxygen of phyllosilicates (clay minerals), illite on the mineral surface and sulfur from asphaltene are Lewis base, whereas nitrogen from crude oil and unsaturated silica on the mineral surface are Lewis acid (Mercier et al. 1999).

Polar and non-polar: The polar component of molecules come from the electronegativity of the atoms and the lack of molecular symmetry (Erbil 2006). For instance, CO<sub>2</sub> molecule is non-polar due to its symmetry between individual bond dipoles at both ends, yet it is able to interact with other molecules through ionic charge or its secondary dipole (Erbil 2006). Brine, on the other hand, is a highly polar component that reacts with other polar components.

Hydrophilic and hydrophobic interactions: Hydrocarbon molecules from crude oil and organic matter are incapable of forming H-bonds and therefore do not interact with water. Hence, they are called hydrophobic molecules (Erbil 2006). Contact angle of water on solid surfaces is shown to increase for samples with increasing total organic content, due to hydrophobicity of organic matter

(Aspenes et al. 2010). Hydrophilic minerals such as clay minerals have high H-bonding capacity and interacts with brine in subsurface.

### 3.1.3 Contact Angle

Young's equation (Young 1805), integral to studies of wettability, shows the balance of forces on solid and fluid interface as shown by Equation 3.1 and Figure 3.1.

$$\gamma_{lv}\cos\theta = \gamma_{sv} - \gamma_{sl} \quad (3.1)$$

Where:

$\gamma_{lv}$  = Interfacial tension between liquid and vapor  
 $\gamma_{sv}$  = Interfacial tension between solid and vapor  
 $\gamma_{sl}$  = Interfacial tension between solid and liquid  
 $\theta$  = Contact angle

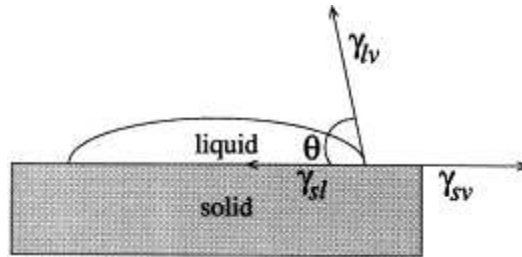


Figure 3.1: Contact angle of a liquid drop on solid surface (Kwok and Neumann 1999).

## 3.2 Background and Motivation

Typically, wettability of rock surfaces is directly measured using contact angle of water droplet or oil droplet (Figure 3.2). For example, a solid is defined as water wet if the water droplet's angle is lower than 90°C and oil-wet if water droplet's angle is greater than 120°C. For angle between 90°C and 120°C, the solid is known as intermediate wet, with no tendency for oil or water wettability (Zerpa et al. 2010). Defining rock by oil and water wettability has proven useful when

dealing with brine and hydrocarbons in the subsurface. However, due to the increasing interest of flowing CO<sub>2</sub> and different types of surfactants into the subsurface, it is important to define wettability of rock surfaces at a fundamental level. This work attempts to estimate solid surface free energy from contact angles, using Young's equation as the integral relation. The surface free energy is further divided into several components such as van der Waals, Lewis acid-base, polar and non-polar components. Dividing surface free energy into separate components allows us to study the contribution by several forces. The fundamental understanding of surface free energy on rock surfaces allows us to predict preferential/selective wettability of rock with any fluids, given the surface tension of the fluids are known.

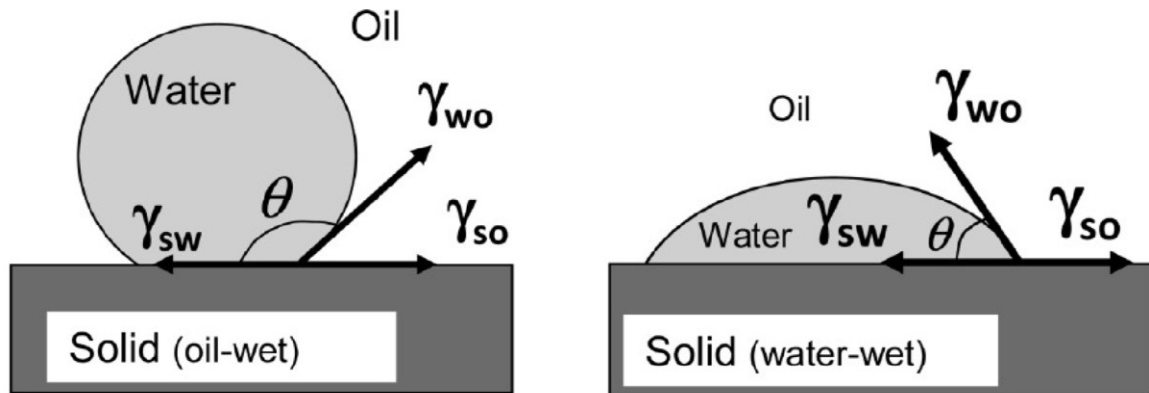


Figure 3.2: The balance of forces between rock, oil and water (Zerpa et al. 2010). Water droplet with large contact angle ( $>120^\circ$ ) is denoted as oil-wet (Diagram on the left). Water droplet with small contact angle ( $<90^\circ$ ) is denoted as water-wet (Diagram on the right).

While contact angle has been vastly applied to geological samples (Anderson 1986; Hirasaki 1991; Kovscek et al. 1993; Kwok and Neumann 1999; Aspenes et al. 2010; Zerpa et al. 2010; Aman et al. 2013; Teklu et al. 2015), very few studies have combined contact angle to determine surface free energy for rocks (Zelenev 2011; Zelenev and Lett 2013; Zelenev and

Grenoble 2018). Using previous literature as reference, this chapter illustrates the possibility of using contact angle measurements to determine surface free energy.

### 3.3 Contact Angle Measurement Method

Unlike liquids, solid surfaces are unable to conform to equilibrium conditions resulting from the minimization of surface free energy (Erbil 2006). Because surface free energy calculation is based on equilibrium conditions, the energy on a solid surface needs to be determined from probe liquids. The common parameter connecting liquid to solid is contact angle. Low contact angles indicate high attraction between the solid and the liquid; with a near zero contact angle for liquid with surface tension close to the surface free energy of the solid surface (Zisman 1964). I measured contact angles using a Drop Shape Analyzer (DSA100) from Krüss as shown in Figure 3.3.

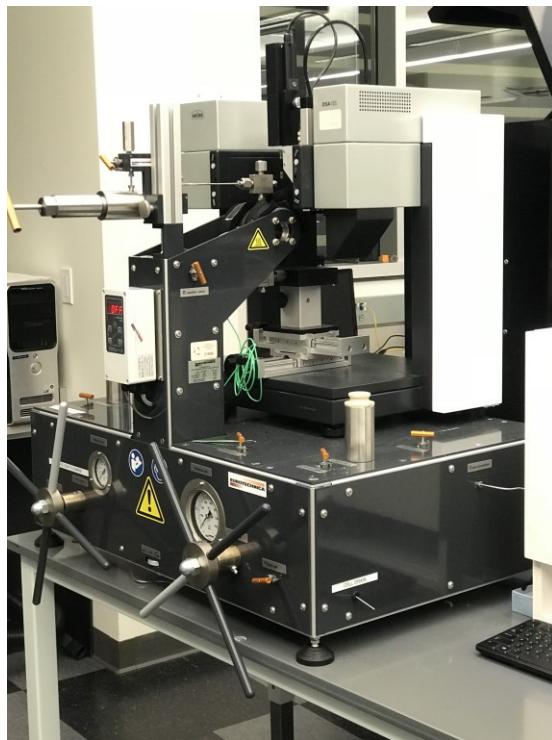
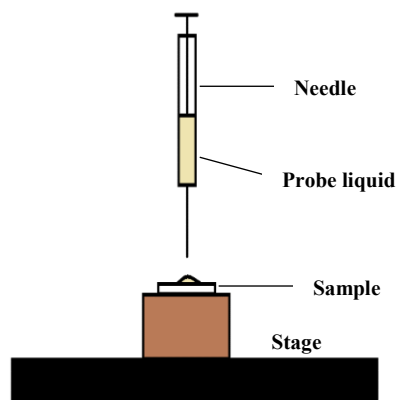


Figure 3.3: Drop Shape Analyzer (DSA100) used to measure the contact angle.

We used the sessile drop method where the contact angle of a free-standing liquid droplet is measured after a designated equilibrium time (refer to Figure 3.4). It is relatively simple for the purpose of using a variety of liquids and samples. Using any other method such as pendant drop requires using a large amount of the chemicals.



(a)



(b)

Figure 3.4: Sessile Drop Method: (a) Droplet suspension on a fused silica; (b) The schematic of sessile drop method.

Prior to the experiment, samples were placed in an enclosed box along with a beaker full of deionized water overnight, to ensure exposure to constant environment for all samples. During the measurement, the sample is mounted with a flat surface on a wooden block. I used the automated program described below from DSA100 manual for liquid droplet suspension to ensure reproducibility.

1. Start with syringe at standby position.
2. Move syringe to dosing position.
3. Dose 5.0  $\mu\text{L}$  of the liquid at 50  $\mu\text{L}/\text{s}$ . (It is dosed at the edge to prevent image reflection).

4. Move syringe back to deposition position after dosing slowly to prevent uncontrolled drops.
  5. Make images of the droplet using a high-speed camera for 60 seconds at 10 frames per second.
  6. Measure contact angle using an ellipse (Tangent-1) fitting for all droplets to be consistent.
- Consistency in terms of the (i) droplet size, (ii) equilibrium time, (iii) fluid choice, and (iv) sample preparation is important to obtain comparable contact angles.

### **3.3.1 Droplet Size**

The droplet size used is very small ( $= 5 \mu\text{L}$ ) to be close to the roughness scale on the sample (Zelenev 2011). Aman et al. (2013) shows the roughness scale for raw calcite and quartz crystals to be  $0.7\mu\text{m}$  and  $9.0 \mu\text{m}$  respectively. Some sources also recommend using a larger size of droplet ( $20\text{-}30 \mu\text{L}$ ) to capture the complete heterogeneity of samples (Drelich 2013). The grain sizes in shale are in the scale of nano- to micrometers (Loucks et al. 2009), and heterogeneity in shales can vary from grain to grain. Therefore, the droplet size chosen for this work ( $= 5 \mu\text{L}$ ) captures both the heterogeneity and roughness scale. The probe liquids used do not pose heterogeneity as only ultrapure liquids are used for the measurements (Table 3.1).

### **3.3.2 Equilibrium Time**

Equilibrium time is the time beyond which the droplet is assumed to reach equilibrium between rock surface and fluid surface forces. Equilibrium time is used to record the final contact angle for each run. For a liquid with high affinity towards rock surface, such as water to clay minerals, fluid tends to imbibe at very high rate. This has caused the clay pellet to swell in the water and dissociate completely as more water droplets are suspended on the surface. The contact angle at  $t=0$  second may seem reasonable because it is the initial angle. However, some liquids take time to equilibrate depending on room conditions and liquid purity. Therefore, sufficient time

needs to be given to the sample for equilibration without allowing the fluid to imbibe or evaporate in dry Colorado weather. Evaporation causes the liquid front to retreat and the contact angle value to decrease (Erbil 2006). The equilibrium time is set to 60 seconds, following Zelenev (2011).

### 3.3.3 Fluid Choice

Choice of fluid depends on potential surface interactions with the sample surface, surface reactivity and solubility (Rulison 1999). Using multiple liquids with a large range of surface energy values allows for a more accurate representation of the contact angle of the rock (Table 3.1). The probe liquid should be pure, homogenous and inert to avoid preferential adsorption to the surface (Hefer et al. 2006). For initial test cases, water (with equal acid and base component), diiodomethane (purely dispersive) and glycerol were used. However, glycerol was replaced by ethylene glycol and 1-Bromonaphthalene for later tests due to its high viscosity and incompatibility with DSA100. Prepared clay samples were not used in this work due to their reactivity to water droplets.

Table 3.1: The surface tension components of probe liquids (van Oss 1993). The probe liquids are arranged in terms of decreasing polarity. Glycerol and ethylene glycol are highly basic liquids. Water has neutral basic and acid components. Diiodomethane and 1-Bromonaphthalene are non-polar liquids.

Liquids	Purity	Lifshitz van der Waals, $\gamma_L^{LW}$ (mN/m)	Acid Component, $\gamma_L^+$ (mN/m)	Basic Component, $\gamma_L^-$ (mN/m)	Lewis Acid Base, $\gamma_L^{AB}$ (mN/m)	Total Surface Tension $\gamma_L^T$ (mN/m)
Glycerol	≥99/5%	34.0	3.9	57.4	30.0	64.0
Ethylene Glycol	99/8%	29.0	1.9	47.0	19.0	48.0
Water	Ultrapure (LC/MS grade)	21.8	25.5	25.5	51.0	72.8
Diiodomethane	99%	50.8	0.0	0.0	0.0	50.8
1-Bromonaphthalene	≥95%	44.4	0.0	0.0	0.0	44.4

### 3.3.4 Sample Preparation

The samples used are: (a) calcite and quartz crystals as standard minerals of geological samples, (b) quartz microscope slides (25.4mmx25.4mmx1mm) obtained from Polysciences, Inc, (c) fused silica from Edmund Optics, (d) clay pellets made of illite-smectite mixed layer and illite-cambrianshale, and (e) shale samples from Niobrara formation. The ISCz and IMt-2 clay minerals' powder is pressed into pellet with a pressure of 25000 psi. These freshly made pellets were stored away from atmosphere in sealed sample bags. Some challenges associated with sample preparation are: (i) surface contamination and (ii) surface flatness, (iii) surface roughness.

#### (i) Effect of surface contamination

The probed surface needs to be pure and clean of any contamination. Typically, cores are cleaned from hydrocarbon by Soxhlet extractor with sequential extraction by toluene and methanol, and oven-dried for 24 hours (Teklu et al. 2015). Such method should be used for measuring contact angles for aged (sample saturated in brine or crude oil) samples. For this work, I first measured contact angle for preserved samples. In order to compare the efficiency of cleaning, some calcite and quartz crystals obtained from gem shops were scrubbed and wiped with deionized water and surfactant. The crystals were dried in vacuum oven at 200°C for 2 hours. Both cleaned and uncleaned samples were covered in epoxy until only the flat surface is visible. Quartz microscope slides and fused silica were tested as they were received.

Table 3.2 compares the standard deviation of measured contact angles for cleaned and uncleaned crystals. The standard deviation obtained for contact angles on quartz has decreased after surfactant cleaning. However, this does not apply for calcite. The standard deviation of cleaned calcite increased for glycerol and diiodomethane liquids. The inconsistency is possibly due to potential reaction of calcite minerals with the surfactant.

Table 3.2: Contact angles measured on cleaned and uncleaned quartz and calcite crystals.

Mineral		Water	Mean	STD	Glycerol	Mean	STD	Diiodomethane	Mean	STD
Quartz	Uncleaned	38.7			51.0			47.8		
		41.9	42.9	4.8	63.5	59.9	7.8	54.7	53.8	5.7
		48.2			65.3			59.1		
	Cleaned	26.6			46.3			49.1		
		29.5	27.3	2.0	47.9	48.6	2.7	49.6	48.3	1.9
		25.8			51.6			46.1		
Calcite	Uncleaned	60.5			63.7			42.5		
		69.7	61.3	8.0	69.3	66.6	2.8	41.4	40.8	3.0
		53.8			66.8			36.9		
	Cleaned	39.0			67.1			48.6		
		50.1	44.6	5.5	70.6	66.1	5.0	41.1	43.4	4.6
		44.6			60.6			40.4		

(ii) Effect of surface flatness

The solid surface needs to be flat, and smooth for comparable contact angle measurements to avoid gravity effects on inclined surfaces that drag the liquid to one side. One way to determine the importance of flat samples for contact angle measurements is observed through studying the variance in measurements on fused silica optical flat with a flatness and smoothness value of  $20\lambda$  (Table 3.3). The standard deviation is relatively small compared to quartz and calcite crystals. Note that glycerol is substituted with ethylene glycol.

Table 3.3: Contact angle measurements on fused silica optical flat ( $20\lambda$ ).

	Water	Mean	STD	Ethylene Glycol	Mean	STD	Diiodomethane	Mean	STD
Fused Silica	14.69			29.0			43.1		
	16.77	14.5	2.0	28.8	29.6	0.9	41.4	43.1	1.7
	14.46			29.9			44.9		
	11.91			30.8					

(iii) Effect of surface roughness

The surface free energy can be lowered by roughness, as rough surface prevents complete contact with fluid (Aman et al. 2012). One way to smoothen the rough surface is by polishing with sandpaper of increasing fineness (100, 220, 400 grit) in a consistent motion (Zelenev 2011; Aman et al. 2012; Teklu et al. 2015). For rock samples that are cored and cut to size, sanding removes the top layer to provide a virgin surface for contact angle measurements. A cleaved crystal surface is naturally flat. Any sanding will destroy the natural surface of the crystals. Therefore, the standard samples used for this experiment (pure calcite and quartz crystals) were not polished with sandpaper.

### 3.3.5 Summary of Methods

Table 3.4 summarizes preparation methods and fluid choice for each sample.

Table 3.4: Summary of preparation method and fluid choice for each sample.

	Calcite crystal	Quartz crystal	Quartz slides	Fused Silica	Shale N1	Shale N2
Cleaned	✓	✓				
Polished					✓	✓
Water	✓	✓	✓	✓	✓	✓
Diiodomethane	✓	✓	✓	✓	✓	✓
Glycerol	✓	✓			✓	✓
Ethylene Glycol	✓		✓	✓		
1-Bromonaphthalene	✓		✓			

### 3.4 Results and Discussion

There is no single equilibrium contact angle on a surface due to surface heterogeneity, roughness, and chemical interactions/heterogeneity. Surface roughness increases the surface area and affects the contact angle (Erbil 2006). Compositional heterogeneity may cause asymmetrical contact angle because the hydrophobic area would hinder the liquid from further spreading while

the hydrophilic portion will attract the liquid to be more spread out on one side. In such cases, I take the average of the left and the right contact angles. Shale samples are heterogenous in terms of both chemistry and roughness (Table 3.5). The contact angles measured on the shales are comparable to the standard deviation determined for pure crystals (Table 3.6).

Table 3.5: Mineralogy of Niobrara shale obtained from XRD.

	Sample ID	TOC	Quartz	K-spar	Plagioclase	Pyrite	Calcite	Dolomite	Mixed Illite/Smectite	Illite
Niobrara 3193.05	N1	0.3	4.7	0.0	1.2	0.6	88.9	1.5	2.1	1.0
Niobrara 3101.9	N2	4.8	14.0	1.0	3.0	5.0	53.0	0.0	11.0	13.0

Table 3.6: Contact angles measured on heterogenous Niobrara shales.

Shales	Water	Mean	STD	Glycerol	Mean	STD	Diiodomethane	Mean	STD
N1	93.9	95.9	5.1	47.8	55.7	6.9	16.3	16.1	2.3
	90.3			59.6			13.7		
	96.9			59.8			18.3		
	102.4								
N2	93.0	95.5	3.1	68.3	71.6	3.9	42.2	43.2	1.8
	98.4			71.6			41.6		
	92.7			77.0			45.7		
	97.9			69.3			43.1		

Due to the heterogeneity posed by shales, three or four measurements are insufficient to provide representative average contact angle. Figure 3.5 and Figure 3.6 show the variation in contact angles as captured by the high-resolution camera for quartz and calcite. Therefore, multiple contact angle measurements were made on various locations on quartz microscope slides and calcite crystals to evaluate the number of measurements needed per surface. Twelve contact angle

measurements from several calcite and quartz microscope slides were obtained for each probe liquid; multiple measurements at the same location were grouped together. Twelve is a random number sufficient to gain contact angle measurements from at least three surfaces for most samples. Several crystals were used for better representation of the contact angle, and to avoid a bias towards any one crystal. The different groups are identified by the sample initials (Table 3.7 and Table 3.8).

A statistical approach using JMP analysis (a software program used for statistical analysis) is used to determine the representative angle. The analysis program allows comparison of means of several groups using F-ratio and the T-ratio tests. F-ratio is the ratio of intergroup variation to the intragroup variation, used to statistically compare group means. The t-test is comparison between means of two groups, f-ratio compares more than two groups.

First, the sample data are plotted for each group with their upper and lower 95% confidence limit. The 95% limit represents the range of two standard deviation from the mean. Any values that lie outside the 95% range are removed. These values are marked by grey boxes in Table 3.7 and Table 3.8. Then, analysis of variance is performed using t-test and f-ratio to statistically compare each pair of groups. If a group is determined to be statistically different, the entire group is removed from the contact angle analysis. Table 3.7 and Table 3.8 show shaded area for points falling outside of the 95% confidence limit within each group and for groups that are statistically different. Figure 3.7 and Figure 3.8 show whisker plots, visually comparing the different groups.

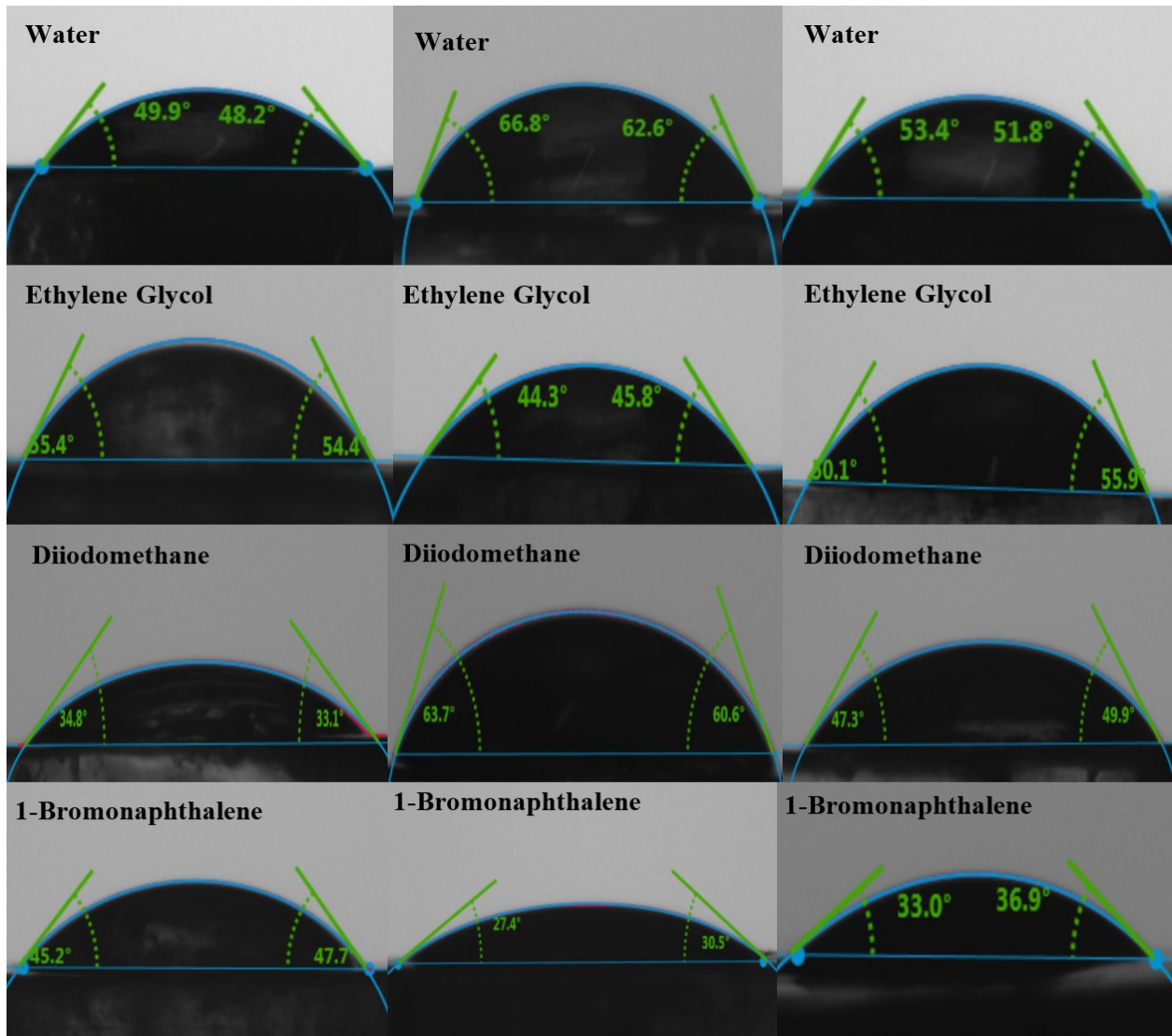


Figure 3.5: The variance in contact angles measured as captured by the high-resolution camera for calcite crystals.

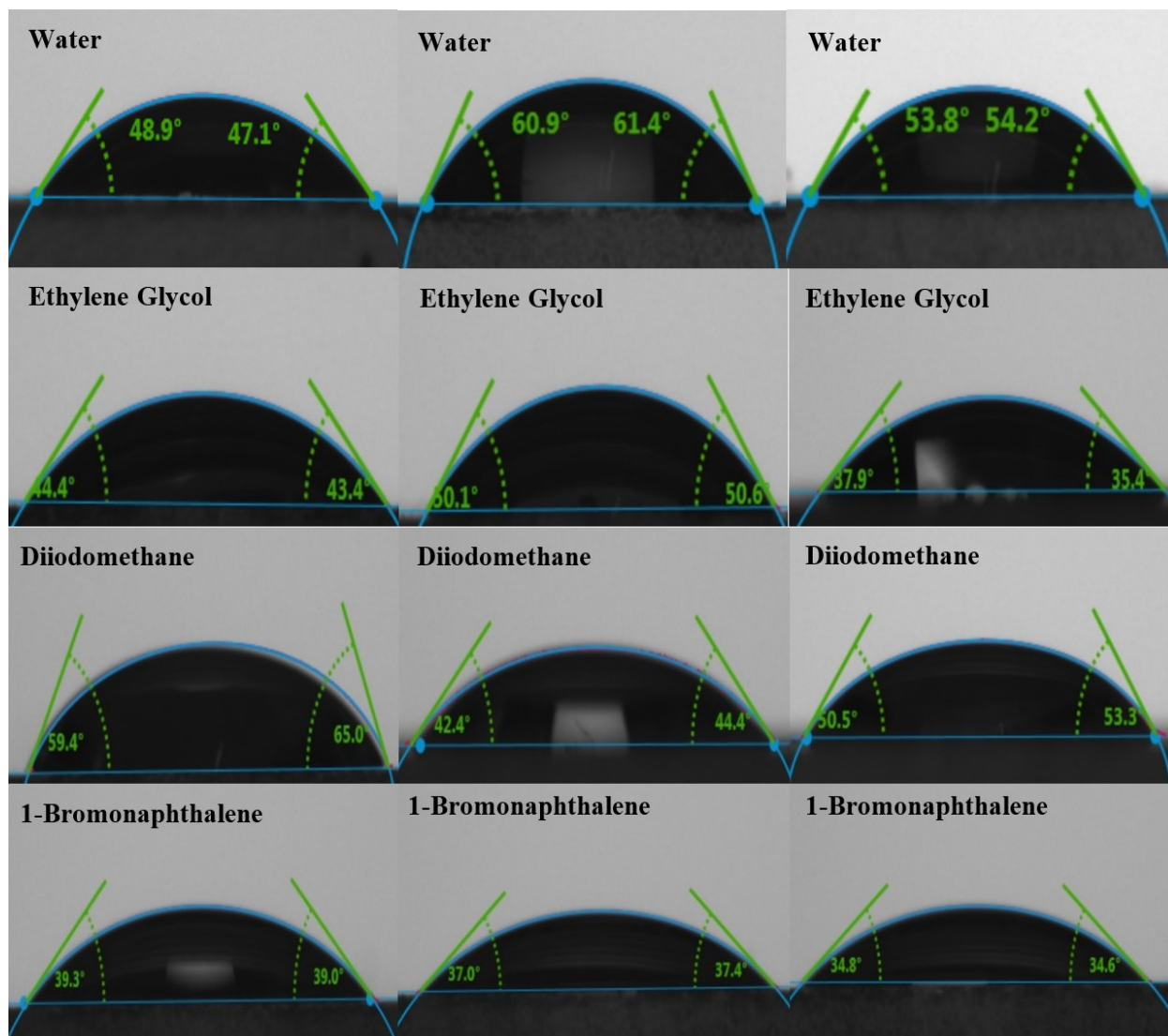


Figure 3.6: The variance in contact angles measured as captured by the high-resolution camera for quartz microscope slides.

Table 3.7: The contact angles on calcite crystals. The shaded cells contain values omitted. Different groups of samples are indicated by sample ID. The lines within each column shows groups of multiple measurements in the same locality.

Count	Water		Ethylene Glycol		Diiodomethane		1-Bromonaphthalene	
1	A1	56.8	B1	54	C1	52.5	D1	29.7
2	A1	60.6	B1	53	C1	62	D1	21.7
3	A1	63.5	B1	53.5	C2	49.7	D1	30.5
4	A1	49.3	B2	45.9	C2	52.2	D2	40.7
5	A2	53.7	B2	41.5	C2	48.5	D2	37.6
6	A2	53.8	B2	41.2	C2	34.8	D3	38.8
7	A2	51.7	B2	44.7	C3	55.9	D3	34.5
8	A2	60.5	B2	46.2	C3	62.8	D3	38.6
9	A3	47.9	B3	53.2	C3	62.4	D3	42.3
10	A3	56.1	B3	52.4	C4	60.9	D4	36.9
11	A3	51	B3	53.5	C4	56.2	D4	44
12	A3	53.9	B3	52	C4	46.3	D4	45.1

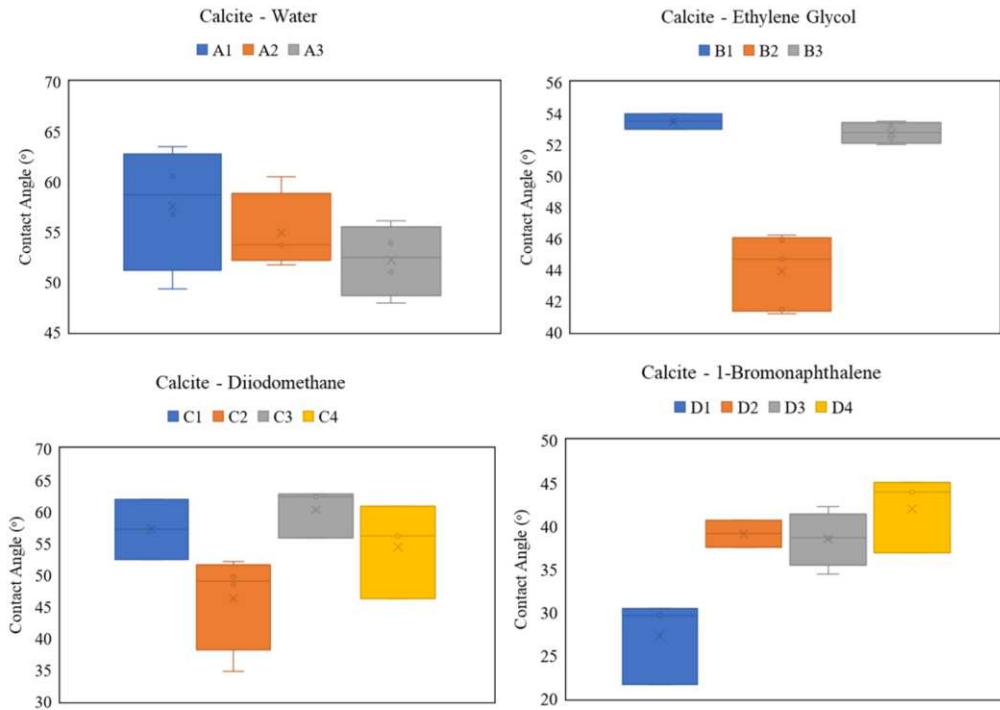


Figure 3.7: Whisker plot of calcite with each probe liquid: The plot compares the means of different groups shown in Table 3.7. The plot shows how groups B2 and D1 are different from the rest of the measurements for respective fluids. Group A1 is also removed due to its large variance within the group. Such variance is captured better by the JMP analysis method than discerning from whisker plot.

Table 3.8: The contact angles on quartz microscope slides. The shaded cells contain values omitted. Different groups of samples are indicated by sample ID. ND refers to No Data.

Count	Water		Ethylene Glycol		Diiodomethane		1-Bromonaphthalene	
1	A1	46.6	B1	47.8	C1	49.7	D1	37.3
2	A1	48.1	B1	43.2	C1	49.8	D1	39.2
3	A1	60.2	B1	40.0	C1	48.4	D1	38.3
4	A1	58.0	B1	42.9	C1	49.3	D1	38.1
5	A2	47.1	B1	44.8	C1	49.4	D2	37.8
6	A2	43.6	B1	42.3	C1	47.8	D2	36.7
7	A2	51.9	B2	38.1	C1	50.4	D2	37.7
8	A3	52.6	B2	39.6	C1	48.6	D2	36.9
9	A3	45.4	B2	48.8	C1	60.3	D3	35.0
10	A3	52.1	B2	50.3	C2	42.8	D3	38.3
11	A4	52.9	B2	44.7	C2	53.3	D3	35.2
12	A4	56.2	B2	36.7	C2	51.4	D3	37.6
13	ND	ND	ND	ND	C2	52.6	ND	ND
14	ND	ND	ND	ND	C2	52.2	ND	ND
15	ND	ND	ND	ND	C2	54.5	ND	ND

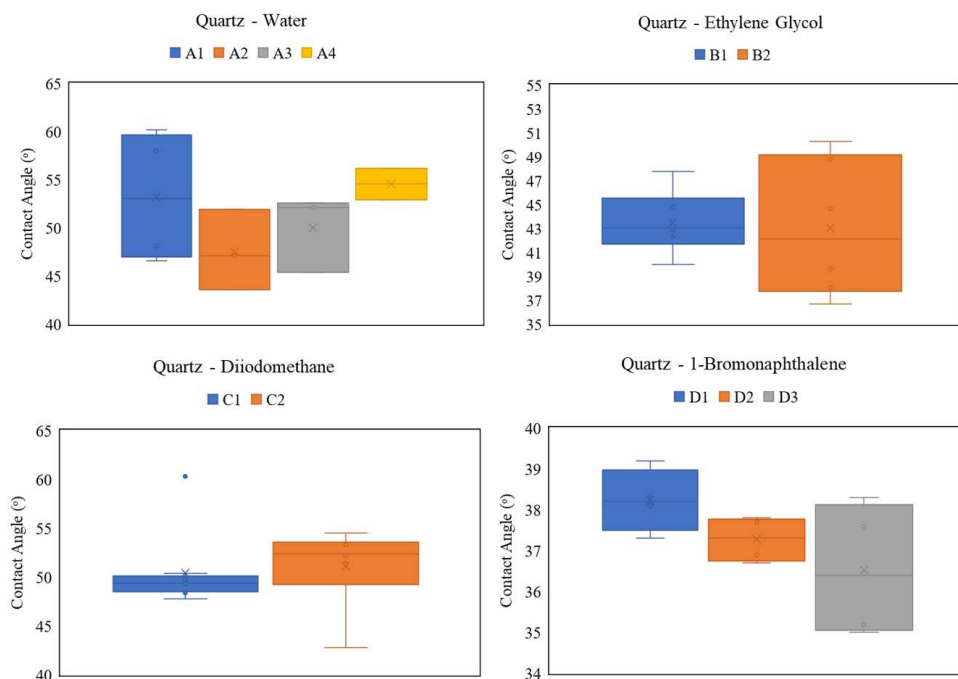


Figure 3.8: Whisker plot of quartz with each probe liquid: The plot compares the means of different groups shown in Table 3.8. As indicated by the JMP analysis method, the groups are not statistically different from each other for each probe liquid, largely due to homogeneity and flatness of quartz microscope slides. Some measurements from each group are removed to reduce the variance within the group.

Table 3.9 shows the means and standard deviation of contact angle for each probe liquid before and after the statistical analysis. The standard deviation has decreased in each case after removing contact angles that are statistically different from the rest of the measurements in the set.

Table 3.9: The means and standard deviation before and after the statistical analysis.

Sample	Probe Liquid	Before		After	
		Mean	STD	Mean	STD
Quartz	Water	51.2	5.2	50.1	4.0
	Ethylene Glycol	43.3	4.3	43.0	3.3
	Diiodomethane	50.7	3.7	50.6	2.1
	1-Bromonaphthalene	37.3	1.2	37.6	0.6
Calcite	Water	54.9	4.8	52.6	2.6
	Ethylene Glycol	47.5	5.3	40.1	0.7
	Diiodomethane	53.7	8.3	55.4	6.0
	1-Bromonaphthalene	36.7	6.7	40.8	3.1

From trying several methods, the recommended steps for contact angle measurements inverted for surface free energy are:

- (i) Do not use the same syringe and needle for different probe liquids. As contact angle measurement is highly surface sensitive, changing between liquids requires meticulous cleaning of the syringe.
- (ii) Wipe the sample surface with residue wipes (e.g. Kimwipes) to clean the dust after polishing.
- (iii) Make multiple measurements of contact angle for each probe liquid at multiple locations on the sample to capture or assess heterogeneity (Zelenev 2011).
- (iv) Conduct measurement in a covered cell (Drelich 2013) to avoid dust and moisture contamination.
- (v) Clean the tip of needle with parafilm to prevent the liquid from climbing up the needle.

- (vi) Record the time dependency of each probe liquid to equilibrate; use the same equilibrium time for all probe liquids for the measurements.
- (vii) Droplet size should be smaller than the roughness scale.
- (viii) Droplet size should be larger than the heterogeneity.

### **3.5 Inversion Models**

Surface free energy on the surface of solid is not as visible as it is on the surface of liquid (Erbil 2006). One way to calculate the solid surface free energy is by inverting from contact angle measurements of probe liquids on the solid surface using one of several theoretical models available: Zisman's method, Fowkes' method, Owens and Wendt's method, Wu's method, Neumann's method and van Oss-Chaudhury-Good method (Rulison 1999; Erbil 2006). These models are based on intermolecular forces that cause most properties of solid, liquid and gas phases, and their interactions with each other.

Of the models listed, Zisman's method requires the surface to be completely non-polar that it becomes insufficient for rock surfaces (Rulison 1999). Neumann's method has been invalidated due to erroneous thermodynamics (Erbil 2006). Fowkes, Owens and Wendt, and Wu's methods are also based on incorrect assumption that all polar materials interact with other polar materials (Erbil 2006). Van-Oss-Chaudhury-Good model, on the other hand, is found to show bias towards Lewis basic component (Mittal and Etzler 2008). Note that all the models have certain limitations. Two methods were chosen for the purpose of determining surface free energy of rock surfaces: (i) van-Oss-Chaudhury-Good model due to its inclusion of chemical interactions such as hydrogen bonding and acid-base interactions, and (ii) Owens and Wendt's theory (derived from Fowkes and theoretically similar to Wu's method) due to its ability to derive a more representative surface free

energy value by using a larger number of probe liquids as compared to van-Oss-Chaudhury-Good model.

The van Oss-Chaudhury-Good model consists of Lifshitz van der Waals and Lewis acid-base components. Lifshitz van der Waals component consists of London dispersion forces with minor influence from induced dipole-dipole (Debye) and dipole-dipole (Keesom) interactions (Erbil 2006). Lifshitz van der Waals is derived from van der Waals theory for macroscopic bodies accounting for temporal fluctuations in the field between neighboring molecules (van Oss et al. 1988). Owens and Wendt model consists of polar and dispersive components, where the polar component consists of induced dipole-dipole interaction, dipole-dipole interaction and hydrogen bonding and the dispersive component is solely based on van der Waals London dispersion forces.

### 3.5.1 van Oss-Chaudhury-Good Method

The total surface free energy consists of Lifshitz van der Waals and Lewis acid-base components.

$$\gamma_i = \gamma_i^{LW} + \gamma_i^{AB} \quad (3.2)$$

Where:

$\gamma_i^{LW}$  = surface tension contributed by Lifshitz van der Waals component (LW)

$\gamma_i^{AB}$  = surface tension contributed by Lewis acid-base component (AB)

i = solid (s), liquid (L), or solid-liquid (SL)

Note that surface tension terms can also be represented in terms of Gibbs free energy:

$$\Delta G_i = \Delta G_i^{LW} + \Delta G_i^{AB} \quad (3.3)$$

Where:

$$\Delta G_i = -2\gamma_i \quad (3.4)$$

The Lifshitz van der Waals surface tension between solid and liquid is expressed as (Fowkes 1963):

$$\Delta G_{SL}^{LW} = -2\sqrt{\gamma_S^{LW}\gamma_L^{LW}} \quad (3.5)$$

The Acid-Base surface tension is shown as (van Oss et al. 1986):

$$\Delta G_{SL}^{AB} = -2\sqrt{\gamma_S^+\gamma_L^-} - 2\sqrt{\gamma_S^-\gamma_L^+} \quad (3.6)$$

Substituting into Equations 3.5 and 3.6 into 3.3, the total surface tension contributed by Lifshitz van der Waals and Acid-Base components is shown as (van Oss et al. 1988):

$$\Delta G_{SL} = -2\sqrt{\gamma_S^{LW}\gamma_L^{LW}} - 2\sqrt{\gamma_S^+\gamma_L^-} - 2\sqrt{\gamma_S^-\gamma_L^+} \quad (3.7)$$

The changes of free energy due to interaction between the solid and liquid phase can also be shown by Young-Dupre equation (Erbil 2006):

$$-\Delta G_{SL} = \gamma_{SL} - \gamma_S - \gamma_L \quad (3.8)$$

Combining Equations 3.1 and 3.8 gives:

$$-\Delta G_{SL} = \gamma_L(1 + \cos\theta) \quad (3.9)$$

Combining Equations 3.7 and 3.9 gives the van Oss-Chaudhury-Good equation:

$$\gamma_L(1 + \cos\theta) = 2\sqrt{\gamma_S^{LW}\gamma_L^{LW}} + 2\sqrt{\gamma_S^+\gamma_L^-} + 2\sqrt{\gamma_S^-\gamma_L^+} \quad (3.10)$$

In measuring the contact angles, we know the surface tensions of the probe liquids (Table 1). The unknowns from the above equation are  $\gamma_S^{LW}$ ,  $\gamma_S^+$  and  $\gamma_S^-$ . Simplifying Equation 3.10 for purely dispersive diiodomethane determines the  $\gamma_S^{LW}$ .

$$\gamma_S^{LW} = \frac{[\gamma_L(\cos\theta+1)]^2}{4\gamma_L^{LW}} \quad (3.11)$$

Using the mean contact angles determined for two more liquids, the solid acid and base components can be determined using van Oss-Chaudhury-Good equation. The Lifshitz van der Waals and Lewis acid-base components for standard materials such as quartz, calcite and fused silica are shown in Table 3.10.

### 3.5.2 Owens and Wendt's Method

Owens and Wendt (1969) shows that surface free energy of solid in contact with liquid consists of two components: the dispersive component for non-site-specific interactions and polar component for site-specific interactions. This method is derived from and is mathematically similar to the Fowkes' theory. It is further developed into the Owens-Wendt-Raebel-Kaelble (OWRK) method (Erbil 2006). Although these methods are interchangeably addressed in several literature sources, this chapter presents the Owens and Wendt's method as illustrated by Rulison (1999). The Owens and Wendt equation is derived from Young's equation (Equation 3.1) and Good's equation. Good and Girifalco (1960) shows:

$$\gamma_{SL} = \gamma_S + \gamma_L - 2\sqrt{\gamma_L^D \gamma_S^D} - 2\sqrt{\gamma_L^P \gamma_S^P} \quad (3.12)$$

Where:

$\gamma_L^D$  = Dispersion component of liquid

$\gamma_S^D$  = Dispersion component of solid

$\gamma_L^P$  = Polar component of liquid

$\gamma_S^P$  = Polar component of solid

The Owens and Wendt equation can be rearranged to a linear relationship such as  $y=mx+c$  and analyzed using regression analysis:

$$\frac{\gamma_L(\cos \theta + 1)}{2\sqrt{\gamma_L^D}} = \sqrt{\gamma_S^P} \frac{\sqrt{\gamma_L^P}}{\sqrt{\gamma_L^D}} + \sqrt{\gamma_S^D} \quad (3.13)$$

Where:

$$y = \frac{\gamma_L(\cos \theta + 1)}{2\sqrt{\gamma_L^D}}$$

$$m = \sqrt{\gamma_S^P}$$

$$x = \frac{\sqrt{\gamma_L^P}}{\sqrt{\gamma_L^D}}$$

$$c = \sqrt{\gamma_S^D}$$

The dispersion ( $\gamma_S^D$ ) and polar components ( $\gamma_S^P$ ) of the solid are determined from the gradient and the y-intercept of a linear plot as shown in Figure 3.9. The polar and dispersive component of surface free energy for quartz and calcite is shown in Table 3.11.

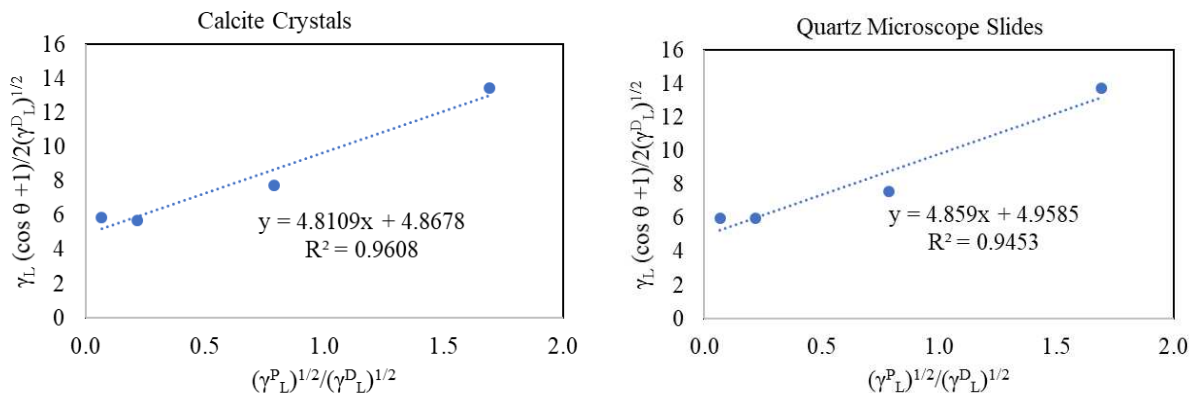


Figure 3.9: The Owens and Wendt's plot with four probe liquids. The polar and dispersive components of the solids are derived from the linear plot.

### 3.5.3 Results and Discussion

For both models, two major mineral constituents of shales, quartz and calcite, are studied separately to understand their individual contributions to the total surface free energy of shales and to compare with literature. The measured surface free energy values are compared with literature for validation. Using van Oss-Chaudhury-Good model shown in Table 3.10, the values obtained for cleaned calcite is validated with findings from Chibowski and Pera- Carpio (2002). The difference in Lewis base of cleaned versus uncleaned calcite crystal is likely due to the surfactant wiping method. On the other hand, the surface energy determined for quartz mineral does not match any previous literature. The Lifshitz van der Waals energy of quartz is comparable to Janczuk and Zdziennicka (1994), but the Lewis base is higher by 40 mN/m. Fused silica's surface energy is comparable to glass slides as determined by both Chibowski and Pera- Carpio (2002) and Zelenev (2011). Fused silica can be complementing better with literature values due to its homogenous and amorphous surface.

Table 3.10: The surface energy components as determined from the van Oss-Chaudhury-Good equation.

Solid	Lifshitz van der Waals, $\gamma_L^{LW}$ (mN/m)	Basic Component, $\gamma_L^-$ (mN/m)	Acid Component, $\gamma_L^+$ (mN/m)
Quartz (Uncleaned)	32.1	50.9	0.0
Quartz (Cleaned)	35.2 (36.08*)	59.1 (11.86*)	0.2 (9.40*)
Calcite (Uncleaned)	39.2	26.4	0.1
Calcite (Cleaned)	37.9 (40.2**)	54.5 (54.4**)	0.5 (1.3**)
Fused Silica	38.0 (33.7**, 28.43***)	72.3 (62.2**, 51.51***)	0.0 (1.3**, 0.74***)

\*Janczuk and Zdziennicka (1994)  
\*\*Chibowski and Pera-Carpio (2002)  
\*\*\*Zelenev (2011)

According to Owens and Wendt's model in Table 3.11, the polar and dispersive components contribute equally to the total surface free energy of calcite and quartz minerals. The surface energy value determined for quartz is close to findings of Janczuk and Zdziennicka (1994). Although the total surface energy of calcite ( $\approx 46$  mN/m) is similar to Zelenev and Lett (2013), the individual polar and dispersive component contributions differ.

Table 3.11: The polar and dispersive component of calcite and quartz minerals determined using the Owens and Wendt's linear plot.

Pure Minerals	Calcite	Polar	mN/m	23.14	(8.6 $\pm$ 0.4*)
		Dispersion	mN/m	23.70	(41.5 $\pm$ 0.7*)
	Quartz	Polar	mN/m	23.61	(36-37**)
		Dispersion	mN/m	24.59	(20-22**)

\*Zelenev and Lett (2013)  
\*\*Janczuk and Zdziennicka (1994)

Interestingly, the Lewis base component for all the mineral constituents determined from van-Oss-Chaudhury-Good model are large, whereas the Lewis acid is almost negligible. Morra (1996) has pointed out that in contrast to chemical intuition, the model shows predominantly Lewis

base parameter for most materials because the acid components of the probe liquids are less than 10 mN/m (except water), whereas the range for basic component of the probe liquids is 0-77 mN/m (Mittal and Etzler 2008). Owens and Wendt's model addresses the bias of the van-Oss-Chaudhury-Good model by using liquids with a larger range of surface tension. Additionally, the surface free energy of shales is poorly understood. Surface free energy of Niobrara (N1 & N2), determined from van-Oss-Chaudhury-Good model, is compared with other North American shale samples from the Marcellus, Rhinestreet, Dunkirk and Horn River formations (Zelenev 2011).

Table 3.12: Surface free energy of Niobrara compared with literature from Zelenev (2011).

Solid	Lifshitz van der Waals, $\gamma_L^{LW}$ (mN/m)	Basic Component, $\gamma_L^-$ (mN/m)	Acid Component, $\gamma_L^+$ (mN/m)
N1 Shale	48.8	2.7	2.7
N2 Shale	38.0	0.0	0.7
Zelenev (2011)			
Marcellus	47.17	6.98	0.24
Rhinestreet	42.94	8.36	0.33
Dunkirk	46.22	6.77	0.51
Horn River	43.22	8.45	0.17

According to Table 3.12, Lifshitz van der Waals component is comparable, close to 40 mN/m and the Lewis acid components are also similarly very low. The Lewis base determined by Zelenev (2011) is consistently higher than the values determined for Niobrara shale.

Conclusion: Individual calcite and quartz were studied to investigate if their surface free energy contributes to the total surface free energy of shales in an addition manner. I did not find any evidence for such relationship between individual minerals and composite shale. From Table 3.12, the main intermolecular force on the surface of shales is the Lifshitz van der Waals because it is a universal force that applies to both polar and non-polar components. Similar to findings in

this study, Zelenev (2011) also shows that Lifshitz van der Waals primarily contributes to surface free energy of shales. I therefore hypothesize that such observation likely applies to all shales.

## CHAPTER 4

### CHEMICAL CHARACTERIZATION OF RESERVOIR AND CAP-ROCKS

This chapter is in preparation for submission to a journal.

This chapter discusses the current state and future directions for chemical characterization of reservoir and cap-rocks with the goals of linking chemical composition to wettability of rocks and understanding fundamental interactions of rocks with relevant gas molecules. The chapter consists of six sections. (1) Introduction provides the motivation for studying chemical composition to understand wettability, and introduces various techniques used to characterize shales such as X-ray Diffraction (XRD), Thermogravimetric Analysis (TGA), Electron Microscopy, Energy Dispersive X-ray Spectroscopy (EDS) and X-ray Photoelectron Spectroscopy (XPS); (2) XRD to assess the bulk mineralogy of rocks; (3) TGA to provide supporting data for mineral characterization and indicates presence of adsorbed species; (4) Electron microscopy and EDS to characterize heterogeneities and elemental composition of reservoir rocks using Environmental SEM. With this information, I provide a workflow where XRD, TGA, ESEM and EDS feeds information for further studies with XPS. (5) Finally, I describe the potential of XPS to evaluate chemical composition to determine wettability; and (6) near-ambient pressure XPS (AP-XPS) to study interactions with gas molecules.

#### **4.1 Introduction**

In this chapter, I discuss chemical characterization for (i) predicting wettability, and (ii) assessing rock interactions with relevant gas molecules. The two concepts are interconnected. As described in Chapter 1 (Introduction), wettability affects various properties of rocks, such as

electrical properties, capillary pressure, relative permeability, dispersion, irreducible water saturation and residual oil saturation (Anderson 1986). Abovementioned properties govern rock-fluid interactions that control effectiveness of oil recovery processes such as waterflooding, CO<sub>2</sub> flooding and chemical flooding. The motivation of this chapter is to investigate composition of rocks and effect of composition on interactions with relevant gas molecules, with and without presence of water and methane.

Reservoir rocks, especially shales, are heterogenous in their elemental composition. The elements commonly observed in rocks are oxygen, carbon, silicon, nitrogen, aluminum, potassium, magnesium, calcium and iron. I used various complementary techniques for comprehensive characterization of the samples: X-ray Diffraction (XRD), Thermogravimetric Analysis (TGA), Environmental Scanning Electron Microscope (ESEM), Energy Dispersive X-ray Spectroscopy (EDS) and X-ray Photoelectron Spectroscopy (XPS). XRD allows the initial determination of bulk minerals in the sample. TGA is a complementary method to XRD and further indicates presence of adsorbed molecules on the pore surfaces. With initial identification of bulk mineralogy, I used ESEM and EDS to determine fine-scale elemental composition to evaluate heterogeneity of the samples. I demonstrated capabilities and limitations of ESEM/EDS for analysis of lighter component such as carbon, among the mix of both lighter and heavier elements. Identification of the amount and distribution of light element such as carbon is important for rock studies as carbon content is widely used in past literature to determine oil wettability; oil wettability is caused by organic carbon. Due to XPS ability to determine amount of carbon and distinguish organic carbon from inorganic carbon (carbonate minerals) and adsorbed air-borne carbon, XPS has been widely used to study wettability of rocks. Thus, sensitivity of XPS is utilized for fine-scale (elemental) wettability determination.

Additionally, recent developments in XPS instrumentation enabled capabilities for near-ambient pressure XPS (AP-XPS), which allows to investigate in-situ reactions at rock-fluid interface in the presence of gases and moisture. Of particular interest are studies of rock samples with the following gases: water vapor, methane and carbon dioxide. Rocks in the formation have irreducible water saturation (moisture) that naturally covers the pores to an extent and some trapped methane. For the application of CO<sub>2</sub> utilization and storage in formations, in-situ CO<sub>2</sub> reaction with rock minerals, with and without the presence of water and methane is therefore of interest. Permanent trapping of CO<sub>2</sub> in the minerals of formation is possible through a phenomenon known as mineral carbonation, where divalent cations of some minerals react with CO<sub>2</sub> to form solid carbonates. While theoretical and experimental explanations exist for this mechanism, XPS can provide fundamental information at the rock-CO<sub>2</sub> interface.

Sections below present a workflow proposed for future comprehensive investigation of rocks with different chemistry, along with reference samples (Agardhfjellet and Niobrara shales). Some sections include analysis of literature and preliminary experiments while others provide discussion of literature identifying directions for future experimental studies.

## **4.2 X-ray Diffraction (XRD) Mineral Analysis**

Introduction: X-ray Diffraction (XRD) measures bulk mineralogy. Comprehensive chemical characterization of a surface requires accurate prediction of the elements present on the surface. For rock surfaces, elemental characterization is complicated by complex mineralogy, especially for shales. Shale is a fine-grained sedimentary rock with large sorption capacity and tight permeability that is of increasing interest as both source and reservoir rock. Therefore, identification of the minerals allows us to predict elements possibly present.

Principles of operation: XRD detects crystalline compounds based on specific crystal structure. Each mineral has a characteristic crystal structure. In XRD, X-rays are generated and focused on powdered sample. The diffracted X-rays are detected by a detector and recorded in a spectrum. The count is recorded in terms of diffraction angles, which later converts to distance between adjacent planes of atoms (d-spacing) (Panfiloff 2016). Minerals are identified from their unique set of d-spacing.

Results: The samples characterized in this section are calcite-rich N1 from Niobrara shale and organic-rich A1 caprock from Agardhfjellet formation. The bulk mineralogy was measured using XRD by commercial laboratory (Weatherford Laboratories) as shown in Table 4.1.

Table 4.1: Mineralogy of Niobrara and Agardhfjellet shales determined by XRD

ID	TOC	Mixed Illite/Smectite	Illite+ Mica	Chlorite	Kaolinite	Total Clay	Calcite	Dolomite	Siderite	Total Carbonate
N1	0.3	2.1	1	0	0	3.1	88.9	1.5	0	90.4
A1	12	31.7	24.6	4.8	0	61.1	0	3.4	2.6	6
	Quartz	Feldspar	Plagioclase	Pyrite	Analcime	Total Other Minerals				
N1	4.7	0.0	1.2	0.6	0.0	6.5				
A1	25.2	0.8	3.2	3.7	0.0	32.9				

### 4.3 Thermogravimetric analysis (TGA)

Introduction: Thermogravimetric analysis (TGA) investigates the effect of temperature on rock minerals. TGA measures the change in mass, commonly a decrease in mass, as a function of time and increasing temperature. When the temperature is increased, minerals are decomposed at temperature range specific to each mineral. Identification of decomposed minerals provide mineral composition in rocks. Other phenomena that occurs during thermal analysis are desorption of adsorbed species, such as water molecules and phase transition. Gips (2014) and, Gips et al. (2014)

have used thermogravimetric analysis to identify these phenomena and recorded the typical temperature range for mineral degradation in rocks.

Principles of operation and experimental details: A known amount of a sample is placed on a reference pan and is exposed to increasing temperature in a furnace, regulated by a pre-programmed test. Inert gas such as Nitrogen is purged into the furnace to remove any oxygen. The sample mass is recorded with time as a function of temperature.

Results: The thermogravimetric analysis for Niobrara (N1) and Agardhfjellet (A1) shales are shown in Figure 4.1 and Figure 4.2 respectively. The analysis shows mass as a function of temperature and its first derivative, indicating significant mass losses. Mass loss indicates mineral degradation. The range of y-axes is kept constant for both samples despite the different original masses used, for comparison purpose.

(i) Niobrara Shale

For Niobrara shale, the absence of peaks at low temperature indicates the lack of free water and clay bound water in the sample, due to lack of clay minerals (Figure 4.1). The major loss of mass occurs at 700°C, corresponding to all calcite mineral. For Niobrara shale sample shown here, any temperature below 500°C can be used in XPS without degrading the sample minerals as the mineral starts to slowly decompose after this temperature.

(ii) Agardhfjellet Shale

Agardhfjellet shale has complex mineralogy and consists of several types of clays and its high organic content indicates kerogen or bitumen content (Table 4.1). For Agardhfjellet, mass loss with increasing temperature is not as significant as Niobrara shale. Figure 4.2 indicates that several minerals are lost with increasing temperature: free and clay bound water are lost at

temperature below 100°C, illite degrades close to 500-550°C, smectite continues to degrade after 600°C, and pyrolysis of kerogen and bitumen starts as early as 400°C. Therefore, care should be taken while determining temperature for XPS studies, as to prevent decomposition of selected minerals. Note that for Agardhfjellet, samples will retain free water and clay bound water if experiments are to be conducted at room temperature.

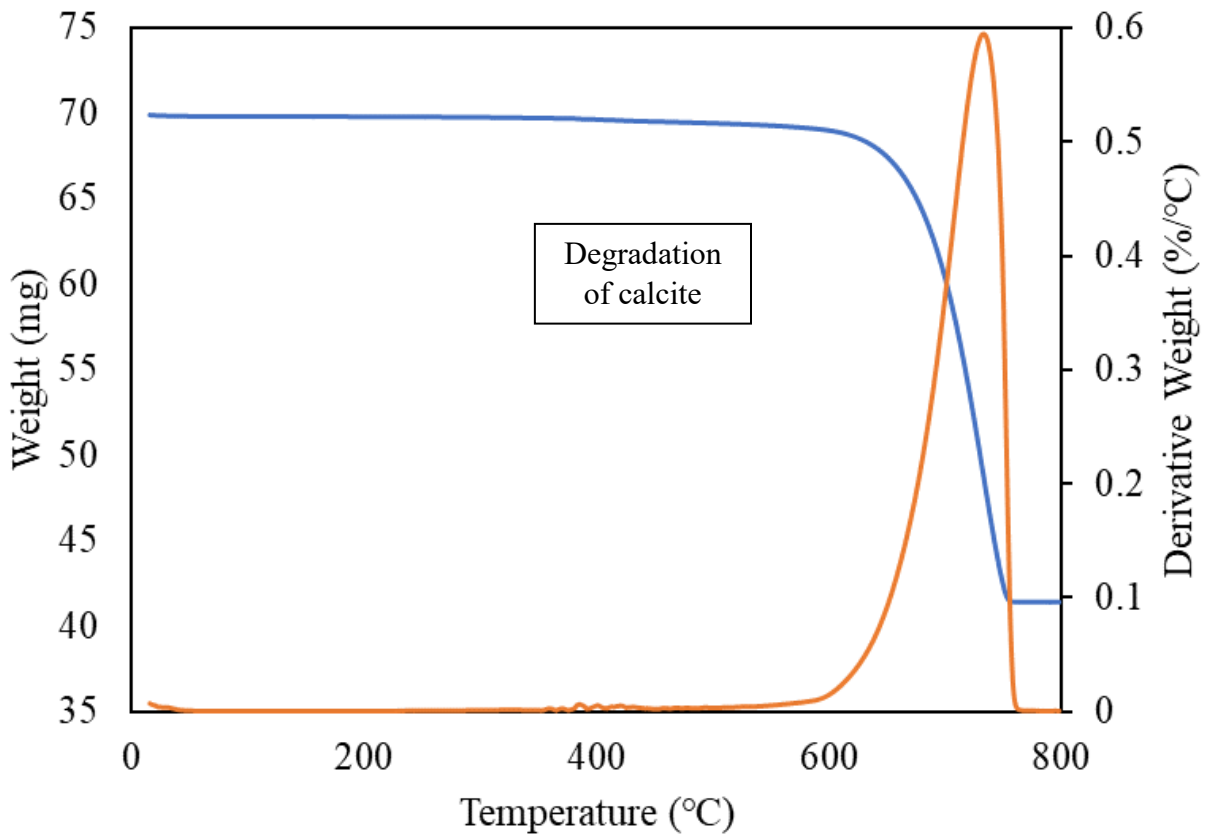


Figure 4.1: TGA and derivative on Niobrara (N1) shale: Major mass loss occurs at 700°C which corresponds to calcite minerals.

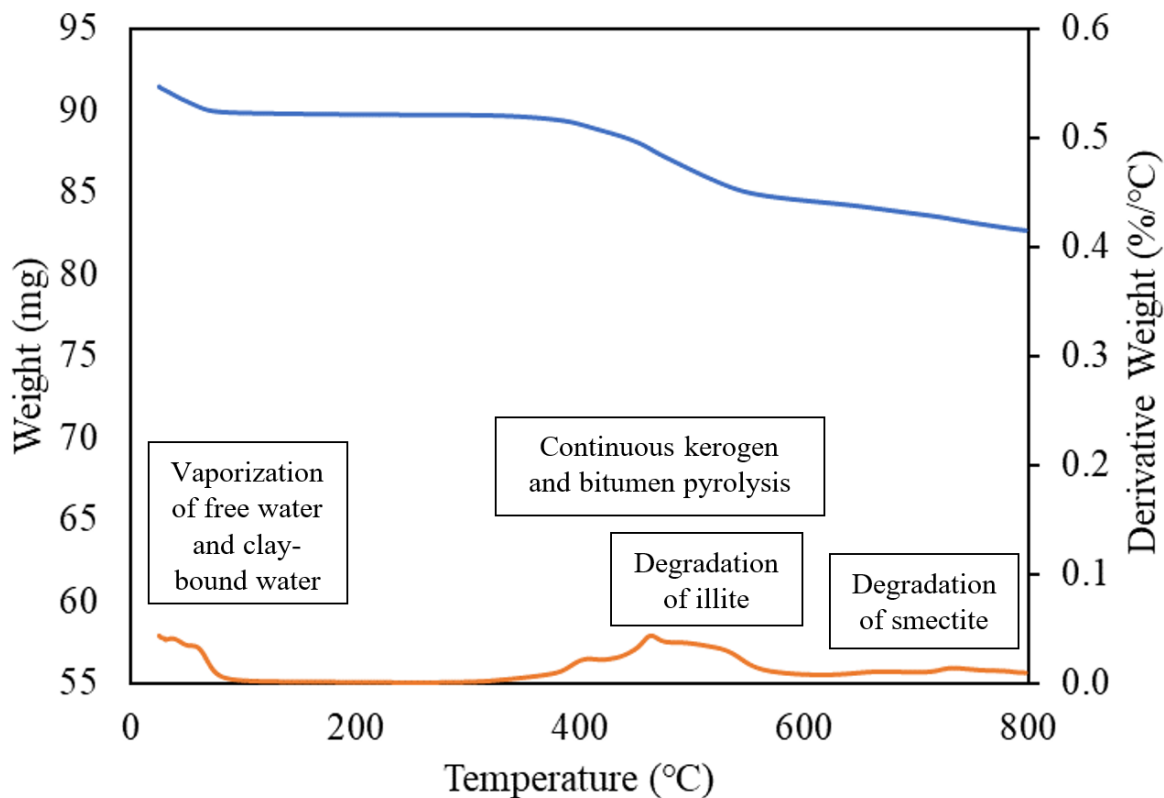


Figure 4.2: TGA and derivative on Agardhfjellet (A1) shale: Thermal analysis shows degradation of illite and smectite minerals at 500°C and 600°C respectively. Due to clay content, the sample loses free water and clay-bound water below 100°C. Due to high organic content of the sample (12%), organic matter matures in increasing temperature after 400°C goes through pyrolysis.

Conclusions: TGA shows mineral degradation at temperature ranges expected for minerals that were predicted by XRD. Thus, TGA and XRD are complementary initial steps for chemical characterization. Agardhfjellet (A1) shale shows desorption of adsorbed species, particularly adsorbed water. Presence of adsorbed water should be noted prior to XPS analysis as adsorbed water will appear in XPS data and affect adsorption studies. Degradation of different minerals is occurring at different temperatures, therefore TGA analysis is a useful initial step to determine potential range of temperatures that can be used in the in-situ gas-solid interactions. Based on the analysis of these two samples, the recommended temperature range for Agardhfjellet (A1) shale is 25-300°C, and for Niobrara (N1) shale is 25-500°C. Above this temperature range, minerals of

interest will degrade. Conducting the analysis at 25°C or room temperature allows us to study the effect of residual moisture on shale-CO<sub>2</sub> interaction.

#### 4.4 Electron Microscopy and Energy Dispersive X-ray Spectroscopy (EDS)

Introduction: Due to the complex mineralogy of rocks, detecting and quantifying multiple elements on heterogeneous surface is challenging. As a first step, elemental composition and heterogeneity of the composition can be evaluated using Environmental Scanning Electron Microscopy (ESEM) and Energy Dispersive X-ray Spectroscopy (EDS). Spatial heterogeneity of rocks is captured using EDS at various (i) accelerating voltages, (ii) magnifications and (iii) areas. Such investigation is important prior to XPS analysis to guide selection of areas and number of areas during XPS analysis. Additionally, sample preparation method is studied to identify the effect of different methods on the preserved surface composition. The samples studied are Niobrara (N1) reservoir rock and Agardhfjellet (A1) caprock as shown in Table 4.1. Common elements expected to be detected with EDS on several minerals are listed in Table 4.2.

Table 4.2: Chemical composition of common rock minerals.

<b>Minerals</b>	<b>Chemical Composition</b>
Quartz	SiO <sub>2</sub>
Plagioclase	NaAlSi <sub>3</sub> O <sub>8</sub> /CaAl <sub>2</sub> Si <sub>2</sub> O <sub>8</sub>
Calcite	CaCO <sub>3</sub>
Dolomite	CaMg(CO <sub>3</sub> ) <sub>2</sub>
Illite/Mica	KAl <sub>3</sub> Si <sub>3</sub> O <sub>10</sub> (OH) <sub>2</sub> / K <sub>y</sub> Al <sub>4</sub> (Si <sub>8-y</sub> ,Al <sub>y</sub> )O <sub>20</sub> (OH) <sub>4</sub>
Mixed Illite-Smectite	K <sub>y</sub> Al <sub>4</sub> (Si <sub>8-y</sub> ,Al <sub>y</sub> )O <sub>20</sub> (OH) <sub>4</sub> / A <sub>0.3</sub> D <sub>2-3</sub> [T <sub>4</sub> O <sub>10</sub> ]Z <sub>2</sub> nH <sub>2</sub> O
Kaolinite	Al <sub>2</sub> Si <sub>2</sub> O <sub>5</sub> (OH) <sub>4</sub>
Pyrite	FeS <sub>2</sub>
Apatite	Ca <sub>5</sub> (PO <sub>4</sub> ) <sub>3</sub> (F,Cl,OH)

Principles of operation and experimental details: In ESEM, a focused beam of electrons is accelerated towards the sample surface. As electrons interact with sample, they produce backscattered electrons, secondary electrons and X-ray energy from electron rearrangement in the atoms. EDS detects the X-ray energy, characteristic of the element from which it was emitted. For ESEM analysis, Agardhfjellet (A1) was placed on sample stage in its original as received state. Niobrara (N1) sample was scanned as received, and compared to sample after polishing. The sample was polished with 100, 220 and 400-grit sandpaper to study the effect of polishing on roughness and possible modification of elemental composition and elemental distributions.

Results: Two samples, Agardhfjellet (A1) and Niobrara (N1) shales, are investigated at varying accelerating voltages, magnifications and areas. While Agardhfjellet (A1) is studied at preserved state, Niobrara (N1) is studied as preserved and polished sample.

#### Agardhfjellet (A1) shale

The as received Agardhfjellet (A1) shale is scanned using ESEM with (i) varying accelerating voltages (10kV and 20kV), (ii) magnifications (X100, X200 and X500), and (iii) areas (area 1, area 2 and area 3).

##### (i) Effect of Accelerating Voltage

The Agardhfjellet shale is scanned at 10 kV and 20 kV accelerating voltages to compare surface composition with bulk composition. Higher accelerating voltage has increased energy level of beam electrons, allowing more electrons to hit the surface and penetrate deeper. Table 4.3 shows the elemental composition in atomic percent for two accelerating voltages (10 kV and 20 kV) at different magnifications and areas on the sample. The atomic percent of silicon is consistently higher at 20 kV, illustrating that there is more silicon in the bulk than at the surface. Silicon is

present in silt-rich minerals such as quartz and clay minerals. Further data in this section is presented at 10 kV to focus on surface properties. 10 kV also decreases the likelihood of charging and surface damage.

Table 4.3: Comparison of different accelerating voltages for Agardhfjellet shale. The boxed values indicate consistently higher silicon content at 20 kV compared to 10 kV.

Elements	Area 1				Area 2			
	100x		500x		100x		500x	
	10 kV	20 kV	10 kV	20 kV	10 kV	20 kV	10 kV	20 kV
C K	3.63	3.12	4.10	3.06	6.15	1.97	3.54	3.77
O K	52.36	52.77	62.62	52.20	65.96	34.37	54.58	56.63
F K	1.11	1.10	1.78	1.15	2.92	0.64	1.30	1.37
Na K	0.35	0.51	0.72	0.61	0.57	0.55	0.51	0.49
Mg K	0.97	1.27	1.17	1.33	1.22	1.43	1.30	1.18
Al K	10.28	9.90	8.44	10.04	7.70	12.16	11.12	9.77
Si K	21.15	23.82	16.28	23.63	13.75	29.44	21.07	21.89
P K	0.09	0.06	0.10	0.07	0.07	0.08	0.00	0.05
S K	2.91	1.88	2.32	2.03	0.45	1.44	0.99	0.87
K K	2.40	2.72	1.37	2.83	0.85	5.00	2.46	2.15
Ti K	2.08	0.80	0.83	0.96	0.19	1.25	0.80	0.40
Fe K	2.67	2.07	0.27	2.09	0.18	11.67	2.32	1.40

(ii) Data at Different Magnifications

The sample is scanned at different magnifications to study variability at different length scales. Table 4.4 shows low standard deviation between elements from different magnifications, illustrating that the elements are uniformly distributed on the surface. Due to the low standard deviation, all further data will be shown at X100 to capture the larger spatial distribution.

Table 4.4: The atomic percent of elements at different magnifications for Agardhfjellet shale.

Elements	Area 3 – 10 kV			Standard Deviation
	X100	X200	X500	
C K	7.48	7.68	10.17	1.50
O K	59.15	59.12	57.38	1.01
Mg K	1.49	1.18	1.35	0.16
Al K	10.22	10.02	9.94	0.14
Si K	17.82	18.06	17.48	0.29
S K	1.13	1.23	1.36	0.12
K K	1.72	1.73	1.82	0.06
Ca K	0.35	0.49	0.26	0.12
Fe K	0.54	0.40	0.23	0.16
Co K	0.08	0.09	0.00	0.05

(iii) Variation between Areas

It is important to study how the distribution of elements vary for different areas on sample surface to understand spatial heterogeneity. Table 4.5 gives the standard deviation for three areas, the major difference being in oxygen, silicon, carbon and aluminum elements. Oxygen shows the highest heterogeneity because it is associated with most minerals present in the rock and varies along with mineral composition across different areas. The heterogeneity within a sample area is studied by focusing on different spots as shown in the example of an area from the Agardhfjellet shale at X500 magnitude (Figure 4.3). There are prominent bright features among the darker background. Average atomic percent distribution of the elements between the bright and dark spots (Table 4.6) shows higher carbon, oxygen, aluminum, silicon, potassium and iron elements at the darker features. These elements are indicative of clay and organic rich minerals. The brighter features have high oxygen and silicon, corresponding to quartz.

Table 4.5: Atomic percent of elements at three different spots on the same Agardhfjellet sample.

Elements	10 kV - 100x			Standard Deviation
	Area 1	Area 2	Area 3	
C K	3.63	6.15	7.48	1.96
O K	52.36	65.96	59.15	6.80
F K	1.11	2.92	-	-
Na K	0.35	0.57	-	-
Mg K	0.97	1.22	1.49	0.26
Al K	10.28	7.70	10.22	1.47
Si K	21.15	13.75	17.82	3.71
P K	0.09	0.07	0.00	0.05
S K	2.91	0.45	1.13	1.27
K K	2.40	0.85	1.72	0.78
Ti K	2.08	0.19	-	1.34
Fe K	2.67	0.18	0.54	1.35

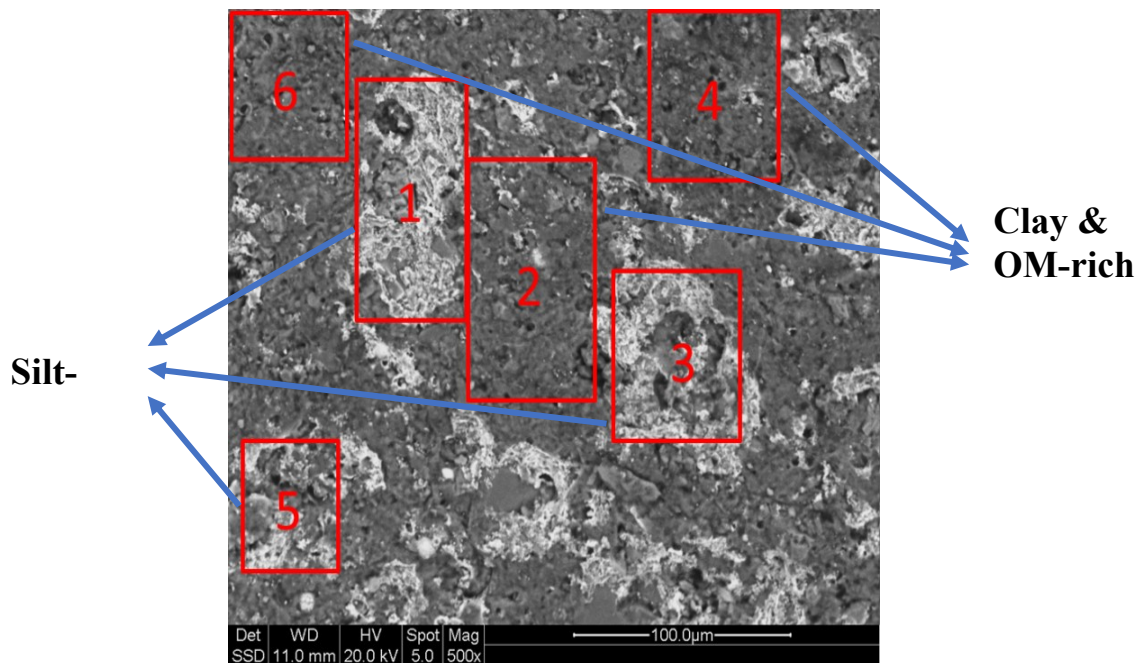


Figure 4.3: Features showing on the Agardhfjellet shale. The bright features are silt-rich due to high oxygen and silicon content. The dark features are possibly clay and organic matter due to its higher carbon, oxygen, aluminum, silicon, potassium and iron elements.

Table 4.6: The average atomic percent of elements at prominent features shown on Figure 4.3.

Elements	Bright Spot	Dark spot	Difference
C K	2.48	3.95	1.47
O K	45.23	39.96	5.27
Mg K	1.56	1.67	0.11
Al K	11.8	13.89	2.09
Si K	27.19	30.34	3.15
S K	2.19	0.89	1.30
K K	3.3	4.59	1.29
Ca K	2.39	0.69	1.70
Fe K	2.63	3.96	1.33

Mapping on the Agardhfjellet shale is also performed to show how well the elements are distributed throughout the sample surface (Figure 4.4).

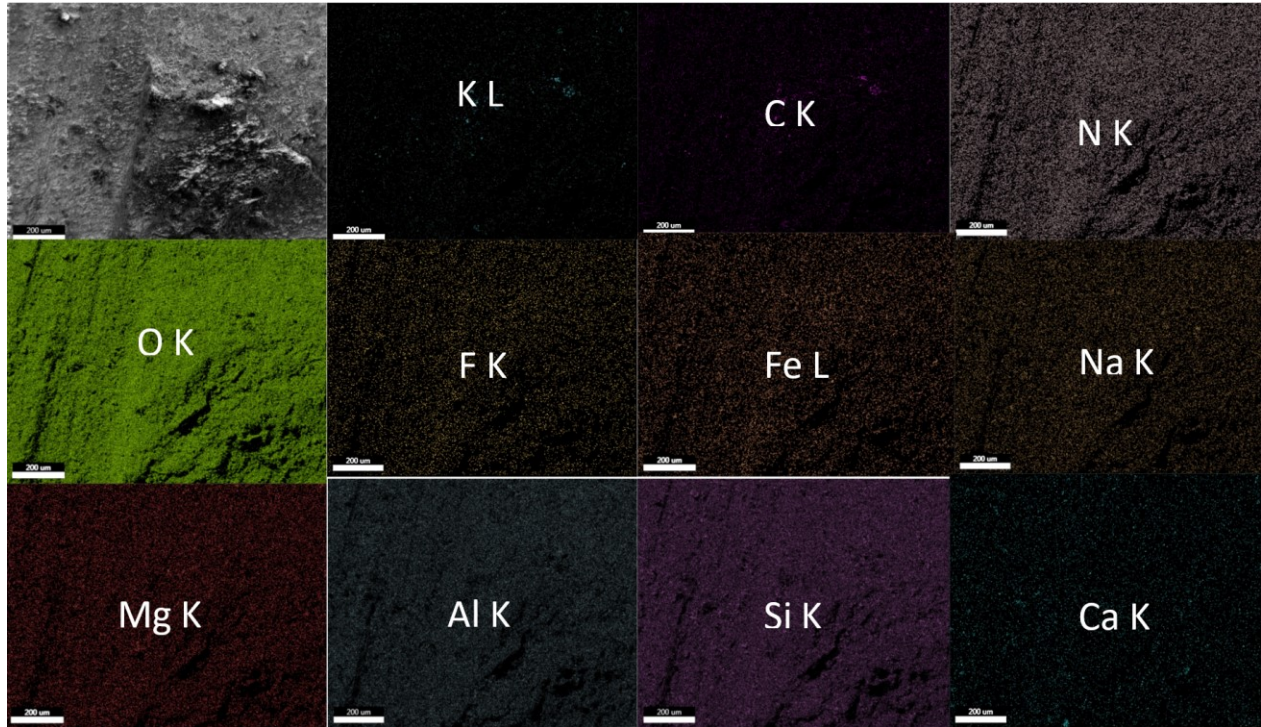


Figure 4.4: Mapping of elements on Agardhfjellet sample surface.

Niobrara (N1) Shale

Both polished and as received Niobrara (N1) shales are scanned using ESEM with (i) varying accelerating voltages (10 kV and 20 kV), (ii) magnifications (X100, X200, X500, X1000 and X3000), and (iii) areas (area 1 and area 2).

(i) Effect of Accelerating Voltages

Different accelerating voltages are also tested for Niobrara shale to distinguish surface composition from bulk composition. For 88.9% calcite-rich Niobrara, every atom of calcium in calcite ( $\text{CaCO}_3$ ) should have an equal amount of carbon and three times the amount of oxygen. This is shown by all the cases in Table 4.7 except for 20 kV at X100 for both areas. Thus, carbon, oxygen and calcium element at 20 kV and X100 in Table 4.7 are boxed as outliers. Carbon element is a lighter element that cannot be accurately captured by ESEM analysis.

Table 4.7: The atomic percent of elements at different accelerating voltages for unpolished Niobrara shale: Carbon, oxygen and calcium element at 20 kV and X100 are boxed as outliers because it does not match the predicted proportion for  $\text{CaCO}_3$  in the calcite-rich Niobrara, where every atom of calcium should have equal amount of carbon and three times the amount of oxygen.

Elements	Area 1				Area 2			
	100x		500x		100x		500x	
	10 kV	20 kV	10 kV	20 kV	10 kV	20 kV	10 kV	20 kV
C K	4.01	1.45	4.25	3.66	8.79	1.68	4.14	4.60
O K	65.99	35.71	65.18	65.77	78.61	34.15	63.97	63.32
Na K	0.54	0.43	0.46	0.38	0.36	0.41	0.59	0.97
Mg K	0.27	0.45	0.49	0.40	0.24	0.47	0.37	0.80
Al K	0.80	1.05	1.04	0.95	0.72	1.08	1.22	1.38
Si K	2.95	3.55	2.41	2.59	2.33	3.67	3.91	3.54
S K	0.20	0.10	0.20	0.03	0.18	0.12	0.00	0.07
K K	0.50	0.48	0.47	0.23	0.17	0.64	0.13	0.28
Ca K	24.74	56.78	25.50	25.99	8.50	56.00	24.51	24.68
Fe K	-	-	-	-	0.10	1.80	1.16	0.36

(ii) Data at Magnifications

Atomic percent at different magnifications is reported to check variations between magnifications for samples prepared differently (see Table 4.8 and Table 4.9 for unpolished and polished Niobrara respectively). Due to the outlier shown at 20 kV for X100, the standard deviation for oxygen in the unpolished sample is high. However, such a high standard deviation is not observed in the unpolished sample at 10 kV and the polished sample at both accelerating voltages. Our analysis shows that majority of elements are consistent throughout varying magnifications. In the following, data are reported at 10 kV for consistency purpose.

Table 4.8: Atomic percent of elements at different magnifications for unpolished Niobrara. The boxes indicate outliers.

Elements	Area 1									
	10 kV				Standard Deviation	20 kV				Standard Deviation
	X100	X500	X1000	X3000		X100	X500	X1000	X3000	
C K	4.01	4.25	3.79	4.52	0.31	1.45	3.66	4.76	4.41	1.53
O K	65.99	65.18	66.10	65.52	0.43	35.71	65.77	64.34	63.50	22.59
Na K	0.54	0.46	0.45	0.45	0.04	0.43	0.38	0.89	1.09	0.30
Mg K	0.27	0.49	0.30	0.34	0.10	0.45	0.40	0.81	0.88	0.25
Al K	0.80	1.04	0.86	0.70	0.14	1.05	0.95	1.15	1.48	0.37
Si K	2.95	2.41	2.88	2.67	0.24	3.55	2.59	2.89	3.57	0.98
S K	0.20	0.20	0.20	0.26	0.03	0.1	0.03	0.15	0.13	0.08
K K	0.50	0.47	0.50	0.43	0.03	0.48	0.23	0.29	0.33	0.16
CaK	24.74	25.50	24.91	25.11	0.33	56.78	25.99	24.74	24.60	14.20

Table 4.9: Atomic percent of elements at different magnifications for polished Niobrara.

Elements	Area 2									
	10 kV				Standard Deviation	20 kV				Standard Deviation
	X100	X200	X500	X1000		X100	X200	X500	X1000	
C K	7.77	9.65	9.52	8.52	0.89	4.09	4.27	3.98	3.93	0.15
O K	79.73	77.97	78.53	79.19	0.77	64.11	64.10	64.39	63.99	0.17
Mg K	0.39	0.51	0.41	0.54	0.07	0.52	0.58	0.65	0.64	0.06
Al K	0.83	0.76	0.88	0.95	0.08	1.16	1.21	1.18	1.23	0.03

Table 4.9 Continued

Si K	2.11	2.03	2.02	2.00	0.05	3.05	2.91	3.12	2.95	0.10
S K	0.05	0.05	0.11	0.00	0.05	0.10	0.09	0.08	0.10	0.01
K K	0.21	0.16	0.10	0.15	0.05	0.29	0.30	0.28	0.29	0.01
Ca K	8.82	8.73	8.32	8.48	0.23	26.32	26.19	25.91	26.48	0.24
Fe K	0.10	0.14	0.12	0.18	0.03	0.36	0.36	0.41	0.39	0.02

## (iii) Variations between Areas

Prominent bright features are also observed on unpolished Niobrara samples (Figure 4.5). There is no distinct difference between the bright and dark features (Table 4.10). Therefore, it can be concluded that the bright spots likely represent marks from cutting the unpolished Niobrara. This shows that cut marks do not remove features from the surface. Note the quality of image is poor due to the low accelerating voltage and lack of coating on the surface.

Table 4.10: The atomic percent of elements for different features on unpolished Niobrara.

Unpolished Niobrara – 10 kV - X1000								
Elements	Spot A – Bright features				Spot B – Dark features			
	A(1)	A(2)	A(3)	Average	B(1)	B(2)	B(3)	Average
C K	4.13	3.84	3.55	3.84	4.46	4.45	4.03	4.31
O K	66.06	67.55	66.96	66.86	63.97	64.65	65.18	64.60
Na K	0.41	0.31	0.59	0.44	0.85	0.50	0.25	0.53
Mg K	0.35	0.14	0.35	0.28	0.62	0.59	0.33	0.51
Al K	0.98	0.78	1.07	0.94	1.40	1.19	0.98	1.19
Si K	2.81	2.05	2.37	2.41	3.42	3.06	3.07	3.18
S K	0.17	0.00	0.00	0.06	0.14	0.22	0.33	0.23
K K	0.69	0.45	0.31	0.48	0.58	0.39	0.62	0.53
Ca K	24.41	24.88	24.81	24.70	24.56	24.97	25.21	24.91



Figure 4.5: The features on unpolished Niobrara sample. Note the poor quality of image is due to obtaining the image from ESEM and low accelerating voltage.

However, there is distinct difference between the ratios of elements on unpolished and polished Niobrara shale (Table 4.11). The polished sample shows high oxygen and carbon element: the oxygen content is eight times higher than the calcium content, in contradiction to the expected proportion for calcite ( $\text{CaCO}_3$ ). Therefore, polishing changes the composition of the original surface. Interestingly, this phenomenon only occurs at the surface composition of polished sample at 10 kV. As shown in Table 4.9, the polished sample retains expected composition for  $\text{CaCO}_3$  at 20 kV despite polishing.

Table 4.11: Comparison of atomic percent of elements between polished and unpolished Niobrara shale. The boxes show outliers because the ratio of the elements does not show expected composition for CaCO<sub>3</sub>.

10 kV - X1000						
Elements	Polished			Unpolished		
	Area 1	Area 2	Average	Area 1	Area 2	Average
C K	8.70	8.52	8.61	3.79	4.16	3.98
O K	79.24	79.19	79.22	66.10	63.80	64.95
Na K	-	-	-	0.45	0.54	0.50
Mg K	0.36	0.54	0.45	0.30	0.18	0.24
Al K	0.69	0.95	0.82	0.86	1.05	0.96
Si K	1.90	2.00	1.95	2.88	3.64	3.26
S K	0.16	0.00	0.08	0.20	0.35	0.28
K K	0.17	0.15	0.16	0.50	0.53	0.52
Ca K	8.64	8.48	8.56	24.91	24.67	24.79
Fe K	0.13	0.18	0.16	-	1.09	1.09

Conclusions: The heterogeneity of rock samples can be in nano- to micro scale, and such elemental heterogeneity across the surface can be captured by ESEM and EDS to determine spatial heterogeneity. Generally, the elements on samples A1 and N1 are uniformly distributed. Unpolished N1 sample is found to preserve original composition compared to the polished sample. This information is useful when determining parameters for XPS analysis. Since the grain sizes of rocks are smaller than the view field of an XPS and XPS spatial resolution is close to 10 μm while the grain sizes in shale are in the scale of nano- to micrometers (Mitchell et al. 1990; Loucks et al. 2009), care should be taken to obtain necessary number of analysis areas per each sample to capture relevant chemistry.

## 4.5 X-ray Photoelectron Spectroscopy (XPS)

Introduction: XPS provides relative quantification of elemental and chemical composition at 5 to 10nm from the surface. With sensitivity of XPS, the method can determine functionalities and oxidation states of elements and detect small differences or changes between samples. Such ability of XPS provides opportunity to understand surface chemistry of rocks in more detail. Additionally, interactions of rocks with gases can be performed using Environmental-XPS to better understand chemical reactions occurring on the rock surface at a fundamental level.

Principles of operation: Ability of XPS to determine elements and differentiate their state is due to the fact that binding energy of photoelectrons ejected upon irradiation with X-rays depends on the type of atom, electron shell and other atoms bound to that atom (Ratner and Castner 1994). Figure 4.6 explains the phenomenon through which photoemission process occurs, leading to the detection of the photoelectrons. The sample is first placed in an ultra-high vacuum environment. X-ray source in XPS produces photons with certain energy directed towards the surface of the sample. The X-ray photon transfers energy to core electrons to overcome electron's binding energy. Core electrons (closest to the nucleus) are at the lowest energy state and have binding energy characteristic of the element. Part of the photon energy is used to overcome the binding energy and the remaining becomes kinetic energy with which the electron escapes, hence the name photoelectrons. The detector in XPS measures the kinetic energy with which the electron passes through the energy analyzer. The binding energy, characteristic of an element, is calculated using Equation 4.1.

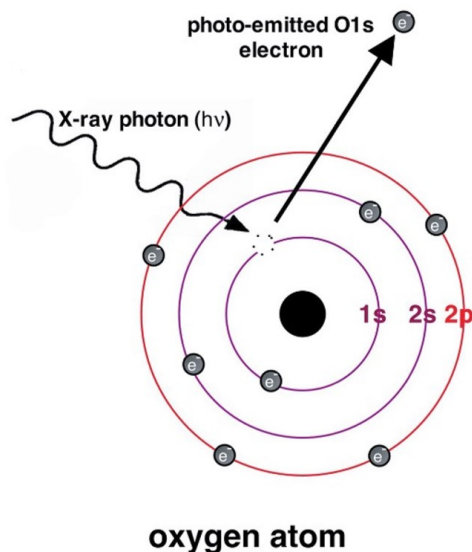


Figure 4.6: Photoemission Effect: As X-ray photons hit the core electron (closest to nucleus and characteristic of the atom), part of the energy is transferred to overcome the binding energy between the electron and nucleus, and the remaining energy becomes kinetic energy with which the photoelectron escapes to energy analyzer. The detector measures the kinetic energy of the photoelectron (Ratner and Castner 1994).

$$E_B = hv - KE - \phi_{sp} \quad (4.1)$$

Where:

$E_B$  = Binding energy of the core electron in an atom

$hv$  = Energy of X-ray source

KE = Kinetic energy with which the photoelectron escapes from an element

$\phi_{sp}$  = Spectrometer work function (specific for instrument)

While  $hv$  and  $\phi_{sp}$  are known values, KE is measured by the energy analyzer. The only unknown calculated, the binding energy, is calculated and collected in a spectrum (Figure 4.7). When accounted for sensitivity factors, area under the peak can provide semi-quantitative elemental composition.

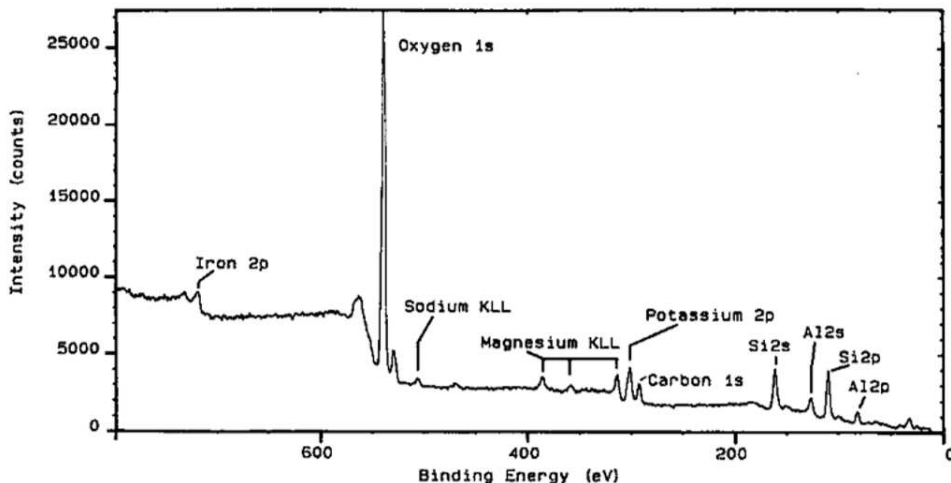


Figure 4.7: Example of low-resolution spectrum obtained from XPS for reservoir rock (Mitchell et al. 1990). s and p refer to the electron's atomic orbital. KLL refers to Auger emission, where additional energy is released from an atom as a result of a higher energy state electron from outer shell transferring to a lower energy state core shell after the previous core electron has vacated upon photoemission.

Literature overview: Very few studies have been reported of XPS characterization for rocks. Surface composition derived from XPS has been used to characterize fine scale wettability (Huang and Holm. 1988; Mitchell et al. 1990; Quet et al. 1991; Toledo et al. 1996; Durand and Beccat 1998; Mercier et al. 1999). XPS-derived surface chemical composition has also been used as supporting data to study rock-fluid interactions (Buckley and Lamb 1995; Feng et al. 2012; Johnson et al. 2014). A literature survey is presented in Table 4.12 concluding the objective, methods and sample preparation shown by Huang and Holm (1988), Mitchell et al. (1990), Quet et al. (1991), Toledo et al. (1996), Durand and Beccat (1998), and Mercier et al. (1999). The main findings of the papers are discussed in this section to evaluate usability of XPS to study wettability and surface interactions of shale rocks in the context of CO<sub>2</sub> storage properties.

The advantage of XPS is its ability to detect light element such as carbon, estimating carbon content. The common findings of past literature demonstrate that XPS-derived elemental

composition, particularly carbon content, can be used to predict oil wettability of reservoir rocks. Sensitivity of XPS allows distinguishing between organic carbon, inorganic carbon and adsorbed air-borne carbon; the distinction is important as wettability properties are affected by the type of carbon. Crude oil tends to preferentially wet organic molecules, therefore the carbon content that determines oil wettability is the organic type.

Organic carbon is present in solid organic matter (source of hydrocarbon), asphaltene (solid component of crude oil), and other polar fractions in crude oil. Typically, more organic carbon is adsorbed on rock surface when the rock is exposed to crude oil for long-term or when organic matter covers the pores. To study the effectiveness of XPS in detecting organic carbon, Huang and Holm (1988) aged the rocks with asphaltene-containing toluene solvent to alter the composition of rock surfaces, allowing more organic molecules to adsorb to rock surfaces (refer to Table 4.12). Aging is a term used when a sample is saturated with certain liquid for a period of time until the sample has reacted with the liquid. After aging with asphaltene, Huang and Holm (1988) observed an increase in organic carbon content of the samples. The organic carbon can be determined by estimating amount of C-H species on the binding energy spectrum (Toledo et al. 1996). The more the organic carbon present on rocks, the more the tendency for it to be oil-wet due to its long exposure to crude oil or coverage by organic matter.

Correlations between carbon content and wettability can be derived using XPS data and Amott-Harvey wettability indices. Amott-Harvey is a core flooding method that provides wettability indices for a drainage process ranging from -1 to 1. -1 refers to highly oil wet and +1 indicates highly water wet. Mitchell et al. (1990), Quet et al. (1991) and Toledo et al. (1996) show the positive correlation between atomic percentage of organic carbon and oil wettability, where oil wet samples show higher carbon content than water wet samples. Due to limited data presented in

each paper (Mitchell et al. 1990; Quet et al. 1991; Toledo et al. 1996), it is difficult to compare all trends. To show correlations for all reported samples, the data from different publications was combined, as shown in Figure 4.8. Note that the lines drawn serve to indicate potential trends.

The collective trend matches the correlation shown by each paper, where oil wet indices (orange dots) show increasing carbon content with stronger oil wetting tendency, and water wet indices (blue dots) show decreasing carbon content with stronger water wetting tendency. Note that for intermediate wet rocks (shown by red box in Table 4.7), the carbon content covers a large range of carbon atomic percent. The intermediate region can also be denoted as weakly oil wet and weakly water wet rocks. Further studies of elemental composition and speciation at this region is required to derive correlations at the intermediate region.

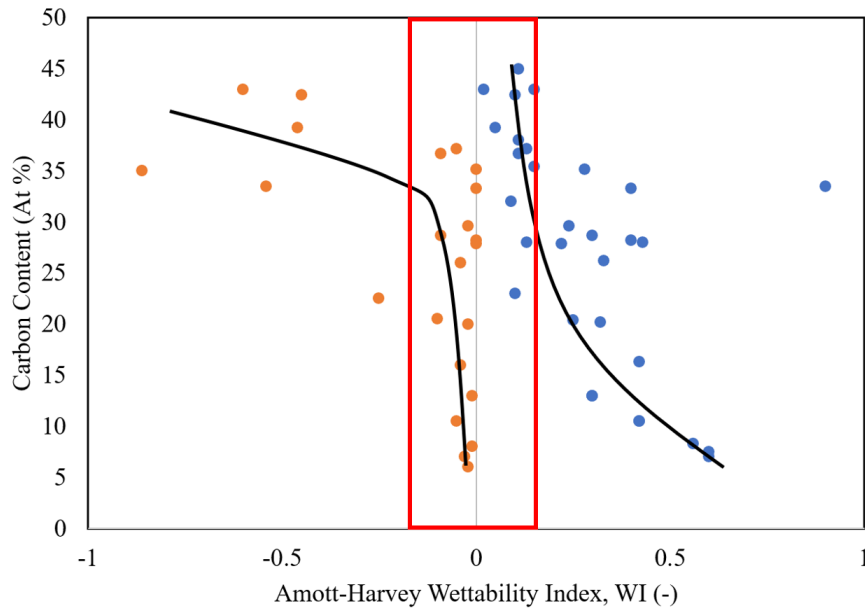


Figure 4.8: Plot of carbon content versus wettability index with data from Mitchell et al. (1990), Quet et al. (1991) and Toledo et al. (1996). Blue dots refer to water wetting indices and orange dots indicate oil wetting indices. The lines are drawn to illustrate potential trends. The stronger the water wetting tendency of rocks, the lower the carbon atomic percent. The stronger the oil wetting tendency of rocks, the higher the carbon atomic percent.

In addition to organic carbon, inorganic carbon and air-borne carbon is also of interest in deriving chemical composition of rock minerals. The inorganic carbon indicates carbonate minerals, while air-borne carbon possibly creates a coating on the surface affecting the surface composition obtained from XPS. Figure 4.9 shows how inorganic carbon (from carbonate mineral) is differentiated from air-borne carbon using the difference in their binding energies (Quet et al. 1991).

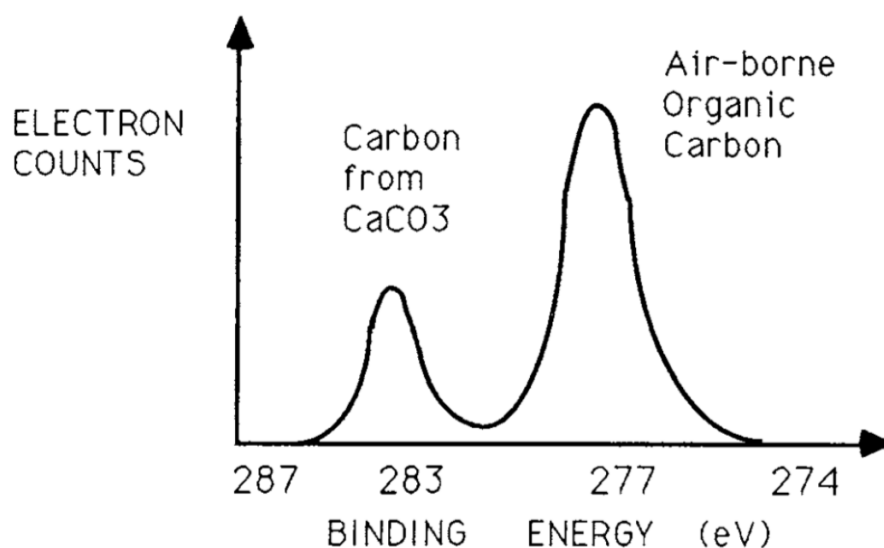


Figure 4.9 : Difference in binding energy of carbon from calcium carbonate and air-borne organic carbon (Quet et al. 1991).

Air-borne carbon content is often significant enough, between 6% to 20% of atomic percentage, to mask the original surface elements (Mitchell et al. 1990; Quet et al. 1991). Using a comprehensive study of carbon contamination on clay minerals, Durand and Beccat (1998) showed that while homogenous carbon coating on the surface does not alter the ratios of Si/Al, K/Al and

O/L (elements of kaolinite and illite), it does reduce their total signal due to inelastic scattering background. Inelastic scattering background is a phenomenon where an electron loses part of its kinetic energy as it escapes from surface due to inelastic interactions, a usual occurrence for electrons from deep within a sample (Ratner and Castner 1994).

Information about presence and nature of other elements and their speciation is also studied to complement the conclusions derived from carbon atomic percentage. Oil wettability was linked to heteroatoms (O, N, S) which are present in the structure of asphaltene, the dissolved solid component of crude oil (Mullins 2011). Therefore, the presence of N and S elements is shown to indicate oil-wettability. The samples were also analyzed to determine hydrophobicity (not attracted to water) of the minerals through the chemistry of Si element. For example, a sample with higher Si-CH as compared to Si-O is considered more hydrophobic (Toledo et al. 1996). The bond of silicon from quartz and phyllosilicates to carbon from organic matter makes it less water-wet. Hydrophilicity (attraction to water), on the other hand, is observed by the elements associated to clay minerals such as K, Mg, Na, Al, Si and O (Huang and Holm 1988; Mitchell et al. 1990).

While elemental characterization using XPS has proven useful in the past, Mitchell et al. (1990) and Durand and Beccat (1998) showed that error in elemental quantification of geological samples ranges from 5% to 20%, suggesting that XPS studies should be coupled with other surface analysis to evaluate the elemental prediction errors and reasons behind these errors. I hypothesize that large variation in XPS data relates to high heterogeneity of some of the samples, highlighting the importance of SEM, FESEM and EDS analysis.

Table 4.12: Literature Review of wettability investigations using X-ray Photoelectron Spectroscopy.

	<b>Core flooding<sup>1</sup></b>	<b>Diagenetic Processes<sup>2</sup></b>	<b>Wettability Restoration<sup>3</sup></b>	<b>Wettability Comparison<sup>4</sup></b>	<b>Carbon Retention and Adsorption<sup>5</sup></b>	<b>Fluid Polarity<sup>6</sup></b>
<b>Objective</b>	<ul style="list-style-type: none"> <li>Investigate oil recovery after core-flooding</li> </ul>	<ul style="list-style-type: none"> <li>Determine surface elemental and chemical compositions</li> <li>Wetting properties</li> <li>Predict diagenetic processes.</li> </ul>	<ul style="list-style-type: none"> <li>Investigate the relation between wettability and surface chemical composition</li> <li>Wettability measurements using core flooding and wettability index</li> <li>Effectiveness of wettability restoration</li> </ul>	<ul style="list-style-type: none"> <li>Evaluate wettability of producing reservoir rocks.</li> </ul>	<ul style="list-style-type: none"> <li>Study carbon retention versus adsorption by comparing surface composition with bulk composition</li> <li>Show how carbon contamination masks surface composition.</li> </ul>	<ul style="list-style-type: none"> <li>Investigate interaction of asphaltenes and pure molecules such as pyridine and pyrrole with major minerals in sandstones</li> </ul>
<b>Samples</b>	<ul style="list-style-type: none"> <li>Sandstone</li> <li>Dolomite and Dolomite chert</li> <li>Limestone</li> </ul>	<ul style="list-style-type: none"> <li>Reservoir rocks (Type not stated)</li> </ul>	<ul style="list-style-type: none"> <li>Carbonate</li> <li>Sandstone (Berea)</li> </ul>	<ul style="list-style-type: none"> <li>Sandstone</li> </ul>	<ul style="list-style-type: none"> <li>Reference clay minerals (KGa-1 and IMt-1) from Clay Minerals Society.</li> <li>Reservoir samples containing diagenetic illite, either platy or fibrous, and/or diagenetic kaolin, either kaolinite or dickite.</li> </ul>	<ul style="list-style-type: none"> <li>Cleaned SiO<sub>2</sub> glass</li> <li>Natural clays (illite, kaolinite)</li> </ul>
<b>Element of Interest</b>	<ul style="list-style-type: none"> <li>Organic C, N<sub>2</sub>, S</li> <li>O<sub>2</sub>, Si, Ca</li> <li></li> </ul>	<ul style="list-style-type: none"> <li>K, Mg, Fe, Na (diagenesis in formation)</li> <li>Al/Si ratio</li> <li>Organic C, N, S</li> <li></li> </ul>	<ul style="list-style-type: none"> <li>Organic C</li> </ul>	<ul style="list-style-type: none"> <li>Organic C</li> <li>Si-CH vs. Si-O</li> </ul>	<ul style="list-style-type: none"> <li>Si/Al ratio</li> <li>K/Al ratio</li> <li>O/Al ratio</li> </ul>	<ul style="list-style-type: none"> <li>N</li> <li>Unsaturated Si</li> <li>Al-O</li> <li>N/C ratio</li> <li>S/C ratio</li> <li>(Si-Al)-O</li> </ul>

Table 4.12 Continued

<p><b>Sample Preparation</b></p>	<ul style="list-style-type: none"> <li>Crushed to a 5-mesh size</li> <li>Washed with naphthalene and toluene to remove oil</li> <li>Dried at 200°F for 16 hours</li> <li>Avoid losing fines while washing.</li> </ul>	<ul style="list-style-type: none"> <li>Freshly exposed fracture surface (1 cm x 1 cm x 0.5 cm) chip</li> </ul>	<ul style="list-style-type: none"> <li>Not stated.</li> </ul>	<ul style="list-style-type: none"> <li>Cored rock cylinder of 1 cm diameter and 3 cm length was cored under fresh water</li> <li>Freshly exposed fracture surfaces obtained by cleaving 1 cm x 1 cm x 0.3 cm chips from each cylinder.</li> </ul>	<ul style="list-style-type: none"> <li>Samples pressed into an indium thin film</li> </ul>	<ul style="list-style-type: none"> <li>Natural clays (1-2µm) pressed into pellets.</li> <li>Slides cleaned with sulphochromic or dichloromethane-ethanol 1/1 solution</li> </ul>
<p><b>Sample Conditions</b> <b>Note:</b> <b>Samples are aged in mineral oil to make it oil-wet before studying its predicted wettability.</b></p>	<ul style="list-style-type: none"> <li>Original rock sample</li> <li>Dean-Stark extraction: removes oil and water from the sample</li> <li>Fired sample (at 1300°F)</li> <li>Asphaltene-treated sample (toluene solution with 1% asphaltene)</li> </ul>	<ul style="list-style-type: none"> <li>Fresh (as cleaved)</li> <li>Baked (exposed to 400°C in drying oven for 24 hours): to remove N, S, and reduces Al/Si.</li> <li>Plasma ashing: to remove carbon</li> </ul>	<ul style="list-style-type: none"> <li>Aged with reservoir crude oil for 3 weeks at 80°C and constant pressure.</li> <li>Cleaned with toluene and isopropanol to reduce the amount of residual oil present, and dried with N<sub>2</sub>.</li> <li>Or</li> <li>No aging.</li> <li>Original samples are flooded with brine, isopropanol, isopropanol/toluene and toluene, at room temperature, and dried with N<sub>2</sub>.</li> </ul>	<ul style="list-style-type: none"> <li>Utilized several different cleaning methods for each sample (refer to Toledo et al. 1996).</li> </ul>	<ul style="list-style-type: none"> <li>Samples aged in crude oil for a month at room temperature.</li> <li>After aging, the samples were cleaned by rinsing once in cyclohexane, sieved and dried at room temperature.</li> </ul>	<ul style="list-style-type: none"> <li>Samples first aged for six weeks with ‘Arabial Light’ asphaltene (contains nitrogen and sulfur) and pure light components such as pyridine and pyrrole.</li> <li>After aging, the samples were rinsed with DI water or toluene and dried at 60°C.</li> </ul>

Table 4.12 Continued

<p><b>Supporting Experiments</b></p>	<p>Core-flooding with, (i) continuous CO<sub>2</sub> injection, (ii) single-slug CO<sub>2</sub> injection (followed by water), and (iii) CO<sub>2</sub> WAG injection, at miscible reservoir conditions of 120°F and 2500 psig.</p> <ul style="list-style-type: none"> <li>• Measure volume of oil recovered (typically high for water-wet rocks)</li> </ul>	<p>Laser Ionization Mass Analysis (LIMA)</p> <ul style="list-style-type: none"> <li>• To measure high sensitivity trace elements, to detect organic compounds adsorbed on refractory materials.</li> </ul> <p>Amott-Harvey</p> <ul style="list-style-type: none"> <li>• Determines wettability index</li> </ul> <p>Water/Oil Relative Permeability</p> <ul style="list-style-type: none"> <li>• Fluid with lesser affinity to the rock tends to have better relative permeability.</li> </ul>	<p>Amott-Harvey</p> <ul style="list-style-type: none"> <li>• Determines wettability index</li> </ul>	<p>Amott-Harvey</p> <ul style="list-style-type: none"> <li>• Determines wettability index</li> </ul>	<p>Simulation</p> <ul style="list-style-type: none"> <li>• Evaluates carbon coating thickness, or the coverage ratio.</li> </ul> <p>X-ray Diffraction, Elemental analysis, Infra-red EDS</p> <ul style="list-style-type: none"> <li>• Determines stoichiometric formula</li> </ul>	<p>Nuclear Microprobe Analysis</p> <ul style="list-style-type: none"> <li>• Quantitative analysis of elements in an area of 100 μm<sup>2</sup> and depth of tens of microns. It gives the chemical composition at larger depth than XPS.</li> </ul>
--------------------------------------	--	---	--	--	--	---

<sup>1</sup>Huang and Holm 1988

<sup>2</sup>Mitchell et al. 1990

<sup>3</sup>Quet et al. 1991

<sup>4</sup>Toledo et al. 1996

<sup>5</sup>Durand and Beccat 1998

<sup>6</sup>Mercier et al. 1999

## 4.6 Ambient Pressure X-ray Photoelectron Spectroscopy (AP-XPS)

### 4.6.1 Capabilities of AP-XPS

Typical XPS experiment requires operation under ultra-high vacuum conditions ( $10^{-9}$  torr). The high vacuum prevents photoelectrons from colliding with other gas particles and maintains an operational environment for the X-ray source (Ratner and Castner 1994). The near ambient-pressure XPS (AP-XPS) allows to conduct studies at much less stringent vacuum conditions, that allow to measure solid-vapor and solid-liquid-vapor at near ambient pressure and temperatures as high as 800°C. With AP-XPS, the chemical reactions of rocks with dosing gases such as H<sub>2</sub>O, CO<sub>2</sub> and CH<sub>4</sub> can be investigated. While there is no AP-XPS data reported for investigation of rocks, these types of studies have been conducted for other materials and applications. This includes investigation of catalysts employed in various catalytic reactions (Óvári et al. 2013).

Figure 4.10 shows an example of AP-XPS study of perovskite film (thin film used in material science) in the presence of water (Stoerzinger et al. 2015). Figure 4.10 shows high-resolution spectra for oxygen element on the thin film at varying temperatures (25°C, 150°C, 300°C) in the presence of 100 mTorr H<sub>2</sub>O. Note the smaller curves drawn inside of the larger binding energy peak: The curves are deconvoluted using standard curve-fitting procedures. The areas under the peaks correspond to oxygen species with different bonding and speciation.

In the experiment, Stoerzinger et al. (2015) increases the relative humidity in the sample by decreasing the temperature. According to Stoerzinger et al. (2015), the clean film at 300°C shows bulk oxygen from film, surface oxygen and OH<sup>-</sup> from initial H<sub>2</sub>O reaction. Due to affinity of CO<sub>2</sub> to the thin film, CO<sub>2</sub> traces in the chamber reacts with the sample, forming CO<sub>3</sub><sup>2-</sup> at 150°C. As the temperature is further decreased, adsorption of water occurs. The purpose of showing this example is to demonstrate how adsorption, chemical reactions and formation of products during

exposure of the rocks to relevant environments ( $\text{CO}_2$ ,  $\text{H}_2\text{O}$ ,  $\text{CH}_4$ , etc.) can be investigated using detailed analysis of XPS data.

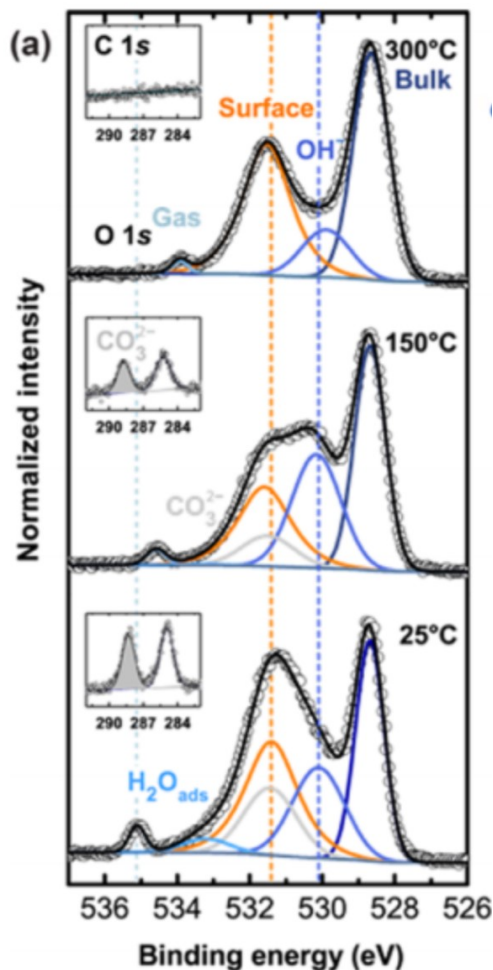
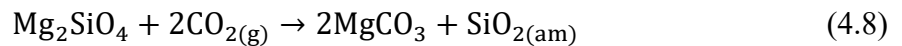


Figure 4.10: O 1s XPS spectra acquired from perovskite film with  $\text{H}_2\text{O}$  at different temperatures (Stoerzinger et al. 2015) demonstrating shifts due to interactions between perovskite and water: At  $300^\circ\text{C}$ , the deconvoluted O 1s spectrum shows bulk oxygen from film, surface oxygen and  $\text{OH}^-$  from initial  $\text{H}_2\text{O}$  reaction. At  $150^\circ\text{C}$ ,  $\text{CO}_2$  traces in the chamber reacts with the sample, forming  $\text{CO}_3^{2-}$ . As temperature is cooled, adsorption of water occurs.

#### 4.6.2 Potential of XPS and AP-XPS for investigation of Mineral Carbonation

Although past studies have largely concentrated on the interaction of crude oil on pore surfaces, the ability of XPS to predict fine-scale wettability can be used to study rock- $\text{CO}_2$

interactions. Given the increasing interest in CO<sub>2</sub> sequestration, I investigated the use of XPS to study chemical alteration due to interactions along CO<sub>2</sub> pathways in the subsurface. As CO<sub>2</sub> reacts with rock minerals and dissolves in residual fluids, surface chemical reactions can chemically transform some minerals, a process known as mineral carbonation. Since mineral carbonation is considered as a long-term carbon trapping mechanism in the subsurface, an integration of theoretical models and experimental observation is necessary to understand and quantify the carbonation process. Several elements in the subsurface can be carbonated, but alkaline earth metals such as calcium, magnesium and iron are most studied (Sipilä et al. 2008). Shown below is reaction steps for magnesium carbonation from forsterite (Mg<sub>2</sub>SiO<sub>4</sub>) dissolution (Hopkinson et al. 2008; Johnson et al. 2014).



The process illustrated in the reactions (4.2) to (4.8) can be separated into dissolution of magnesium silicate (4.2), precipitation of amorphous silica (4.3), and precipitation of magnesium carbonate (4.4-4.8). Carbonation process takes years to reach reaction equilibrium in the subsurface. Experimentally, several carbonation steps are evaluated to speed up the reaction: direct

gas-mineral carbonation in the presence and absence of aqueous environments and additives, and multi-step indirect carbonation with the aid of acetic acid, low pH and other additives (Sipilä et al. 2008). The multi-step process separates the reaction of mineral carbonation into several steps, reducing the total time for each reaction studied individually.

Given the increasing interest in CO<sub>2</sub> sequestration, both XPS and AP-XPS can be used to investigate chemical alteration due to interactions along CO<sub>2</sub> pathways in the subsurface, providing complementary information. First, regular XPS at ultra-high vacuum can be used to study samples before and after CO<sub>2</sub> treatment at high pressure and temperature conditions that expediate mineral carbonation process. Second, AP-XPS can be used to study the in-situ interactions to gain insights on the carbonation mechanism itself.

#### **4.6.3 Proposed Workflow for Investigation of Gas-solid Interactions using XPS and AP-XPS, along with Complementary Techniques**

Given the different factors discussed, I developed a workflow for XPS analysis as shown in Figure 4.11. As described in previous sections, XRD, SEM/EDS, and TGA provide preliminary characterization of rock surfaces, in terms of bulk mineralogy, elemental composition and adsorbed species. The preliminary analysis provides valuable information for sample preparation and analysis conditions. Regular XPS analysis can be conducted on initial samples and after exposing the samples to conditions that rapidly alter the chemistry and morphology of the rocks. Such conditions include CO<sub>2</sub> at high temperature and high pressure. With ambient pressure XPS, some of the conditions relevant to rock interactions with CO<sub>2</sub> can be investigated. Of particular interest are interactions of rock minerals with different chemistry and morphology with various fluids (carbon dioxide, water and methane gas) at varying temperature conditions.

**Preliminary Analysis:**

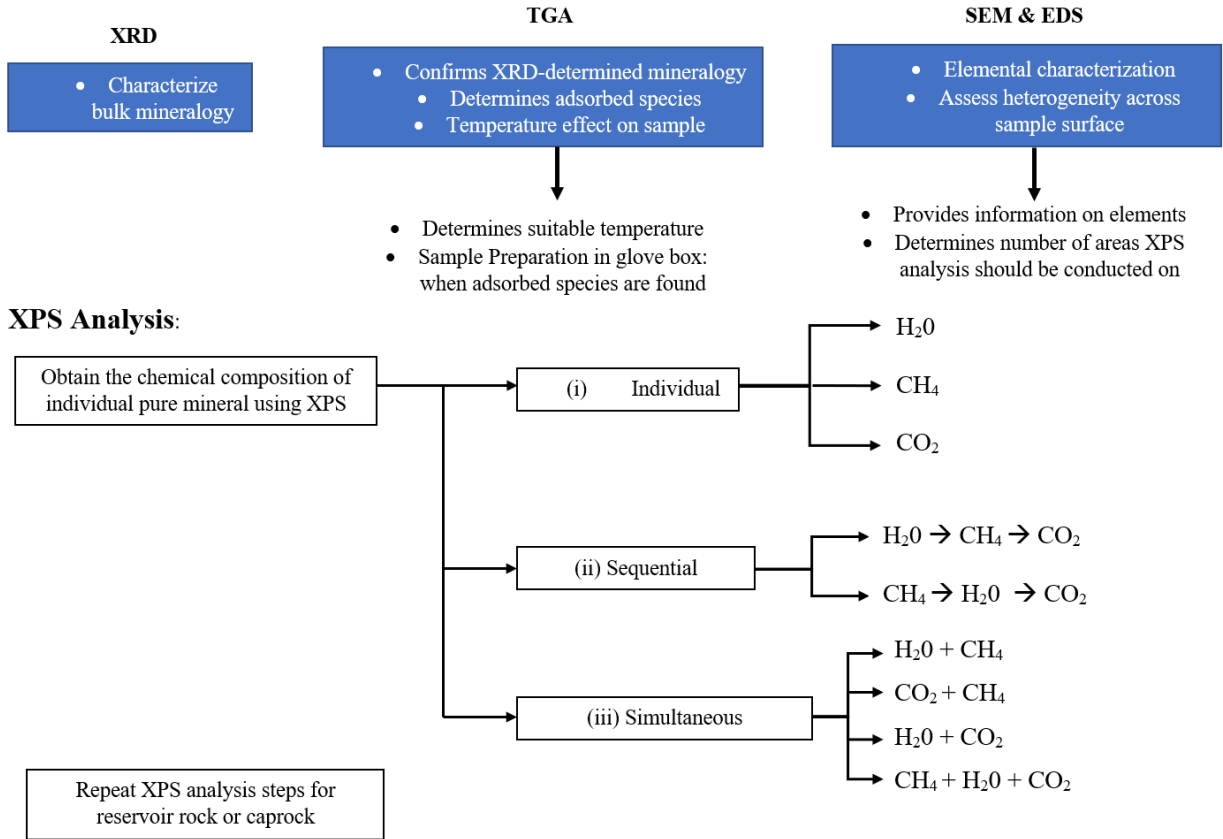


Figure 4.11: The Experimental Plan for ambient-pressure XPS. The colored boxes are preliminary steps.

Minerals: Due to the polyminerale nature of rocks, it will be useful to conduct XPS analysis on individual minerals before analyzing a composite shale sample. Thus, XPS analysis of rocks require identification of minerals and their interactions with introduced fluid. The minerals of interest are minerals commonly found in reservoir and cap-rocks as shown in Table 4.1. Hellevang et al. (2013) lists the divalent cation minerals capable of forming carbonates with CO<sub>2</sub> reaction.

Fluids: The fluids can be dosed (i) individually, (ii) sequentially, and (iii) simultaneously.

(i) The fluids such as water, methane and CO<sub>2</sub> can be dosed individually to assess their direct reaction with the rock minerals. Water and methane are naturally occurring fluids in the reservoir, whereas CO<sub>2</sub> can be naturally occurring or introduced for enhanced oil recovery and storage purposes. For controlled moisture condition in XPS analysis, the sample can be degassed with heat treatment in a glove box to eliminate the naturally adsorbed water. Then, moisture can be introduced at specified rate, temperature and pressure in the XPS chamber to accurately quantify the effect of amount of water and experimental conditions on the sample.

(ii) Sequentially, water can be injected followed by methane and finally, CO<sub>2</sub>. Water is of interest because it is naturally present in rocks at irreducible saturation. Following water, methane gas can be dosed to introduce the hydrocarbon molecules that are often trapped in some pores of the rocks in formation. Finally, CO<sub>2</sub> can be introduced to study the reaction of CO<sub>2</sub> in the presence of moisture and hydrocarbon with the minerals. For oil-wet rocks, however, the hydrocarbon molecules will be adsorbed to the rock surface. Thus, the dosing can be changed to methane followed by water vapor and CO<sub>2</sub> in a sequential manner.

(iii) The fluids can also be dosed simultaneously to study preferential adsorption of fluids at different spots on the sample. This necessitates spatial mapping of the chemical composition on the rocks. For simultaneous, any two gases from water vapor, methane and CO<sub>2</sub> can be dosed together. For the final step, the three gases can be dosed together.

Temperature: The kinetics of carbonation reaction is governed by the empirical Arrhenius equation (Laidler 1984):

$$k = Ae^{-\left(\frac{E_a}{RT}\right)} \quad (4.9)$$

Where:

$k$  = Rate constant

$A$  = Frequency factor

$E_a$  = Activation energy

$R$  = Gas constant

$T$  = Temperature

According to Equation 4.9, temperature is a controlling factor of rate of reaction. Temperature increases the frequency of collisions, rendering higher kinetic energy to more molecules to overcome the activation energy ( $E_a$ ) of the reaction (Arrhenius 1889). Hence, temperature effect should be evaluated on the reaction through XPS analysis at various temperatures. AP-XPS has ability to regulate temperature up to 800°C. Note that high temperature could alter the minerals, causing phase transition of organic matter and thermally degrading some minerals. Thus, a thermal analysis such as Thermogravimetric Analysis (TGA) especially on organic-rich shale rocks, is necessary to identify appropriate temperature range.

## CHAPTER 5

### SUMMARY AND CONCLUSION

In this thesis, I addressed two related concepts: wettability and storage capacity. With the rising interest in using and storing CO<sub>2</sub> in the subsurface, I emphasized wettability and storage capacity related to CO<sub>2</sub>. Mineral composition controls nano-scale microstructure in shales and its wetting properties, hence controlling storage capacity. Due to the complexity of shale mineralogy, I investigated shales rich in specific minerals (e.g. calcite, clay, organic) and pure minerals (e.g. calcite, quartz) to isolate the behaviors of individual minerals. I used both CO<sub>2</sub>- and N<sub>2</sub>-adsorption because the combination provides the complete range of pore size distribution from ultra-micropore to mesopore (0.3 nm-50 nm). Specific interaction between the minerals and CO<sub>2</sub> can be studied at the micropore region (pore diameter up to 0.7 nm) because at this pore size, only one monolayer of CO<sub>2</sub> (molecular diameter of 0.232 nm) on the pore walls can be accommodated.

#### **5.1 Calcite – CO<sub>2</sub> Interaction**

Calcite- CO<sub>2</sub> reaction was investigated by conducting continuous tests of CO<sub>2</sub> on calcite-rich, clay-rich and organic-rich samples. The total CO<sub>2</sub> adsorbed reduced with consequent runs in calcite-rich samples, but not in clay-rich or organic-rich samples. Further investigating the pore size distribution of the calcite-rich N1 sample, I identified that N1 with 88.9% calcite content by weight has permanently trapped some CO<sub>2</sub> in the ultra-micropore region (2-4Å). Permanent trapping can be due to the presence of chemisorbed water in calcite that dissolves the CO<sub>2</sub>, or due to pore condensation phenomena in specific pores of N1. The volume of CO<sub>2</sub> trapped in the ultra-micropore is estimated to be 0.10 Tonnes/acre ft /82.98 kilotonnes/km<sup>3</sup>.

## 5.2 Organic Matter – CO<sub>2</sub>

Organic-rich samples, B1 and A1, are studied to understand the distribution of organic matter and its effect on CO<sub>2</sub> storage capacity. N<sub>2</sub>-derived PSD and CO<sub>2</sub>-derived PSD are compared, and both show a gradual increase of micropore region with the extraction of soluble organic matter, indicating that the dominant pore size of kerogen is micropores (Pore diameter < 2nm) (Kuila 2013; Zargari et al. 2015). Affinity of CO<sub>2</sub> towards organic matter can also lead to an increase in CO<sub>2</sub> sorption (Edwards et al. 2015). Interestingly, the specific surface area (SSA) and cumulative pore volume of B1 shale decreased after chloroform extraction, similar to a number of samples presented by Zargari et al. (2015). I assume that the decreasing SSA and cumulative pore volume are due to some minerals in the pores dissolving in chloroform and redepositing into the pores due to inefficient extraction. CO<sub>2</sub> storage capacity of kerogen-hosted pores is calculated for an area and thickness used by Nuttall et al. (2005) who estimated the storage capacity of Devonian shales underlying Kentucky to be 28 Gt. For a similar area, the pore volume derived from CO<sub>2</sub>+N<sub>2</sub> adsorption demonstrates a capacity to store at least three times higher amounts of CO<sub>2</sub> than the literature-provided estimate (28 Gt) in Agardhfjellet (A1). For Bakken (B1), however, the reported storage capacity derived from CO<sub>2</sub>+N<sub>2</sub> adsorption is lower than one half of literature-provided estimate. The CO<sub>2</sub>-derived ultra-micropore volume in both samples suggest storage capacities of around 1-2 Gt. Typically, the soluble organic matter will evacuate the pores after reaching post mature stage, providing additional storage space. The total volume (ultra-micropore to mesopore) that can be trapped by kerogen pores after maturation in A1 and B1 are estimated to be 13.2 Gt and 1.2 Gt respectively for the same reservoir volume used by Nuttall et al. (2005). Hence, the kerogen-hosted pores can be targeted as CO<sub>2</sub> storage site.

### **5.3 Surface Free Energy**

Gas adsorption studied above is mainly governed by temporary polarization due to London dispersion forces. I studied surface free energy of shales in terms of intermolecular forces such as van der Waals forces, Lewis acid-base interactions and polarity of the molecules. The surface free energy of shales is dominated by Lifshitz van der Waals, particularly the London dispersion forces (38-48 mN/m). The result is validated by surface free energy found for shales by Zelenev (2011). Therefore, subcritical gas adsorption conducted in this work sufficiently accounts for the major interaction force on pores of shale, the London dispersion forces. Individual minerals, such as calcite and quartz, have strong surface forces in terms of van der Waals and Lewis acid-base, or polar and dispersive components. However, the values cannot be validated as the inversion models do not compare to each other.

### **5.4 X-ray Photoelectron Spectroscopy**

Besides surface free energy described, surface chemistry equally governs the interaction at rock-fluid interface. Thus, I explored the use of XPS for chemical characterization of rocks, of both the surface and reactions at the interface. Prior to XPS characterization of elements present on the surface, I determined bulk mineralogy of the samples using XRD and confirmed with TGA. TGA shows the presence of adsorbed water molecules on A1 shale, which should be considered during XPS analysis. I performed elemental characterization using electron microscopy and EDS to assess the heterogeneity throughout the sample area. The spatial elemental composition across different number of areas allows understanding of chemistry of the rock and respective interactions. In the past, XPS was used to determine oil wettability with the determination of organic carbon content and the presence of nitrogen and sulfur elements on the surface. This work should be expanded to include more detailed analysis of all elements and their speciation through

curve fitting and correlations between all elements. Another capability of XPS that should be explored is studies of fluid-rock interactions, which can be achieved using AP-XPS and dosing relevant gas molecules such as CO<sub>2</sub>, H<sub>2</sub>O and CH<sub>4</sub>, in different combinations and sequences. For example, a sequence where CO<sub>2</sub> is introduced following exposure to CH<sub>4</sub> and H<sub>2</sub>O can be useful for mineral carbonation study in the presence of moisture and hydrocarbon molecules and have implications for CO<sub>2</sub>-EOR studies.

## 5.5 Conclusion

The main findings of this thesis are:

- Calcite minerals or specific pore structure of shales can permanently trap CO<sub>2</sub> through dissolution or pore condensation respectively. The volume trapped should be taken into account during CO<sub>2</sub>-EOR. Therefore, ultra-micropore characterization of shales should be analyzed before planning CO<sub>2</sub>-EOR for shale formations.
- The additional CO<sub>2</sub> that can be stored upon complete maturation of organic matter should be taken into account while planning CO<sub>2</sub> storage sites in organic-rich formations.
- Surface free energy of shales are dominated by van der Waals forces, which governs the physisorption during gas adsorption experiments conducted.
- A workflow is provided for XPS and AP-XPS studies, along with complementary techniques, particularly for the purpose of investigating the mineral carbonation process.

## LIST OF ABBREVIATIONS AND NOMENCLATURE

AP-XPS:	Ambient Pressure X-ray Photoelectron Spectroscopy
BET:	Brunauer, Emmett, Teller
BJH:	Barrett, Joyner, Halenda
CCUS:	Carbon Capture, Utilization and Storage
DA:	Dubinin-Asthakov
DFT:	Density Functional Theory
DR:	Dubinin-Radushkevich
$E_b$ :	Binding Energy
EDS:	Energy Dispersive Spectroscopy
EOR:	Enhanced Oil Recovery
ESEM:	Environmental Scanning Electron Microscopy
G:	Gibbs Free Energy
HI:	Hydrogen Index
HK:	Horvath-Kawazoe
IUPAC:	International Union of Pure and Applied Chemistry
KE:	Kinetic Energy
MP:	Micropore Analysis
OI:	Oxygen Index
PSD:	Pore Size Distribution
SF:	Saito-Foley
SSA:	Specific Surface Area
TGA:	Thermogravimetric Analysis
$T_{max}$ :	Maximum temperature

TOC:	Total Organic Carbon
XPS:	X-ray Photoelectron Spectroscopy
XRD:	X-ray Diffraction
$\gamma^-$ :	Electron Acceptor
$\gamma^+$ :	Electron Donor
$\phi_{sp}$ :	Spectrometer Work Function
$h\nu$ :	Energy of X-ray Source
$\gamma$ :	Surface Tension
$\theta$ :	Contact Angle

## REFERENCES CITED

- Aman, Z.M., Leith, W.J., Grasso, G.A., Sloan, E.D., Sum, A.K. and Koh, C.A. 2013. Adhesion Force Between Cyclopentane Hydrate and Mineral Surfaces. *Langmuir* **29**(50):15551-15557.
- Ambrose, R.J., Hartman, R.C., Diaz-Campos, M., Akkutlu, I.Y. and Sondergeld, C.H. 2012. Shale Gas-in-place Calculations Part I: New Pore-scale Considerations. *SPE Journal* **17**(1): 219-229.
- Anderson, W.G., 1986. Wettability Literature Survey-Part 3: The Effects of Wettability on the Electrical Properties of Porous Media. *Journal of Petroleum Technology* **38**(12): 1-371.
- Arrhenius, S. 1889. On the reaction velocity of the inversion of Cane Sugar by Acids. *Zeitschrift fur physikalische Chemie* **4**: 226.
- Aspenes, G., Dieker, L.E., Aman, Z.M., Høiland, S., Sum, A.K., Koh, C.A. and Sloan, E.D. 2010. Adhesion Force Between Cyclopentane Hydrates and Solid Surface Materials. *Journal of Colloid and Interface Science* **343**(2): 529-536.
- Benson, S.M., Bennaceur, K., Cook, P., Davison, J., de Coninck, H., Farhat, K., Ramirez, C.A., Simbeck, D., Surles, T., Verma, P. and Wright, I. 2012. Carbon Capture and Storage. *Global Energy Assessment-Toward a Sustainable Future*: 993.
- Brunauer, S., Emmett, P.H. and Teller, E. 1938. Adsorption of Gases in Multimolecular Layers. *Journal of the American Chemical Society*, **60**(2): 309-319.
- Buckley, A.N. and Lamb, R.N. 1996. Surface Chemical Analysis in Coal Preparation Research: Complementary Information from XPS and ToF-SIMS. *International Journal of Coal Geology* **32**(1-4): 87-106.
- Busch, A., Amann-Hildenbrand, A., Bertier, P., Waschbuesch, M. and Krooss, B.M. 2010. The Significance of Caprock Sealing Integrity for CO<sub>2</sub> Storage. Presented on the SPE Symposium on CO<sub>2</sub> Capture, Storage, and Utilization., New Orleans, Louisiana, 10-12 November. SPE-139588-MS. <https://doi.org/10.2118/139588-MS>
- Chalmers, G.R. and Bustin, R.M. 2007a. On the Effects of Petrographic Composition on Coalbed Methane Sorption. *International Journal of Coal Geology* **69**(4): 288-304.
- Chalmers, G.R. and Bustin, R.M. 2007b. The Organic Matter Distribution and Methane Capacity of the Lower Cretaceous Strata of Northeastern British Columbia, Canada. *International Journal of Coal Geology* **70**(1-3): 223-239.
- Chibowski, E. and Perea-Carpio, R. 2002. Problems of Contact Angle and Solid Surface Free Energy Determination. *Advances in Colloid and Interface Science* **98**(2): 245-264.

- Clarkson, C.R., Freeman, M., He, L., Agamalian, M., Melnichenko, Y.B., Mastalerz, M., Bustin, R.M., Radliński, A.P. and Blach, T.P. 2012. Characterization of Tight Gas Reservoir Pore Structure Using USANS/SANS and Gas Adsorption Analysis. *Fuel* **95**: 371-385.
- de Boer, J.H., Lippens, B.C., Linsen, B.G., Broekhoff, J.C.P., Van den Heuvel, A. and Osinga, T.J. 1966. The T-curve of Multimolecular N<sub>2</sub>-adsorption. *Journal of Colloid and Interface Science* **21**(4): 405-414.
- Donaldson, E. and Alam, W. 2008. *Wettability*. Houston, Texas: Gulf Publishing Company.
- Drelich, J. 2013. Guidelines to Measurements of Reproducible Contact Angles Using a Sessile-Drop Technique. *Surface innovations* **1**(4): 248-254.
- Durand, C. and Beccat, P. 1998. Use of XPS for Reservoir Sandstone Wettability Evaluation. Application to Kaolinite and Illite. *Journal of Petroleum Science and Engineering* **20**(3-4): 259-265.
- Edwards, R.W., Celia, M.A., Bandilla, K.W., Doster, F. and Kanno, C.M. 2015. A Model to Estimate Carbon Dioxide Injectivity and Storage Capacity for Geological Sequestration in Shale Gas Wells. *Environmental Science & Technology* **49**(15): 9222-9229.
- Erbil, H.Y. 2006. *Solid and Liquid Interfaces*. Oxford: Blackwell Publishing.
- Ettensohn, F.R., Miller, M.L., Dillman, S.B., Elam, T.D., Geller, K.L., Swager, D.R., Markowitz, G., Woock, R.D. and Barron, L.S. 1988. Characterization and Implications of the Devonian-Mississippian Black Shale Sequence, Eastern and Central Kentucky, USA: Pycnoclines, Transgression, Regression, and Tectonism.
- Feng, C., Kong, Y., Jiang, G., Yang, J., Pu, C. and Zhang, Y. 2012. Wettability Modification of Rock Cores by Fluorinated Copolymer Emulsion for the Enhancement of Gas and Oil Recovery. *Applied Surface Science* **258**(18): 7075-7081.
- Fowkes, F.M. 1963. Additivity of Intermolecular Forces at Interfaces. I. Determination of the Contribution to Surface and Interfacial Tensions of Dispersion Forces in Various Liquids. *The Journal of Physical Chemistry* **67**(12): 2538-2541.
- Gaus, I. 2010. Role and Impact of CO<sub>2</sub>-Rock Interactions During CO<sub>2</sub> Storage in Sedimentary Rocks. *International Journal of Greenhouse Gas Control* **4**(1): 73-89.
- Gips, J.P. 2014. *Shale Characterization Using TGA, Py-GC-MS, and NMR*. PhD thesis, University of Texas, Austin, Texas (December 2014).
- Gips, J.P., Daigle, H. and Sharma, M. 2014. Characterization of Free and Bound Fluids in Hydrocarbon Bearing Shales Using NMR and Py GC-MS. *Proc.*, Unconventional Resources Technology Conference, Denver, Colorado, 25-27 August, 1217-1225.

- Good, R.J. and Girifalco, L.A. 1960. A Theory for Estimation of Surface and Interfacial Energies. III. Estimation of Surface Energies of Solids from Contact Angle Data. *The Journal of Physical Chemistry* **64**(5): 561-565.
- Hefer, A.W., Bhasin, A. and Little, D.N. 2006. Bitumen Surface Energy Characterization Using a Contact Angle Approach. *Journal of Materials in Civil Engineering* **18**(6): 759-767.
- Hellevang, H., Pham, V.T. and Aagaard, P. 2013. Kinetic Modelling of CO<sub>2</sub>–Water–Rock Interactions. *International Journal of Greenhouse Gas Control* **15**: 3-15.
- Hirasaki, G.J. 1991. Wettability: Fundamentals and Surface Forces. *SPE Formation Evaluation* **6**(2): 217-226.
- Hopkinson, L., Rutt, K. and Cressey, G. 2008. The Transformation of Nesquehonite to Hydromagnesite in the System CaO-MgO-H<sub>2</sub>O-CO<sub>2</sub>: An Experimental Spectroscopic Study. *The Journal of Geology* **116**(4): 387-400.
- Huang, E.T.S. and Holm, L.W. 1988. Effect of WAG Injection and Rock Wettability on Oil Recovery During CO<sub>2</sub> Flooding. *SPE Reservoir Engineering* **3**(1): 119-129.
- Ip, S.W. and Toguri, J.M. 1994. The Equivalency of Surface Tension, Surface Energy and Surface Free Energy. *Journal of Materials Science* **29**(3): 688-692.
- Janczuk, B. and Zdziennicka, A. 1994. A Study on the Components of Surface Free Energy of Quartz from Contact Angle Measurements. *Journal of Materials Science*, **29**(13): 3559-3564.
- Joewondo, N. 2018. *Pore Structure of Micro-and Mesoporous Mudrocks Based on Nitrogen and Carbon Dioxide Sorption*. MS Thesis, Colorado School of Mines, Golden, Colorado (May 2018).
- Johnson, K.L., Kendall, K. and Roberts, A.D. 1971. Surface Energy and the Contact of Elastic Solids. *Proc., Royal Society of London. A. Mathematical and Physical Sciences* **324**(1558): 301-313.
- Johnson, N.C., Thomas, B., Maher, K., Rosenbauer, R.J., Bird, D. and Brown Jr, G.E. 2014. Olivine Dissolution and Carbonation Under Conditions Relevant for in Situ Carbon Storage. *Chemical Geology* **373**: 93-105.
- Koevoets, M.J., Abay, T.B., Hammer, Ø. and Olaussen, S. 2016. High-resolution Organic Carbon–Isotope Stratigraphy of The Middle Jurassic–Lower Cretaceous Agardhfjellet Formation of Central Spitsbergen, Svalbard. *Palaeogeography, Palaeoclimatology, Palaeoecology* **449**: 266-274.
- Kovscek, A.R., Wong, H. and Radke, C.J. 1993. A Pore-level Scenario for the Development of Mixed Wettability in Oil Reservoirs. *AIChE Journal* **39**(6): 1072-1085.

- Kuila, U. 2013. *Measurement and Interpretation of Porosity and Pore-Size Distribution in Mudrocks: The Hole Story of Shales*. PhD Thesis, Colorado School of Mines, Golden, Colorado (May 2018).
- Kuila, U. and Prasad, M. 2013. Specific Surface Area and Pore-size Distribution in Clays and Shales. *Geophysical Prospecting* **61**(2): 341-362.
- Kumar, S. 2016. *Rock-fluid Interaction and Phase Properties of Fluids in Nano-and Subnano-Pores of Shales: Sorption-based Studies*. PhD Thesis, Colorado School of Mines, Golden, Colorado (May 2018).
- Kwok, D.Y. and Neumann, A.W. 1999. Contact Angle Measurement and Contact Angle Interpretation. *Advances in Colloid and Interface Science* **81**(3): 167-249.
- Laidler, K.J. 1984. The Development of The Arrhenius Equation. *Journal of Chemical Education* **61**(6): 494.
- Landers, J., Gor, G.Y. and Neimark, A.V. 2013. Density Functional Theory Methods for Characterization of Porous Materials. *Colloids and Surfaces A: Physicochemical and Engineering Aspects* **437**: 3-32.
- Lingling, Q., Tang, X., Wang, Z. and Peng, X. 2017. Pore Characterization of Different Types of Coal from Coal and Gas Outburst Disaster Sites Using Low Temperature Nitrogen Adsorption Approach. *International Journal of Mining Science and Technology* **27**(2): 371-377.
- Loucks, R.G., Reed, R.M., Ruppel, S.C. and Jarvie, D.M. 2009. Morphology, Genesis, and Distribution of Nanometer-scale Pores in Siliceous Mudstones of the Mississippian Barnett Shale. *Journal of sedimentary research* **79**(12): 848-861.
- Lowell, S., Shields, J.E., Thomas, M.A. and Thommes, M. 2012. *Characterization of Porous Solids and Powders: Surface Area, Pore Size and Density*. New York City: Springer Science & Business Media.
- Mercier, F., Toulhoat, N., Potocek, V. and Trocellier, P. 1999. The Role of Nitrogen and Sulphur Bearing Compounds in the Wettability of Oil Reservoir Rocks: An Approach with Nuclear Microanalysis and Other Related Surface Techniques. *Nuclear Instruments and Methods in Physics Research Section B: Beam Interactions with Materials and Atoms* **152**(1): 122-128.
- Metz, B., Davidson, O., de Coninck, H., Loos, M., and Meyer, L. 2005. *Carbon Dioxide Capture and Storage*. Edinburgh: Cambridge University Press.
- Mitchell, A.G., Hazell, L.B. and Webb, K.J. 1990. Wettability Determination: Pore Surface Analysis. Presented at the SPE Annual Technical Conference and Exhibition, New Orleans, Louisiana, 23-26 September. SPE-20505-MS. <https://doi.org/10.2118/20505-MS>

- Mittal, K. and Etzler, F. 2008. Is the World Basic? Lessons from Surface Science. *Annales UMCS, Chemistry* **63**: 1-16.
- Morimoto, T., Kishi, J., Okada, O. and Kadota, T. 1980. Interaction of Water with the Surface of Calcite. *Bulletin of the Chemical Society of Japan* **53**(7): 1918-1921.
- Morra, M. 1996. Some Reflection on the Evaluation of the Lewis Acid–Base Properties of Polymer Surfaces by Wetting Measurements. *Journal of Colloid and Interface Science* **182**(1): 312-314
- Mullins, O.C. 2011. The Asphaltenes. *Annual Review of Analytical Chemistry* **4**: 393-418.
- Murugesu, M.P. 2017. Pore Structure Analysis Using Subcritical Gas Adsorption Method. Presented at the SPE Annual Technical Conference and Exhibition, San Antonio, Texas, 9-11 October. SPE-189292-STU. <https://doi.org/10.2118/189292-STU>.
- Nuttall, B.C., Eble, C., Bustin, R.M. and Drahovzal, J.A. 2005. Analysis of Devonian Black Shales in Kentucky for Potential Carbon Dioxide Sequestration and Enhanced Natural Gas Production. *Greenhouse Gas Control Technologies* **7**: 2225-2228.
- Óvári, L., Calderon, S.K., Lykhach, Y., Libuda, J., Erdöhelyi, A., Papp, C., Kiss, J. and Steinrück, H.P. 2013. Near Ambient Pressure XPS Investigation of the Interaction of Ethanol with Co/CeO<sub>2</sub> (1 1 1). *Journal of catalysis* **307**: 132-139.
- Owens, D.K. and Wendt, R.C. 1969. Estimation of the Surface Free Energy of Polymers. *Journal of applied polymer science* **13**(8): 1741-1747.
- Panfiloff, A. 2016. *Experimental Evaluation of Dynamic Elastic Properties and Anisotropy in Shales*. PhD Thesis, Colorado School of Mines, Golden, Colorado (May 2018).
- Pomerantz, D. 2014. Modern Spectroscopies for Characterizing the Chemical Composition of Kerogen and Bitumen. AAPG Geoscience Technology Workshop, Pittsburgh, Pennsylvania, 17-19 June
- Quet, C., Glotin, G., Cheneviere, P. and Bourrel, M. 1991. Core Surface Analysis for Wettability Assessment. *Adv. in Core Evaluation II*: 119-131.
- Ratner, B.D. and Castner, D.G. 1994. Advances in X-ray Photoelectron Spectroscopy Instrumentation and Methodology: Instrument Evaluation and New Techniques with Special Reference to Biomedical Studies. *Colloids and Surfaces B: Biointerfaces* **2**(1-3): 333-346.
- Remy, M.J. and Poncelet, G. 1995. A New Approach to the Determination of the External Surface and Micropore Volume of Zeolites from the Nitrogen Adsorption Isotherm at 77 K. *The Journal of Physical Chemistry* **99**(2): 773-779.

- Rouquerol, J., Rouquerol, F., Llewellyn, P., Maurin, G. and Sing, K.S. 2013. *Adsorption by Powders and Porous Solids: Principles, Methodology and Applications*, second edition. Amsterdam, Netherlands: Academic press.
- Rulison, C. 1999. So You Want to Measure Surface Energy? KRÜSS Technical Note TN306e, Augustine Note #401, North Carolina (June 1999).
- Shuttleworth, R. 1950. The Surface Tension of Solids. *Proc., Physical Society. Sec. A* **63**(5): 444.
- Sing, K.S.W., Everett, D.H., Haul, R.A.W., Moscou, L., Pierotti, R.A., Rouquerol, J., and Siemieniewska, T. 1985. IUPAC Recommendations 1984: Reporting Physisorption Data for Gas/Solid Systems with Special Reference to the Determination of Surface Area and Porosity. *Pure and Applied Chemistry* **57**(4): 603-619.
- Sipilä, J., Teir, S. and Zevenhoven, R. 2008. Carbon Dioxide Sequestration by Mineral Carbonation: Literature Review Update 2005–2007. *Report Vt 1*: 2008.
- Stoerzinger, K.A., Hong, W.T., Crumlin, E.J., Bluhm, H. and Shao-Horn, Y. 2015. Insights into Electrochemical Reactions from Ambient Pressure Photoelectron Spectroscopy. *Accounts of Chemical Research* **48**(11): 2976-2983.
- Storck, S., Bretinger, H. and Maier, W.F. 1998. Characterization of Micro-and Mesoporous Solids by Physisorption Methods and Pore-Size Analysis. *Applied Catalysis A: General* **174**(1-2): 137-146.
- Teklu, T.W., Alameri, W., Kazemi, H. and Graves, R.M. 2015. Contact Angle Measurements on Conventional and Unconventional Reservoir Cores. Presented at the Unconventional Resources Technology Conference, San Antonio, Texas, 20-22 July. <https://doi.org/10.15530/urtec-2015-2153996>.
- Thommes, M. 2010. Physical Adsorption Characterization of Nanoporous Materials. *Chemie Ingenieur Technik* **82**(7): 1059-1073.
- Thommes, M. and Cychosz, K. A. 2014. Physical Adsorption Characterization of Nanoporous Materials: Progress and Challenges. *Adsorption* **20**: 233–250.
- Thommes, M., Kaneko, K., Neimark, A.V., Olivier, J.P., Rodriguez-Reinoso, F., Rouquerol, J. and Sing, K.S. 2015. Physisorption of Gases, with Special Reference to the Evaluation of Surface Area and Pore Size Distribution (IUPAC Technical Report). *Pure and Applied Chemistry* **87**(9-10): 1051-1069.
- Toledo, P.G., Araujo, Y.C. and Leon, V. 1996. Wettability of Oil-producing Reservoir Rocks as Determined from X-Ray Photoelectron Spectroscopy. *Journal of Colloid and Interface Science* **183**(2): 301-308.
- van der Meer, L.G.H., Kreft, E., Geel, C. and Hartman, J. 2005. K12-B a Test Site for CO<sub>2</sub> Storage and Enhanced Gas Recovery. *Proc., 67th EAGE Conference & Exhibition, Madrid, Spain, 13-16 June. SPE-94128-MS*.

- van Oss, C.J. 1993. Acid-base Interfacial Interactions in Aqueous Media. *Colloids and Surfaces A: Physicochemical and Engineering Aspects* **78**: 1-49.
- van Oss, C.J., Chaudhury, M.K. and Good, R.J. 1988. Interfacial Lifshitz-van der Waals and Polar Interactions in Macroscopic Systems. *Chemical Reviews* **88**: 927 – 941.
- Voogd, P., Scholten, J.J.F. and Van Bekkum, H. 1991. Use of the T-Plot—De Boer Method in Pore Volume Determinations of ZSM-5 Type Zeolites. *Colloids and surfaces* **55**: 163-171.
- Wei, M., Zhang, L., Xiong, Y., Li, J., and Peng, P. 2016. Nanopore Structure Characterization for Organic-Rich Shale using the Non-Local-Density Functional Theory by a Combination of N<sub>2</sub> and CO<sub>2</sub> Adsorption. *Microporous and Mesoporous Materials* **227**: 88–94.
- Young, Thomas. 1805. III. An Essay on the Cohesion of Fluids. *Philosophical Transactions of the Royal Society of London* **95**: 65-87.
- Zargari, S., Karen L.C., and Manika P. 2015. Porosity Evolution in Oil-prone Source Rocks. *Fuel* **153**: 110-117.
- Zelenev, A.S. 2011. Surface Energy of North American Shales and Its Role in Interaction of Shale with Surfactants and Microemulsions. Presented at the SPE International Symposium on Oilfield Chemistry, Woodlands, Texas, 11-13 April. SPE-141459-MS. <https://doi.org/10.2118/141459-MS>
- Zelenev, A.S. and Grenoble, Z. 2018. Wettability of Reservoir Rocks Having Different Polarity by a Model Nonionic Surfactant: Fluid Imbibition Study into Crushed Rock Packs. *Energy & Fuels* **32**(2): 1340-1347.
- Zelenev, A.S. and Lett, N. 2013. Surface Free Energy and Wettability of Different Oil and Gas Reservoir Rocks. *Advances in Contact Angle, Wettability and Adhesion* **1**: 377-388.
- Zerpa, L.E., Salager, J.L., Koh, C.A., Sloan, E.D. and Sum, A.K. 2010. Surface Chemistry and Gas Hydrates in Flow Assurance. *Industrial & Engineering Chemistry Research* **50**(1): 188-197.
- Zhang, T., Ellis, G.S., Ruppel, S.C., Milliken, K. and Yang, R. 2012. Effect of Organic-Matter Type and Thermal Maturity on Methane Adsorption in Shale-Gas Systems. *Organic geochemistry* **47**: 120-131.
- Zisman, W. A. 1964. Contact Angle, Wettability, and Adhesion. *Advances in Chemistry Series* **43**:1.

## APPENDIX A

### SUPPLEMENTAL ELECTRONIC FILES

Apart from the content of this work, I have also second-authored a paper published in the *Journal of Volcanology and Geothermal Research*. This paper analyzes specific surface area as a measure of alteration of volcanic rocks. By measuring complex conductivities of a set of 28 basalts from Hawaii, the paper concludes that surface and quadrature conductivities are directly related to specific surface area. The published title of this work is *Alteration of Volcanic Rocks: A New Non-Intrusive Indicator Based on Induced Polarization Measurements*. I am the second author of this work with Andre Revil, Manika Prasad and Mathieu Le-Breton. This peer-reviewed and published manuscript is attached as a supplementary file.

Table A.1: Supplementary files of the manuscript that have been published apart from the work contained in this thesis

Revil_Murugesu_Volcanology_Geothermal Research	PDF file containing manuscript peer-reviewed and published in the <i>Journal of Volcanology and Geothermal Research</i> analyzing the relation between complex conductivity and specific surface area (SSA).
--	--